

ASSESSMENT OF TAYLOR-SERIES MODEL FOR ESTIMATION OF VORTEX
FLOWS USING SURFACE STRESS MEASUREMENTS

By

Gaurang Shrikhande

A THESIS

Submitted to
Michigan State University
in partial fulfillment of the requirements
for the degree of

MASTER OF SCIENCE

Mechanical Engineering

2012

ABSTRACT

ASSESSMENT OF TAYLOR-SERIES MODEL FOR ESTIMATION OF VORTEX FLOWS USING SURFACE STRESS MEASUREMENTS

By

Gaurang Shrikhande

This research is motivated by the development of ground-based sensor arrays for detection of wake vortices behind an aircraft that would enable take off and landing at faster rates at commercial airports in the United States. It is envisioned that multiple sensor-array units installed along the sides of runways would accurately detect the strength and the location of wake vortices in real time, enabling efficient and safe management of airplane take-offs and landings. The focus of this research is on examining the feasibility of a method that can estimate the details of the velocity field of wake vortices from distributed measurements of the wall shear stress and pressure. The method relies on obtaining a Taylor-series expansion of the velocity field starting from the ground. This idea is based on the ability to derive the coefficients of the Taylor-series expansion up to an arbitrary order using only wall-shear-stress and -pressure information coupled with recursive relations that are derived from the Navier-Stokes equations without any knowledge of the far-field boundary condition. In the current research, we examined the possibility that this concept can be extended to estimate the wake-vortex velocity field from near-wall-velocity and -pressure information. The analysis shows that though the Taylor-series model works in principle, the convergence of the series is very slow, enabling accurate estimation of only the flow within the boundary layer. Furthermore, the increase in size of the accurately estimated domain above the wall with increase in the series order reaches a 'break even' point at which further increase in the order is offset by inaccuracies in calculating high-order derivatives.

Copyright by
GAURANG SHRIKHANDE
2012

To
My Family

ACKNOWLEDGMENTS

I would like to express my sincere gratitude to Dr. Naguib for giving me the opportunity to work at Flow Physics and Control Laboratory (FPaCL), for his patience and continuous guidance during my graduate studies, and for helping me in some of my difficult times both academically and personally. I am thankful to Dr. Dominique Fourquette for her guidance and expertise. I am thankful to Michigan Aerospace Corporation for generously supporting the initial phase of the project under contract # F1373-02012010. I would like to express my special thanks to Dr. M. M. Koochesfahani for giving us access to the experimental data, providing a discussion forum through group meetings and giving feedback on research, as and when required.

I owe my deepest gratitude to my grand-parents late Shalini, late Digambar, late Arvind, Indira, and Madhuri, my parents Swati and Sanjay, my sister Gayatri, and aunt Kalpana for their unconditional love, support, encouragement, and for being my strength.

Special thanks to Rohit Nehe, Kyle Bade, and Malek Al-Aweni for making my time at ERC eventful. I would like to thank my closest friends from elementary school and beyond - Sonali, Suchita, Abdul Husein, Bhaargav, and Ankur. Sincere thanks to my friend Krupesh for his support and encouragement at all times. Lastly, thanks to International Students Association (ISA) and Office for International Students and Scholars (OISS) for truly *internationalizing* my life.

TABLE OF CONTENTS

List of Tables		ix
List of Figures		x
1 Introduction		1
1.1 Motivation		1
1.2 Approach		4
1.2.1 Step I - Construction and Validation of the Taylor-series model.		4
1.2.2 Step II - Numerical Computation to evaluate the applicability of the Taylor-series model to estimate the flow field of a vortex-pair above a wall.		5
1.2.3 Step III - Study of Cartesian Taylor Series model using simulations.		6
2 Taylor-series Model For Estimation of Incompressible Flow Fields Using Wall-Stress Information		7
2.1 Background		7
2.2 Concept in 2D		8
2.2.1 Step I. Expanding the stream function (ψ) in a two-dimensional, infinite Taylor-series form		8
2.2.2 Step II. Expressing the velocity components in series form by differentiating the series for the stream function given by Equation 2.1		9
2.2.3 Step III. Obtaining series expressions for partial derivatives of the velocity components in the momentum equation (the components of which in the x and y directions are given by Equations 2.20 and 2.24 respectively)		10
2.2.4 Step IV. Obtaining expression relating the lowest-order Taylor series coefficients a_{1j} to the wall shear stress using the constitutive equation for Newtonian fluids		11
2.2.5 Step V. Obtaining expression relating the next-order Taylor series coefficients a_{2j} to the wall pressure gradient using the momentum equation in the streamwise direction		12
2.2.6 Step VI. Obtaining expressions for higher-order Taylor series coefficients in terms of a_{1j} and a_{2j} and their time derivatives by successive differentiation (in the wall-normal direction) of the 2D momentum equations and evaluating the result at the wall		14
2.3 Demonstration In Laminar Flows With Known Analytical Solution		17
2.3.1 Blasius Boundary Layer		19

2.3.2	Falkner-Skan Boundary Layer ($m = 1$)	22
2.3.3	Stokes Oscillating Stream Problem	26
2.4	Summary	29
3	Validation of The Computational Approach	32
3.1	Background	33
3.2	Description of The Experimental Data	34
3.2.1	Credits	34
3.2.2	Introduction	34
3.2.3	Experimental Facility	35
3.2.4	Observations	35
3.3	Initial Conditions For The Simulation Model	39
3.3.1	Gaussian Vorticity Distribution	39
3.3.1.1	<i>Two</i> -Parameter Fit	43
3.3.1.2	<i>Three</i> -Parameter Fit	43
3.3.2	Comparison of Numerical Results With Experiments	44
3.3.2.1	Effect of computational time step	54
3.3.2.2	Effect of number of iterations per time step	58
3.3.2.3	Effect of grid size	58
3.4	Summary of Fluent Parameters	60
3.4.0.4	General Attributes:	60
3.4.0.5	Solution Methods:	62
3.4.0.6	Solution Controls:	62
4	Simulation of A Pair of Line Vortices Impinging On A Solid Wall And Estimation of Velocities Using The Cartesian Taylor Series Model	63
4.1	Geometry of the Computational Model	64
4.2	Simulations Using ANSYS [®] -Fluent	65
4.3	Simulation Results	68
4.4	Estimations Using Cartesian Taylor-series Model	76
4.5	Results and Discussion	77
4.5.1	Comparison of estimations based on different grid resolutions	77
4.5.2	The same grid resolution (600×600) but two different estimation locations: $x = 25$ mm and $x = 30$ mm	83
5	Summary, Conslusions and Recommendations	86
5.1	Summary and Conclusions	86
5.2	Recommendations	88
	APPENDICES	90

A Taylor-series Model for Axisymmetric Flow	91
A.1 Derivation of the Taylor-series Model for Axisymmetric Flow	91
A.1.1 Step I. Expanding the stream function (ψ) in a two-dimensional, infinite Taylor-series form	91
A.1.2 Step II. Expressing the velocity components in a series form by differentiating the series for the stream function given by Equation A.1	92
A.1.3 Step III. Obtaining series expressions for partial derivatives of the velocity components in the momentum equations A.20	93
A.1.4 Step IV. Obtaining expression relating the lowest-order Taylor series coefficients a_{0j} to the wall shear stress using constitutive equation for Newtonian fluids	94
A.1.5 Step V. Obtaining expression relating the next-order Taylor series coefficients a_{1j} to the wall pressure gradient using the momentum equation in the streamwise direction	95
A.1.6 Step VI. Obtaining expressions for higher-order Taylor series coefficients in terms of a_{0j} and a_{1j} and their time derivatives by successive differentiation (in the wall-normal direction) of the 2D momentum equations and evaluating the result at the wall	97
A.2 Demonstration In Axisymmetric Laminar Flows With Known Analytical Solution	99
A.2.1 Axisymmetric Flow	100
 BIBLIOGRAPHY	 105

LIST OF TABLES

Table 2.1	Analytical flows employed in validation of MATLAB [®] code used to derive Taylor series coefficients	18
Table 3.1	Initial Vortex parameters obtained from the Gaussian fit	44
Table 3.2	Computational cases and associated initial vortex parameters. Listed experimental values are those given by Gendrich <i>et al.</i> [3]	54
Table 4.1	Comparison of the y extent from the wall over which the u -velocity estimation has an error less than $\pm 0.1\%$ at a location directly beneath the center of the primary vortex ($x = 25$ mm) for different grid sizes	82
Table 4.2	Comparison of the y extent from the wall over which the v -velocity estimation has an error less than $\pm 0.1\%$ at a location directly beneath the center of the primary vortex ($x = 25$ mm) for different grid sizes	82
Table 4.3	Comparison of the y extent from the wall over which the u -velocity estimation has an error less than $\pm 0.1\%$ at a location directly beneath the center of the primary vortex ($x = 25$ mm) and $x = 30$ mm . . .	83
Table 4.4	Comparison of the y extent from the wall over which the u -velocity estimation has an error less than $\pm 0.1\%$ at a location directly beneath the center of the primary vortex ($x = 25$ mm) and $x = 30$ mm . . .	85
Table A.1	Analytical flows employed in validation of MATLAB [®] code used to derive Taylor series coefficients	100

LIST OF FIGURES

Figure 1.1	Schematic of wake vortices behind a finite-span airfoil (top) and an aircraft (bottom). (Web source [13])	2
Figure 2.1	Series expansions up to the 45 th order of the streamwise velocity compared to the analytical solution for Blasius boundary layer. (For interpretation of the references to color in this and all other figures, the reader is referred to the electronic version of this thesis.)	23
Figure 2.2	Series expansions up to the 45 th order of the streamwise velocity compared to the analytical solution for Falkner-Skan ($m = 1$) boundary layer	27
Figure 2.3	Series expansions up to the 45th order of the streamwise velocity compared to the analytical solution for Stokes oscillating stream flow. Different plots represent different phases of the oscillation cycle . . .	30
Figure 3.1	Experimental Set up (units are in cm) - Axisymmetric vortex impinging on a wall [3]	36
Figure 3.2	Coordinate axes, $D_0 = 0.0364$ m and the core diameter $2R_C = 1.06$ cm (used in this thesis as $R_C = \mathbf{0.0053}$ m[3])	36
Figure 3.3	Flow visualization using LIF [3]	37
Figure 3.4	Near-wall velocity vectors, time in <i>seconds</i> [3]	38
Figure 3.5	Geometry of the computational model to be used in ANSYS [®] -Fluent based on experimental geometry given in Figure 3.2 [3]	40
Figure 3.6	Experimental vorticity at $t = 1.4$ s along lines passing through the vortex core center while parallel to r and z axis	42
Figure 3.7	Two-parameter fit, with $r_{peak} = 0.018$ m and $z_{peak} = 0.02$ m is taken from from the experiments at $t = 1.4$ s, compared to experimental data for the r -profile	45

Figure 3.8	Two-parameter fit, with $r_{peak} = 0.018$ m and $z_{peak} = 0.02$ m is taken from the experiments at $t = 1.4$ s, compared to experimental data for the z -profile	45
Figure 3.9	Three-parameter fit compared to experimental data for the r -profile. Initial position of the center of vortex r_{peak} and z_{peak} is obtained from the fit	46
Figure 3.10	Three-parameter fit compared to experimental data for the z -profile. Initial position of the center of vortex r_{peak} and z_{peak} is obtained from the fit	46
Figure 3.11	Experimental, r and z vorticity profiles compared with <i>two</i> -parameter and <i>three</i> -parameter Gaussian fits	47
Figure 3.12	Vorticity (ω_θ) contour of the <i>experimental</i> flow-field at $t = 0.3$ s (measured relative to the time of occurrence of the velocity field used to set the initial Gaussian vortex parameters for the computation: $t = 1.4$ s relative to the solenoid opening)	50
Figure 3.13	Vorticity (ω_θ) contour of the <i>simulated</i> flow-field at $t = 0.3$ s	50
Figure 3.14	Vorticity (ω_θ) contour of the <i>experimental</i> flow-field at $t = 0.5$ s (measured relative to the time of occurrence of the velocity field used to set the initial Gaussian vortex parameters for the computation: $t = 1.4$ s relative to the solenoid opening)	51
Figure 3.15	Vorticity (ω_θ) contour of the <i>simulated</i> flow-field at $t = 0.5$ s	51
Figure 3.16	Vorticity (ω_θ) contour of the <i>experimental</i> flow-field at $t = 0.8$ s (measured relative to the time of occurrence of the velocity field used to set the initial Gaussian vortex parameters for the computation: $t = 1.4$ s relative to the solenoid opening)	52
Figure 3.17	Vorticity (ω_θ) contour of the <i>simulated</i> flow-field at $t = 0.8$ s	52
Figure 3.18	Vorticity (ω_θ) contour of the <i>experimental</i> flow-field at $t = 1$ s (measured relative to the time of occurrence of the velocity field used to set the initial Gaussian vortex parameters for the computation: $t = 1.4$ s relative to the solenoid opening)	53
Figure 3.19	Vorticity (ω_θ) contour of the <i>simulated</i> flow-field at $t = 1$ s	53
Figure 3.20	Comparison of the temporal evolution of the vorticity at the center of the primary vortex. Results from simulations based on <i>three</i> -parameter r, z and $avg(r, z)$ Gaussian profiles are compared with those from MTV experiments.	55

Figure 3.21	Axial- (z), and radial- (r) trajectories of the center of the primary vortex.	56
Figure 3.22	Effect of the computational time step on maximum vorticity of the primary-vortex (a) and boundary layer (b) vorticity. ($\Gamma_0 = 46.11 \times 10^{-4} \text{ m}^2/\text{s}$, $R_C = 0.005012 \text{ m}$, 300 iterations/time step, 600×600 grid)	57
Figure 3.23	Effect of no iterations per time step on maximum vorticity of the primary-vortex (a) and boundary layer (b) vorticity. ($\Gamma_0 = 46.11 \times 10^{-4} \text{ m}^2/\text{s}$, $R_C = 0.005012 \text{ m}$, Time step = 0.005s, 600×600 grid)	59
Figure 3.24	Effect of different grid resolution on maximum vorticity of the primary-vortex (a) and boundary layer (b) vorticity. ($\Gamma_0 = 46.11 \times 10^{-4} \text{ m}^2/\text{s}$, $R_C = 0.005012 \text{ m}$, 300 iterations/time step, Time step = 0.005 s)	61
Figure 4.1	Illustration of the numerical domain and initial/boundary conditions used for simulation of a pair of counter rotating vortices having initial circulation $\Gamma_0 = 46.11 \times 10^{-4} \text{ m}^2/\text{s}$ and initial core radius $R_C = 0.005012 \text{ m}$ introduced in a $0.06 \times 0.06 \text{ m}^2$ square-domain at $(0.018337, 0.019602) \text{ m}$ at $t = 0$. Because of problem symmetry, only the upper half domain containing one of the vortices is computed.	65
Figure 4.2	Comparison of the Vorticity at the core center of the primary vortex for an axisymmetric vortex ring (ω_θ) and 2D vortex (ω_z)	67
Figure 4.3	Vorticity (ω_z in s^{-1}) contour of Cartesian flow at $\mathbf{t} = \mathbf{0.005 s}$ showing evolution of the primary vortex.	69
Figure 4.4	Vorticity (ω_z in s^{-1}) contour of Cartesian flow at $\mathbf{t} = \mathbf{0.25 s}$ showing evolution of the primary vortex.	69
Figure 4.5	Vorticity (ω_z in s^{-1}) contour of Cartesian flow at $\mathbf{t} = \mathbf{0.50 s}$ showing evolution of the primary vortex.	70
Figure 4.6	Vorticity (ω_z in s^{-1}) contour of Cartesian flow showing at $\mathbf{t} = \mathbf{0.605 s}$ evolution of the primary vortex.	70
Figure 4.7	Vorticity (ω_z in s^{-1}) contour of Cartesian flow at $\mathbf{t} = \mathbf{0.75 s}$ showing evolution of the primary vortex.	71
Figure 4.8	Vorticity (ω_z in s^{-1}) contour of Cartesian flow at $\mathbf{t} = \mathbf{1 s}$ showing evolution of the primary vortex.	71

Figure 4.9	τ_{wall} profile at time $t = 0.605$ s	72
Figure 4.10	p_{wall} profile at time $t = 0.605$ s	72
Figure 4.11	$\frac{\partial p_{wall}}{\partial x}$ profile at time $t = 0.605$ s	73
Figure 4.12	Streamwise (u -) and wall-normal (v -) profile in a plane at $x = 30$ mm (near outer edge of the primary vortex) at time $t = 0.605$ s as determined by Fluent simulations for the case of <i>Domain-600</i>	73
Figure 4.13	Streamwise (u -) and wall-normal (v -) profile in a plane at $x = 25$ mm (nearest pixel to the maximum vorticity, at the center of the primary vortex) at time $t = 0.605$ s as determined by Fluent simulations for the case of <i>Domain-600</i>	74
Figure 4.14	Comparison of the wall-shear stress profile along the wall, at $t = 0.605$ s for <i>Domain-500</i> , <i>-600</i> , <i>-715</i>	75
Figure 4.15	Comparison of the wall-pressure gradient along the wall, at $t = 0.605$ s for <i>Domain-500</i> , <i>-600</i> , <i>-715</i>	75
Figure 4.16	u -Velocity estimation using Taylor-series expansions up to 15 th order for the case of <i>Domain-500</i> in a plane through the center of the primary vortex ($x = 25$ mm)	78
Figure 4.17	v -Velocity estimation using Taylor-series expansions up to 15 th order for the case of <i>Domain-500</i> in a plane through the center of the primary vortex ($x = 25$ mm)	78
Figure 4.18	u -Velocity estimation using Taylor-series expansions up to 15 th order for the case of <i>Domain-600</i> in a plane through the center of the primary vortex ($x = 25$ mm)	79
Figure 4.19	v -Velocity estimation using Taylor-series expansions up to 15 th order for the case of <i>Domain-600</i> in a plane through the center of the primary vortex ($x = 25$ mm)	79
Figure 4.20	u -Velocity estimation using Taylor-series expansions up to 15 th order for the case of <i>Domain-715</i> in a plane through the center of the primary vortex ($x = 25$ mm)	80
Figure 4.21	v -Velocity estimation using Taylor-series expansions up to 15 th order for the case of <i>Domain-715</i> in a plane through the center of the primary vortex ($x = 25$ mm)	80

Figure 4.22	<i>u</i> -Velocity estimation using Taylor-series expansions up to 15 th order for the case of <i>Domain-600</i> in a plane through outer edge (away from the axis) of the Primary vortex ($x = 30$ mm)	84
Figure 4.23	<i>v</i> -Velocity estimation using Taylor-series expansions up to 15 th order for the case of <i>Domain-600</i> in a plane through outer edge (away from the axis) of the Primary vortex ($x = 30$ mm)	84
Figure A.1	Series expansions up to the 40 th order of the radial velocity compared to the analytical solution for axisymmetric stagnation flow	103
Figure A.2	Series expansions up to the 40 th order of the wall-normal velocity compared to the analytical solution for axisymmetric stagnation flow	103

Chapter 1

Introduction

1.1 Motivation

This research is motivated by the development of ground-based sensor arrays for detection of wake vortices behind an aircraft that would enable take off and landings at faster rates at commercial airports in the United States. This research, undertaken at the Flow Physics and Control Laboratory (FPaCL) at Michigan State University, coupled with resources and expertise from Michigan Aerospace Corporation (MAC), the sponsor of the current work, is intended to lead to designing such a sensor system to be developed commercially (by MAC) and installed at commercial airports in the country.

Current Federal Aviation Administration (FAA) regulations limit the rate at which aircraft landings and take-offs happen due to mandatory spacing requirements between two successive commercial aircrafts. It is required for a medium-sized aircraft to maintain 4 - 6 NM (Nautical Mile) distance behind a heavy aircraft during landings and 2 - 3 NM during take-offs [1]. This limit is imposed to avoid accidents due to wake vortices forming in the

wake of the leading aircraft interfering with the trailing aircraft during landing or take-off (see Figure 1.1 [13]). Wake vortices are the vortical structures that are formed at the wing-tip of an aircraft (or any lift producing system). These vortices could be quite strong and they persist over a long time period depending upon the type of aircraft. Heavy aircrafts generate stronger vortices that last longer compared to light-weight ones. These wake vortices interact with a trailing airplane and may cause it to roll and crash due to the associated swirling flow or cause loss of altitude due to downwash (see Figure 1.1).

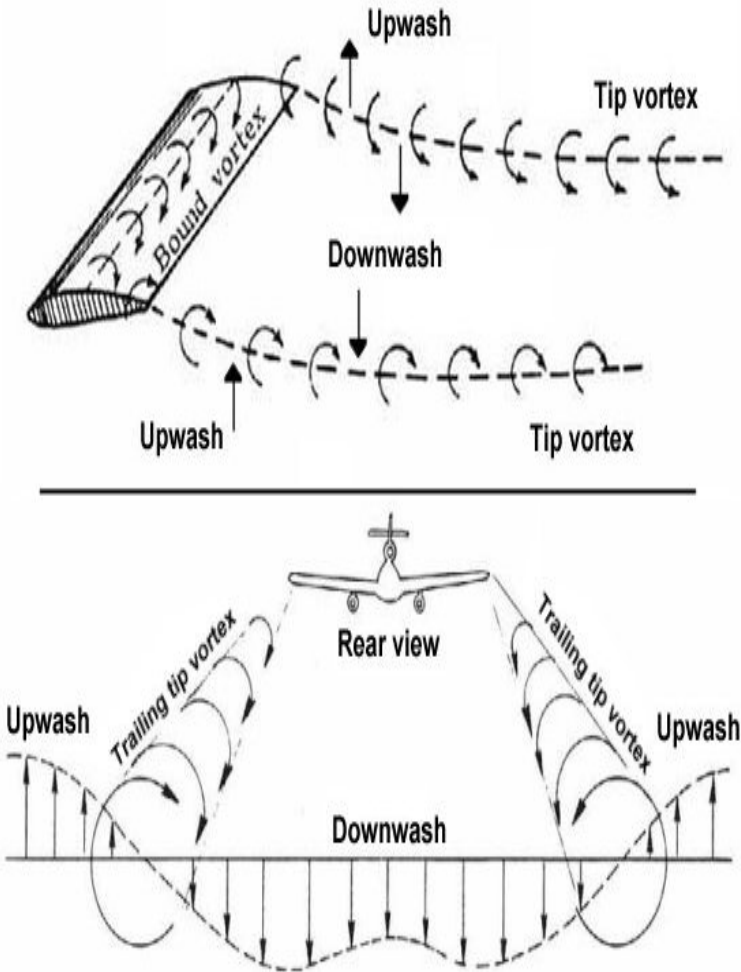


Figure 1.1: Schematic of wake vortices behind a finite-span airfoil (top) and an aircraft (bottom). (Web source [13])

The ground-based sensor system will allow landings and take-offs at faster rate (15% [1]) through accurate detection of the vortex strength and the location of the wake vortices. It is envisioned that multiple sensor-array units will be installed along the sides of runways to capture near-ground-velocity (i.e. wall shear stress) and -pressure information near the runway. The assessment of a method for utilization of this information to estimate the above-ground flow field of wake vortices is the subject of the current study. Unlike other surface-based flow estimation methods, such as used for feedback flow control, the uniqueness of the current approach is that it does not require empirical information and/or approximate models.

Current wake-vortex measurement systems at airports include wind anemometers, pulse and continuous-wave Light Detection and Ranging (LIDAR) and Radar Acoustic Sounding Sensor (RASS). These technologies capture integrated data related to overall vortex circulation and *not* the detailed flow-field of the vortex structure.

The method examined here relies on obtaining a Taylor-series expansion of the velocity field starting from the wall. The basic idea of this technique was published by Dallman *et al.* [2] who demonstrated the ability to derive the coefficients of the Taylor-series expansion up to an arbitrary order using only wall-shear-stress and -pressure information coupled with recursive relations that are derived from the Navier-Stokes equations without any knowledge of the far-field boundary condition. In the current research, we examine the possibility that this concept can be extended to estimate the wake-vortex velocity field where the far-field boundary is not known but knowledge of wall stresses can be obtained from the near-wall-velocity and -pressure signatures captured by sensors installed near the runways. If successful, the estimated velocity field would be analyzed to locate the cores of wake

vortices and find their strengths in real time.

The specific objectives of this research are to demonstrate the usability of the Taylor-series model for velocity estimation, understand the strengths and limitations of the method, study parameters influencing its performance, and test its applicability for the wake vortex problem.

1.2 Approach

In order to address the objectives outlined above, we followed a three-step approach-

1.2.1 Step I - Construction and Validation of the Taylor-series model.

The expressions for the Taylor-series coefficients were initially hand-derived to understand the underlying mathematical process and to identify recursive patterns that may be used to construct a computer program to derive the coefficients. Using the identified patterns, a MATLAB[®] program is developed to automate the process of deriving the expressions in terms of the wall-shear and -pressure information for series coefficients up to any arbitrary order. Additionally, a separate MATLAB[®] code is developed that is used in conjunction with the program that generates the series-coefficients expressions *to compute* the values of the coefficients based on the time history of the wall-shear stress and the wall-pressure fields. This program, after computing the coefficients, is used to expand the series for the streamwise u - and the wall-normal v -velocities up to a specified order.

The constructed programs required validation to ensure that the expressions for the coefficients are computed accurately. We identified three fundamental flows with known

analytical solutions to compare against that estimated using the Taylor-series model for validation purpose -

1. Blasius Boundary Layer
2. Falkner Skan ($m = 1$; *i.e.* two-dimensional stagnation-point flow)
3. Stokes Oscillating Stream Problem

1.2.2 Step II - Numerical Computation to evaluate the applicability of the Taylor-series model to estimate the flow field of a vortex-pair above a wall.

As discussed earlier, the motivation behind this study was to analyze the Taylor-series model to see if it can be applied to estimate vortex flows. Given the infancy state of the estimation model, it is sensible to test the method first under simple, controlled, yet relevant, flow conditions. The selected flow problem is that of a counter-rotating vortex pair above a wall. This problem can be viewed as analogous to the wake-vortex problem where the counter-rotating vortices are generated at the tip of an aircraft wing which is symmetric about the aircraft axis (parallel to the centerline of the runway). The vortices then convect down towards the ground under the effect of their mutually-induced velocity.

The database of the vortex-pair-above-a-wall flow field was obtained from numerical simulation using ANSYS[®]-Fluent CFD solver. In order to validate the accuracy of the computational approach/parameters, it is necessary to compare against experiments. Though no such data were accessible for the specific problem of interest, measurements in the closely-related problem of an axisymmetric ring above a wall by Gendrich *et al.* [3] could be found. Thus, prior to computation of the two-dimensional vortex-pair simulation, a calculation of

the axisymmetric problem was undertaken. Upon validation, the same computational parameters (e.g. initial and boundary conditions, time step size, grid resolution, etc.) were then used to generate the numerical data for the counter-rotating linear vortex pair above a wall to study the Cartesian Taylor-series model.

1.2.3 Step III - Study of Cartesian Taylor Series model using simulations.

The numerical data for the Cartesian simulations yield the velocity-vector and the pressure field. This can be used to compute the wall-stresses (and their time derivatives) by using the central difference scheme. The computed stresses are then used to obtain the Taylor series estimation of the velocity field and the result is compared against the actual flow field to assess the accuracy and speed of convergence of the series. It is obvious that the accuracy of the Taylor-series model will depend on how accurately the derivatives used to obtain the series coefficients are computed. Finer grid should give better accuracy of the derivatives. Hence, three spatial resolutions were used to study their effect on the estimation.

Chapter 2

Taylor-series Model For Estimation of Incompressible Flow Fields Using Wall-Stress Information

It is demonstrated in this chapter that the velocity field for an incompressible flow can be estimated using a Taylor-series-based mathematical model *with coefficients that can be determined solely* from knowledge of the time history of the wall-shear stress and wall-pressure gradient.

2.1 Background

Wu *et al.* [4] developed a generalized theory for the interaction between a three-dimensional moving body with compressible viscous flows. Their analysis showed that for incompressible flows, it is possible to estimate the entire flow field with knowledge of initial conditions as well as, the vorticity and its flux at the wall without having any knowledge of the far-field boundary conditions. The authors were able to reduce the Navier-Stokes equations

into a form that could be expressed in terms of generalized recursive relation between the wall-vorticity and the wall-vorticity flux. These expressions can be used for computing wall-normal derivatives of the velocity and pressure field at the wall *up to* any arbitrary order. Meaning, the entire flow field can be obtained from an expansion in terms of a continuous (and infinite) series whose coefficients are essentially functions of the wall vorticity and wall-vorticity flux, assuming that the series does converge. Dallman *et al.* [2] elaborated on the same concept for two-dimensional incompressible flows by analyzing the fourth-order stream-function (ψ) form of Navier-Stokes equations.

2.2 Concept in 2D

It is known that the two-dimensional (2D), velocity field (u, v in x, y directions respectively for Cartesian coordinate system) for an incompressible flow can be expressed in terms of spatial derivatives of a scalar field given by $\psi(x, y, t)$, the *stream function*.

Typically, the following steps are involved in deriving the series coefficients in a Cartesian system (similar details in cylindrical coordinate system are outlined in Appendix A for the interested reader) :

2.2.1 Step I. Expanding the stream function (ψ) in a two-dimensional, infinite Taylor-series form

$$\psi = \sum_{i=1}^{\infty} \sum_{j=0}^{\infty} a_{ij} x^j y^{i+1} \quad (2.1)$$

Where a_{ij} are the series coefficients (which are time dependent), and x and y are stream-

wise and wall-normal coordinates respectively. Note that the lowest power of y in the series is 2. This is so because of the wall boundary conditions:

$$\psi_{y=0} = 0 \quad (2.2)$$

$$u_{y=0} = \left. \frac{\partial \psi}{\partial y} \right|_{y=0} = 0 \quad (2.3)$$

This also guarantees that

$$v_{y=0} = -\left. \frac{\partial \psi}{\partial x} \right|_{y=0} = 0 \quad (2.4)$$

2.2.2 Step II. Expressing the velocity components in series form by differentiating the series for the stream function given by Equation 2.1

Since the series defined for the stream function (ψ) is continuous and differentiable in space, we differentiate it to obtain the series form for the velocity components. Considering the streamwise velocity component (in x direction):

$$u = \frac{\partial \psi}{\partial y} \quad (2.5)$$

$$u = \sum_{i=1}^{\infty} \sum_{j=0}^{\infty} a_{ij} (i+1) x^j y^i \quad (2.6)$$

and the wall-normal velocity component (in y direction):

$$v = -\frac{\partial\psi}{\partial x} \quad (2.7)$$

$$v = -\sum_{i=1}^{\infty} \sum_{j=1}^{\infty} a_{ij}(j)x^{j-1}y^{i+1} \quad (2.8)$$

2.2.3 Step III. Obtaining series expressions for partial derivatives of the velocity components in the momentum equation (the components of which in the x and y directions are given by Equations 2.20 and 2.24 respectively)

Starting with Equation 2.6 and differentiating with respect to x:

$$\frac{\partial u}{\partial x} = \sum_{i=1}^{\infty} \sum_{j=1}^{\infty} a_{ij}(i+1)(j)x^{j-1}y^i \quad (2.9)$$

$$\frac{\partial^2 u}{\partial x^2} = \sum_{i=1}^{\infty} \sum_{j=2}^{\infty} a_{ij}(i+1)(j)(j-1)x^{j-2}y^i \quad (2.10)$$

Similarly, starting with Equation 2.6 but differentiating with respect to y:

$$\frac{\partial u}{\partial y} = \sum_{i=1}^{\infty} \sum_{j=0}^{\infty} a_{ij}(i+1)(i)x^j y^{i-1} \quad (2.11)$$

$$\frac{\partial^2 u}{\partial y^2} = \sum_{i=2}^{\infty} \sum_{j=0}^{\infty} a_{ij}(i+1)(i)(i-1)x^j y^{i-2} \quad (2.12)$$

Starting with Equation 2.8 and differentiating with respect to x:

$$\frac{\partial v}{\partial x} = - \sum_{i=1}^{\infty} \sum_{j=2}^{\infty} a_{ij}(j)(j-1)x^{j-2}y^{i+1} \quad (2.13)$$

Differentiating a second time with respect to x:

$$\frac{\partial^2 v}{\partial x^2} = - \sum_{i=1}^{\infty} \sum_{j=3}^{\infty} a_{ij}(j)(j-1)(j-2)x^{j-3}y^{i+1} \quad (2.14)$$

Similarly, Equation 2.8 is used to obtain the first and second derivatives of v with respect to y:

$$\frac{\partial v}{\partial y} = - \sum_{i=1}^{\infty} \sum_{j=1}^{\infty} a_{ij}(j)(i+1)x^{j-1}y^i \quad (2.15)$$

$$\frac{\partial^2 v}{\partial y^2} = - \sum_{i=1}^{\infty} \sum_{j=1}^{\infty} a_{ij}(i+1)(i)(j)x^{j-1}y^{i-1} \quad (2.16)$$

2.2.4 Step IV. Obtaining expression relating the lowest-order Taylor series coefficients a_{1j} to the wall shear stress using the constitutive equation for Newtonian fluids

Starting with the constitutive equation for Newtonian fluids applied at the wall:

$$\tau_{wall} = \mu \left. \frac{\partial u}{\partial y} \right|_{y=0} \quad (2.17)$$

Substituting the series expression for $\frac{\partial u}{\partial y}$ (Equation 2.11), and evaluating the expression

at the wall i.e. $y = 0$:

$$\tau_{wall} = \mu \sum_{i=1}^{\infty} \sum_{j=0}^{\infty} a_{ij} (i+1)(i) x^j y^{i-1} \Big|_{y=0} \quad (2.18)$$

We observe that, only terms with y^0 will survive (i.e. $i = 1$) and the expression reduces to the form below -

$$\frac{\tau_{wall}}{2\mu} = \sum_{j=0}^{\infty} a_{1j} x^j \quad (2.19)$$

2.2.5 Step V. Obtaining expression relating the next-order Taylor series coefficients a_{2j} to the wall pressure gradient using the momentum equation in the streamwise direction

We use the momentum equation in the streamwise direction (x) and replace all derivatives by their corresponding series forms derived in step 3 above:

$$\rho \left(\frac{\partial u}{\partial t} + u \frac{\partial u}{\partial x} + v \frac{\partial u}{\partial y} \right) = -\frac{\partial p}{\partial x} + \mu \left(\frac{\partial^2 u}{\partial x^2} + \frac{\partial^2 u}{\partial y^2} \right) \quad (2.20)$$

Rearranging terms in Equation 2.20 to obtain series expression for the pressure gradient

in the streamwise (x) direction:

$$\begin{aligned}
& -\frac{1}{\rho} \left(\frac{\partial p}{\partial x} \right) \tag{2.21} \\
& = \sum_{i=1}^{\infty} \sum_{j=0}^{\infty} \dot{a}_{ij} (i+1) x^j y^i \\
& + \sum_{i=1}^{\infty} \sum_{j=0}^{\infty} \sum_{p=1}^{\infty} \sum_{q=1}^{\infty} a_{ij} a_{pq} (i+1)(p+1)(q) x^{j+q-1} y^{i+p} \\
& - \sum_{i=1}^{\infty} \sum_{j=1}^{\infty} \sum_{p=1}^{\infty} \sum_{q=0}^{\infty} a_{ij} a_{pq} (j)(p)(p+1) x^{j+q-1} y^{i+p} \\
& - v \left[\sum_{i=1}^{\infty} \sum_{j=2}^{\infty} a_{ij} (i+1)(j)(j-1) x^{j-2} y^i + \sum_{i=2}^{\infty} \sum_{j=0}^{\infty} a_{ij} (i+1)(i)(i-1) x^j y^{i-2} \right]
\end{aligned}$$

where, \dot{a} indicates differentiation of a with respect to time. If we evaluate Equation 2.21 at the wall,

$$\begin{aligned}
& -\frac{1}{\rho} \left(\frac{\partial p}{\partial x} \right)_{Wall} \tag{2.22} \\
& = \sum_{i=1}^{\infty} \sum_{j=0}^{\infty} \dot{a}_{ij} (i+1) x^j y^i \\
& + \sum_{i=1}^{\infty} \sum_{j=0}^{\infty} \sum_{p=1}^{\infty} \sum_{q=1}^{\infty} a_{ij} a_{pq} (i+1)(p+1)(q) x^{j+q-1} y^{i+p} \\
& - \sum_{i=1}^{\infty} \sum_{j=1}^{\infty} \sum_{p=1}^{\infty} \sum_{q=0}^{\infty} a_{ij} a_{pq} (j)(p)(p+1) x^{j+q-1} y^{i+p} \\
& - v \left[\sum_{i=1}^{\infty} \sum_{j=2}^{\infty} a_{ij} (i+1)(j)(j-1) x^{j-2} y^i + \sum_{i=2}^{\infty} \sum_{j=0}^{\infty} a_{ij} (i+1)(i)(i-1) x^j y^{i-2} \right] \Big|_{y=0}
\end{aligned}$$

In equation 2.22, only terms where the power of y is 0 will survive. Considering each of the terms on the right hand side, the lowest power of y is 1 in the first term, 2 in the second term, 2 in the third term, 1 in the fourth term and 0 in the last term. Thus, only the last term has components that do not vanish at the wall, giving an expression for the wall-pressure gradient in the streamwise direction in terms of a_{2j} :

$$\frac{1}{6\mu} \left(\frac{\partial p}{\partial x} \right)_{wall} = \sum_{j=0}^{\infty} a_{2j} x^j \quad (2.23)$$

2.2.6 Step VI. Obtaining expressions for higher-order Taylor series coefficients in terms of a_{1j} and a_{2j} and their time derivatives by successive differentiation (in the wall-normal direction) of the 2D momentum equations and evaluating the result at the wall

The series expression of the streamwise momentum equation is given by Equation 2.21 above.

The momentum equation in the wall-normal (y) direction is given by-

$$\rho \left(\frac{\partial v}{\partial t} + u \frac{\partial v}{\partial x} + v \frac{\partial v}{\partial y} \right) = -\frac{\partial p}{\partial y} + \mu \left(\frac{\partial^2 v}{\partial x^2} + \frac{\partial^2 v}{\partial y^2} \right) \quad (2.24)$$

Substituting for series expressions of the velocity components and their derivatives (obtained in step 3):

$$\begin{aligned}
& -\frac{1}{\rho} \left(\frac{\partial p}{\partial y} \right) \tag{2.25} \\
& = \sum_{i=1}^{\infty} \sum_{j=1}^{\infty} \dot{a}_{ij} (i+1)(j) x^{j-1} y^{i+1} \\
& - \sum_{i=1}^{\infty} \sum_{j=0}^{\infty} \sum_{p=1}^{\infty} \sum_{q=2}^{\infty} a_{ij} a_{pq} (i+1)(q)(q-1) x^{j+q-2} y^{i+p+1} \\
& + \sum_{i=1}^{\infty} \sum_{j=1}^{\infty} \sum_{p=1}^{\infty} \sum_{q=1}^{\infty} a_{ij} a_{pq} (j)(q)(p+1) x^{j+q-2} y^{i+p+1} \\
& + v \left[\sum_{i=1}^{\infty} \sum_{j=3}^{\infty} a_{ij} (j)(j-1)(j-2) x^{j-3} y^{i+1} + \sum_{i=1}^{\infty} \sum_{j=1}^{\infty} a_{ij} (i+1)(i)(j) x^{j-1} y^{i-1} \right]
\end{aligned}$$

We combine the expressions for both momentum equations (2.21 and 2.25) and rearrange the terms in such a way that the highest starting value of index i , relating to the series order with respect to y , in the summation will be on the left hand side and other lower-order y terms appear on the right hand side. To do so, we first take the derivative with respect to y of Equation 2.21, and exchange the order of the x and y derivatives of the pressure on the left hand side. Subsequently, Equation 2.25 is used to express $\frac{\partial p}{\partial y}$ in the resulting equation in terms of series expansion. This leads to:

$$\begin{aligned}
& v \sum_{i=3}^{\infty} \sum_{j=0}^{\infty} a_{ij}(i+1)(i)(i-1)(i-2)x^j y^{i-3} \tag{2.26} \\
&= \sum_{i=1}^{\infty} \sum_{j=0}^{\infty} \dot{a}_{ij}(i)(i+1)x^j y^{i-1} + \sum_{i=1}^{\infty} \sum_{j=2}^{\infty} \dot{a}_{ij}(j)(j-1)x^{j-2} y^{i+1} \\
&+ \sum_{i=1}^{\infty} \sum_{j=0}^{\infty} \sum_{p=1}^{\infty} \sum_{q=1}^{\infty} a_{ij} a_{pq}(i+1)(p+1)(q)(i+p)x^{j+q-1} y^{i+p-1} \\
&- \sum_{i=1}^{\infty} \sum_{j=1}^{\infty} \sum_{p=1}^{\infty} \sum_{q=0}^{\infty} a_{ij} a_{pq}(j)(p+1)(p)(i+p)x^{j+q-1} y^{i+p-1} \\
&+ \sum_{i=1}^{\infty} \sum_{j=0}^{\infty} \sum_{p=1}^{\infty} \sum_{q=0}^{\infty} a_{ij} a_{pq}(i+1)(q)(q-1)(j+q-2)x^{j+q-3} y^{i+p+1} \\
&- \sum_{i=1}^{\infty} \sum_{j=1}^{\infty} \sum_{p=1}^{\infty} \sum_{q=1}^{\infty} a_{ij} a_{pq}(p+1)(q)(j)(j+q-2)x^{j+q-3} y^{i+p+1} \\
&- v \left[2 \sum_{i=1}^{\infty} \sum_{j=2}^{\infty} a_{ij}(i+1)(i)(j)(j-1)x^{j-2} y^{i-1} \right] \\
&- v \left[\sum_{i=1}^{\infty} \sum_{j=4}^{\infty} a_{ij}(j)(j-1)(j-2)(j-3)x^{j-4} y^{i+1} \right]
\end{aligned}$$

By applying Equation 2.26 at the wall, *i.e.* setting $y = 0$, we obtain equations for a_{3j} in terms of a_{1j} , a_{2j} and their time derivatives. To obtain expressions for a_{4j} . Equation 2.26 is differentiated with respect to y , and the result is evaluated at the wall. The process can continue indefinitely in this recursive manner to derive expressions for any a_{ij} ($i > 2$) in terms of a_{1j} , a_{2j} and their time derivatives.

Some low-order coefficients were hand-derived initially to understand the process of obtaining these coefficients prior to developing a MATLAB[®] program to automate the deriva-

tion process. Given below are sample hand-derived expressions for some coefficients of the series. In addition to clarifying the derivation process, the hand-derived expressions were also helpful in validating the those obtained from the MATLAB[®] program.

$$a_{30} = \frac{1}{24\nu}[2\dot{a}_{10} - 8\nu a_{12}] \quad (2.27)$$

$$a_{31} = \frac{1}{24\nu}[2\dot{a}_{11} - 24\nu a_{13}] \quad (2.28)$$

$$a_{37} = \frac{1}{24\nu}[2\dot{a}_{17} - 288\nu a_{19}] \quad (2.29)$$

$$a_{40} = \frac{1}{120\nu}[6\dot{a}_{20} + 4a_{10}a_{11} - 24\nu a_{22}] \quad (2.30)$$

$$a_{41} = \frac{1}{120\nu}[6\dot{a}_{21} + 8a_{10}a_{12} + 4a_{11}^2 - 72\nu a_{23}] \quad (2.31)$$

$$a_{42} = \frac{1}{120\nu}[6\dot{a}_{22} + 12a_{10}a_{13} + 12a_{11}a_{12} - 144\nu a_{24}] \quad (2.32)$$

$$a_{50} = \frac{1}{720\nu}[24\dot{a}_{30} + 4\dot{a}_{12} + 24a_{10}a_{21} - 48\nu a_{14} - 96\nu a_{32}] \quad (2.33)$$

2.3 Demonstration In Laminar Flows With Known Analytical Solution

In order to accurately estimate the velocity profile above the wall, it may be necessary to employ high-order Taylor series expansion. As seen from Equation 2.26, the expressions for the series coefficients become more complex at higher order. The underlying process to derive these coefficients also becomes too time consuming and tedious. Therefore, it is important to automate the process of computing the series coefficients up to any arbitrary order. To this end, MATLAB[®] programs are designed and built based on the process

mentioned in section 2.2 to compute coefficients up to any arbitrary order. The resulting expressions are saved and used directly in expansion of series for different applications, to avoid re-deriving the expressions for each flow situation, and hence reduce computational time. However, prior to using the MATLAB-derived coefficient expressions, it is important to validate these coefficients. This is done in two ways: (1) for low-order coefficients up to order 2, the MATLAB[®] expressions are compared to their analytically-derived counterpart; (2) by comparing estimations of simple flows with their analytical solutions. Table 2.1 summarizes the different types of flow analyzed for the purpose of validation.

Table 2.1: Analytical flows employed in validation of MATLAB[®] code used to derive Taylor series coefficients

Case No.	Flow	Nature of flow
1.	Blasius Boundary Layer	<ol style="list-style-type: none"> 1. 2D Steady flow. 2. Only wall-shear stress information is required to obtain series coefficients. 3. Zero pressure gradient.
2.	Falkner-Skan Boundary Layer (m = 1)	<ol style="list-style-type: none"> 1. 2D Steady flow. 2. Stagnation line flow. 3. Wall-shear stress and wall-pressure gradient information is required to obtain series coefficients. 4. Flow with favorable pressure gradient. 5. The streamwise wall-shear stress and the wall-pressure gradient are linear.
3.	Stokes Stream Oscillating Problem	<ol style="list-style-type: none"> 1. Unsteady flow. 2. Wall-shear stress and wall pressure gradient is sinusoidal in time. 3. Series coefficients are computed dynamically.

It is important to note that when validating the series predictions against analytical solutions, both the wall-shear stress and wall-pressure are available in analytical forms that can be differentiated up to an arbitrary order without loss of accuracy. Therefore these valida-

tion cases enable verifications of the complex analytical forms obtained from the MATLAB[®] program to relate the high-order series coefficients to the wall-shear and wall-pressure series coefficients. They also help to provide a sense of the speed of convergence of the series. On the other hand, the validation process does not provide an assessment of the effect of the accuracy of the wall shear stress and pressure, and their derivatives up to the required order, on the estimation accuracy.

2.3.1 Blasius Boundary Layer

The following derivation may be found in most standard textbooks on fluid mechanics (e.g. Panton [9], pages 498:501).

Blasius boundary layer is a 2D steady boundary layer formed on a semi-infinite plate oriented parallel to the flow direction. The solution is expressed in terms of a similarity variable in the wall-normal direction:

$$\eta = y\sqrt{\frac{U_0}{2x\nu}} \quad (2.34)$$

Where, y is the the wall-normal coordinate measured from the plate, x is the distance along the plate, U_0 is the free stream velocity and ν is the kinematic viscosity.

For a Blasius boundary layer problem, the wall-shear stress is given by:

$$\tau_{wall} = \mu U_0 f''(0) \sqrt{\frac{U_0}{2x\nu}} \quad (2.35)$$

where $\frac{u}{U_0} = f'(\eta)$. Equation 2.35 may be simplified to:

$$\tau_{wall} = \frac{\Omega}{\sqrt{x}} \quad (2.36)$$

where,

$$\Omega = \mu U_0 f''(0) \sqrt{\frac{U_0}{2\nu}} \quad (2.37)$$

The Taylor series coefficients in this case can be derived from knowledge of the wall-shear stress only due to the absence of pressure-gradient. To do so, the coefficients of the infinite series for τ_{wall} (on the left hand side of the Equation 2.19) are first computed as follows -

$$\begin{aligned} \sum_{j=0}^{\infty} a_{1j} x^j & \quad (2.38) \\ &= \frac{1}{2\mu} (\tau_{wall}) \frac{x^0}{0!} + \frac{1}{2\mu} \frac{\partial}{\partial x} (\tau_{wall}) \frac{x^1}{1!} + \frac{1}{2\mu} \frac{\partial^2}{\partial x^2} (\tau_{wall}) \frac{x^2}{2!} \\ &+ \frac{1}{2\mu} \frac{\partial^3}{\partial x^3} (\tau_{wall}) \frac{x^3}{3!} + \frac{1}{2\mu} \frac{\partial^4}{\partial x^4} (\tau_{wall}) \frac{x^4}{4!} + \dots \end{aligned}$$

Equation 2.38 can be rewritten by substituting for τ_{wall} from Equation 2.36 to get:

$$\begin{aligned} \sum_{j=0}^{\infty} a_{1j} x^j & \quad (2.39) \\ &= \frac{1}{2\mu} \left(\frac{\Omega}{\sqrt{x}} \right) + \frac{1}{2\mu} \frac{(-1)\Omega x^1}{2x^{\frac{3}{2}} 1!} + \frac{1}{2\mu} \frac{(-1)(-3)\Omega x^2}{2^2 x^{\frac{5}{2}} 2!} \\ &+ \frac{1}{2\mu} \frac{(-1)(-3)(-5)\Omega x^3}{2^3 x^{\frac{7}{2}} 3!} + \frac{1}{2\mu} \frac{(-1)(-3)(-5)(-7)\Omega x^4}{2^4 x^{\frac{9}{2}} 4!} + \dots \end{aligned}$$

Comparing the LHS and the RHS in Equation 2.39, expressions for and any a_{1j} may be obtained, such as:

$$a_{10} = \frac{1}{0!} \frac{\Omega}{2^\mu} \frac{1}{x^{\frac{1}{2}}} \quad (2.40)$$

$$a_{11} = \frac{1}{1!} \frac{\Omega}{2^\mu} \frac{(-1)}{2x^{\frac{3}{2}}} \quad (2.41)$$

$$a_{12} = \frac{1}{2!} \frac{\Omega}{2^\mu} \frac{(-1)(-3)}{2^2 x^{\frac{5}{2}}} \quad (2.42)$$

$$a_{13} = \frac{1}{3!} \frac{\Omega}{2^\mu} \frac{(-1)(-3)(-5)}{2^3 x^{\frac{7}{2}}} \quad (2.43)$$

$$a_{14} = \frac{1}{4!} \frac{\Omega}{2^\mu} \frac{(-1)(-3)(-5)(-7)}{2^4 x^{\frac{9}{2}}} \quad (2.44)$$

Where x is the location at the wall where the series expansion is obtained. Given the above coefficients, and similar higher order ones, the Taylor-series expansion for $u(y)$ (Equation 2.6) may be written as:

$$u(y) = 2a_{10}y + 3a_{20}y^2 + 4a_{30}y^3 + 5a_{40}y^4 + 6a_{50}y^5 + \dots \quad (2.45)$$

Or, using the expressions 2.27 through 2.33 and similar higher-order ones:

$$\begin{aligned} u(y) = & 2a_{10}y + 3a_{20}y^2 + \frac{4}{24\nu}[2\dot{a}_{10} - 8\nu a_{12}]y^3 \\ & + \frac{5}{120\nu}[6\dot{a}_{20} + 4a_{10}a_{11} - 24\nu a_{22}]y^4 \\ & + \frac{6}{720\nu}[24\dot{a}_{30} + 4\dot{a}_{12} + 24a_{10}a_{21} - 48\nu a_{14} - 96\nu a_{32}]y^5 + \dots \end{aligned} \quad (2.46)$$

Eliminating terms containing the time derivatives (since the flow is steady) and a_{2j} (since

$\frac{\partial p}{\partial x} = 0$) from Equation 2.46:

$$u(y) = 2a_{10}y - \frac{4}{3}a_{12}y^3 + \frac{a_{10}a_{11}}{6\nu}y^4 - \frac{2\nu a_{14}}{5\nu}y^5 + \dots \quad (2.47)$$

Figure 2.1 shows different-order expansions of Taylor-series to estimate the streamwise velocity profile in the Blasius boundary layer, plotted in similarity variables. Expansions up to the 45th order where the order represents the order of y in the *stream function*, are depicted in the figure and compared to the exact solution.

Two main observations can be made from Figure 2.1. First, the series expansion coincides exactly with the solution over a certain η range, beyond which the series diverges. The η range over which the agreement is accomplished becomes progressively bigger with increasing series order. This provides validation of the MATLAB[®] code used to derive the series coefficients. Specifically, the results show the appropriate behavior of a series expression of the solution that increases in accuracy with increasing number of terms in the series. This complements the validation done by comparing the code's output to hand-derived expressions (which could only be done for very low-order expressions).

A second observation is that the series convergence appears to be very slow. Though the lowest order series expansion shown (5th order) accurately captures the velocity profile over more than third of the 99% boundary layer thickness ($\eta = 4.9$), accurate representation over the full boundary layer thickness is not possible even with as high of an order as 45th.

2.3.2 Falkner-Skan Boundary Layer ($m = 1$)

The following derivation may be found in most standard textbooks on fluid mechanics (e.g. Panton [9], pages 508:512).

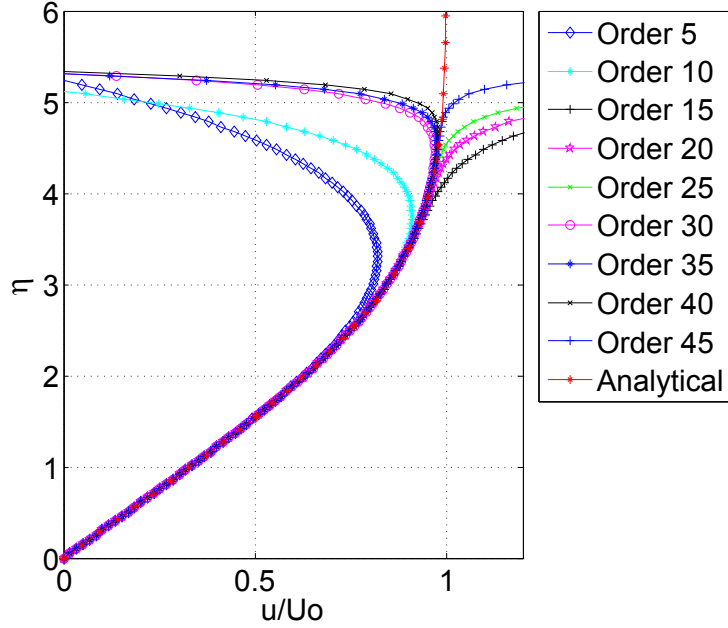


Figure 2.1: Series expansions up to the 45th order of the streamwise velocity compared to the analytical solution for Blasius boundary layer. (For interpretation of the references to color in this and all other figures, the reader is referred to the electronic version of this thesis.)

The Flakner-skan boundary layer problem with favorable pressure gradient ($m = 1$) is a steady state stagnation flow whose self-similar solution is expressed in terms of the following similarity variable in the wall-normal direction:

$$\eta = \frac{y}{L} \sqrt{Re} \quad (2.48)$$

Where, y is the wall-normal coordinate, L is a characteristic length, Re is Reynolds number based on L and u_0 , and u_e is the external velocity ($u_e(x) = u_0(\frac{x}{L})$); x being the streamwise coordinate.

The Falkner-Skan solution is given by-

$$u(x, y) = u_0 \left(\frac{x}{L} \right) f'(\eta) \quad (2.49)$$

Differentiating Equation 2.49 with respect to y :

$$\frac{\partial u}{\partial y} = \frac{u_0 \sqrt{Re}}{L} f''(\eta) \frac{x}{L} \quad (2.50)$$

$$\frac{\partial^2 u}{\partial^2 y} = \frac{u_0 Re}{L^2} f'''(\eta) \frac{x}{L} \quad (2.51)$$

and the shear-stress on the wall:

$$\tau_{wall} = \mu \frac{u_0 \sqrt{Re}}{L} f''(0) \frac{x}{L} \quad (2.52)$$

We substitute $Re = \frac{u_0 L}{\nu}$ in Equation 2.52 to get a function for τ_{wall} :

$$\tau_{wall} = \frac{\mu}{\sqrt{\nu}} \left(\frac{u_0}{L}\right)^{\frac{3}{2}} f''(0) x \quad (2.53)$$

Now, the x-momentum equation (Equation 2.20) if evaluated at the wall reduces to:

$$\left. \frac{\partial p}{\partial x} \right|_{wall} = \mu \left. \frac{\partial^2 u}{\partial^2 y} \right|_{y=0} \quad (2.54)$$

Combining equations 2.54 and 2.51:

$$\left. \frac{\partial p}{\partial x} \right|_{wall} = \rho \left(\frac{u_0}{L}\right)^2 f'''(0) x \quad (2.55)$$

From Equations 2.53 and 2.55, it is evident that, the wall-shear stress and wall-pressure gradient are linear in x . We now set the characteristic length L to 1 m and free stream velocity u_0 to 1 m/s for simplicity of calculations. If we compare 2.53 with the Equation

2.19, we get the coefficients a_{1j} 's as below-

$$a_{10} = 0 \quad (2.56)$$

$$a_{11} = \frac{f''(0)}{2\sqrt{\nu}} \quad (2.57)$$

$$a_{12}, a_{13}, a_{14}, \dots, a_{1\infty} = 0 \quad (2.58)$$

Similarly, if we compare 2.55 with the Equation 2.23, we get coefficients a_{2j} 's as below-

$$a_{20} = 0 \quad (2.59)$$

$$a_{21} = \frac{f'''(0)}{6\nu} \quad (2.60)$$

$$a_{22}, a_{23}, a_{24}, \dots, a_{2\infty} = 0 \quad (2.61)$$

Given the above coefficients (Equations 2.56 through 2.61), and similar higher order ones ($a_{nj}; n > 2$), the Taylor-series expansion for $u(y)$ (Equation 2.6) can be written as:

$$\begin{aligned} u(y) = & (2a_{10}y + 3a_{20}y^2 + 4a_{30}y^3 + \dots) \\ & + (2a_{11}y + 3a_{21}y^2 + 4a_{31}y^3 + 5a_{41}y^4 + 6a_{51}y^5 + \dots)x \\ & + (2a_{12}y + 3a_{22}y^2 + 4a_{32}y^3 + \dots)x^2 + \dots \end{aligned} \quad (2.62)$$

Combining Equations 2.62, 2.56 through 2.61 and 2.27 through 2.33:

$$u(y) = (2a_{11}y + 3a_{21}y^2 + \frac{a_{11}^2}{6\nu}y^4 + \dots)x \quad (2.63)$$

Or (recalling, $u_e(x) = u_0(\frac{x}{L})$, $u_0 = L = 1$),

$$\frac{u}{u_e} = 2a_{11}y + 3a_{21}y^2 + \frac{a_{11}^2}{6\nu}y^4 + \dots \quad (2.64)$$

Figure 2.2 shows the expansions of Taylor-series to estimate the streamwise velocity profile of ($m = 1$) boundary layer. Similar to the Blasius boundary layer case, comparison with the exact solution gives confidence in the MATLAB[®] code used to calculate the series coefficients. Unlike the Blasius boundary layer case, here the derived coefficients depend also on the wall pressure gradient. Thus, the results give added validation of terms in the coefficient expressions that are related to the wall pressure gradient. It is also noted here that the series convergence seen in Figure 2.2 is also found to be very slow, with the 45th series not able to accurately estimate the velocity over the entire boundary layer thickness.

2.3.3 Stokes Oscillating Stream Problem

The following derivation may be found in most standard textbooks on fluid mechanics (e.g. Panton [9], pages 221:224).

Stokes Oscillating stream problem is an unsteady flow (sinusoidal in time) that helps us validate Taylor-series-coefficient expressions that contain high-order time derivatives of the wall-shear stress and the wall-pressure gradient. This also helps us validate the Taylor-series-based flow-estimation due to dynamically changing coefficients.

The oscillating free-stream problem is analyzed based on the assumption that the fluid has a single velocity component $u(y, t)$. The x-momentum equation in this case reduces to:

$$\frac{\partial P}{\partial X} = \frac{\partial^2 U}{\partial^2 Y} - \frac{\partial U}{\partial T} \quad (2.65)$$

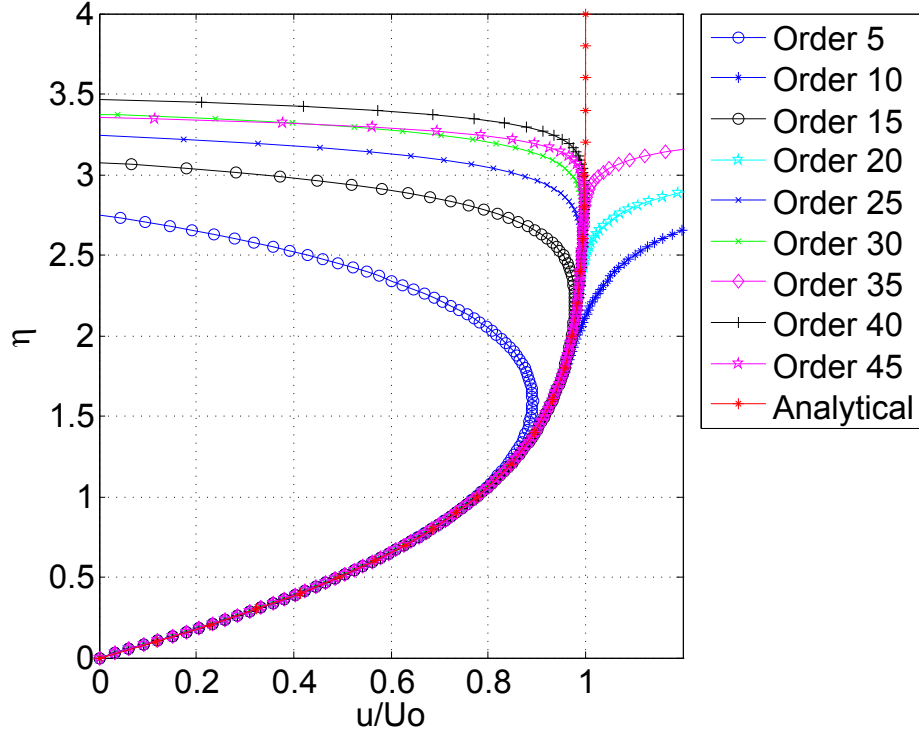


Figure 2.2: Series expansions up to the 45th order of the streamwise velocity compared to the analytical solution for Falkner-Skan ($m = 1$) boundary layer

Where - $P = \frac{p}{\rho u_0 \Omega L}$, $X = \frac{x}{L}$, $U = \frac{u}{u_0}$, Ω is the frequency of oscillation (s^{-1}), L is a characteristic length, u_0 is the free stream velocity, Y is similarity variable defined as $Y = y\sqrt{\frac{\Omega}{\nu}}$, and T is the time similarity variable defined as $T = \Omega t$.

The solution to the above problem subject to the boundary conditions associated with a uniform stream oscillating above a fixed wall is given by:

$$U(y, t) = -\sin\left(T - \frac{Y}{\sqrt{2}}\right) \exp\left(-\frac{Y}{\sqrt{2}}\right) + \sin T \quad (2.66)$$

Differentiating 2.66 with respect to T:

$$\frac{\partial U}{\partial T} = -\cos\left(T - \frac{Y}{\sqrt{2}}\right) \exp\left(-\frac{Y}{\sqrt{2}}\right) + \cos T \quad (2.67)$$

Differentiating 2.66 with respect to Y twice:

$$\frac{\partial U}{\partial Y} = \frac{\exp(-\frac{Y}{\sqrt{2}})}{\sqrt{2}} \left[\sin\left(T - \frac{Y}{\sqrt{2}}\right) + \cos\left(T - \frac{Y}{\sqrt{2}}\right) \right] \quad (2.68)$$

$$\frac{\partial^2 U}{\partial^2 Y} = -\cos\left(T - \frac{Y}{\sqrt{2}}\right) \exp\left(-\frac{Y}{\sqrt{2}}\right) \quad (2.69)$$

Combining equations 2.65, 2.67, 2.69 and evaluating at the wall ($Y = 0$):

$$\left. \frac{\partial P}{\partial X} \right|_{wall} = -\cos T \quad (2.70)$$

Evaluating 2.68 at the wall ($Y = 0$) and combining with 2.19 to obtain the series expression for τ_{wall} , we get:

$$\sum_{j=0}^{\infty} a_{1j} x^j = \frac{1}{2\sqrt{2}} (\sin T + \cos T) \quad (2.71)$$

It is evident from 2.71 that the wall-shear stress is *independent* of X . Therefore, we get:

$$a_{10} = \frac{1}{2\sqrt{2}} (\sin T + \cos T) \quad (2.72)$$

$$a_{11}, a_{12}, a_{13}, a_{14}, \dots, a_{1\infty} = 0 \quad (2.73)$$

Similarly, comparing Equation 2.70 and 2.23, we get:

$$a_{20} = -\frac{\cos T}{6\mu} \quad (2.74)$$

$$a_{21}, a_{22}, a_{23}, a_{24}, \dots, a_{2\infty} = 0 \quad (2.75)$$

Given the above coefficients, and similar higher order ones, the Taylor-series expansion

for U (Equation 2.6) can be written as:

$$U = 2a_{10}Y + 3a_{20}Y^2 + 4a_{30}Y^3 + 5a_{30}Y^4 + 6a_{30}Y^5 + \dots \quad (2.76)$$

Combining Equations 2.76, 2.72 through 2.75:

$$U = 2a_{10}Y + 3a_{20}Y^2 + \frac{\dot{a}_{10}}{3\nu}Y^3 + \frac{\dot{a}_{20}}{4\nu}Y^4 + \frac{\ddot{a}_{10}}{60\nu^2}Y^5 + \dots \quad (2.77)$$

It is important to note that, for this problem all the higher-order spatial derivatives are *zero* but time-derivatives (up to any order) of a_{10} and a_{20} exist, thereby making the coefficients of the Cartesian Taylor-series completely independent of spatial derivatives.

Figures 2.3a, 2.3b, 2.3c, 2.3d, 2.3e show expansions to capture the boundary layer profile using series up to the order of 45 for different time periods. It is observed that the near-wall region, where the largest variation in the velocity takes place, was captured by the 10th order series but even the 45th order series is not sufficient to capture the entire flat zone of the profile. The convergence rate is relatively faster compared to Blasius boundary layer and Falkner-Skan.

2.4 Summary

Some of the key findings of the present chapter are:

1. The constructed MATLAB[®] programs are capable of generating Taylor-series coefficients up to any order accurately.
2. The agreement of series prediction with the theoretical solution gets progressively better with increasing order of the expansion, *but*, with a very slow rate of convergence.

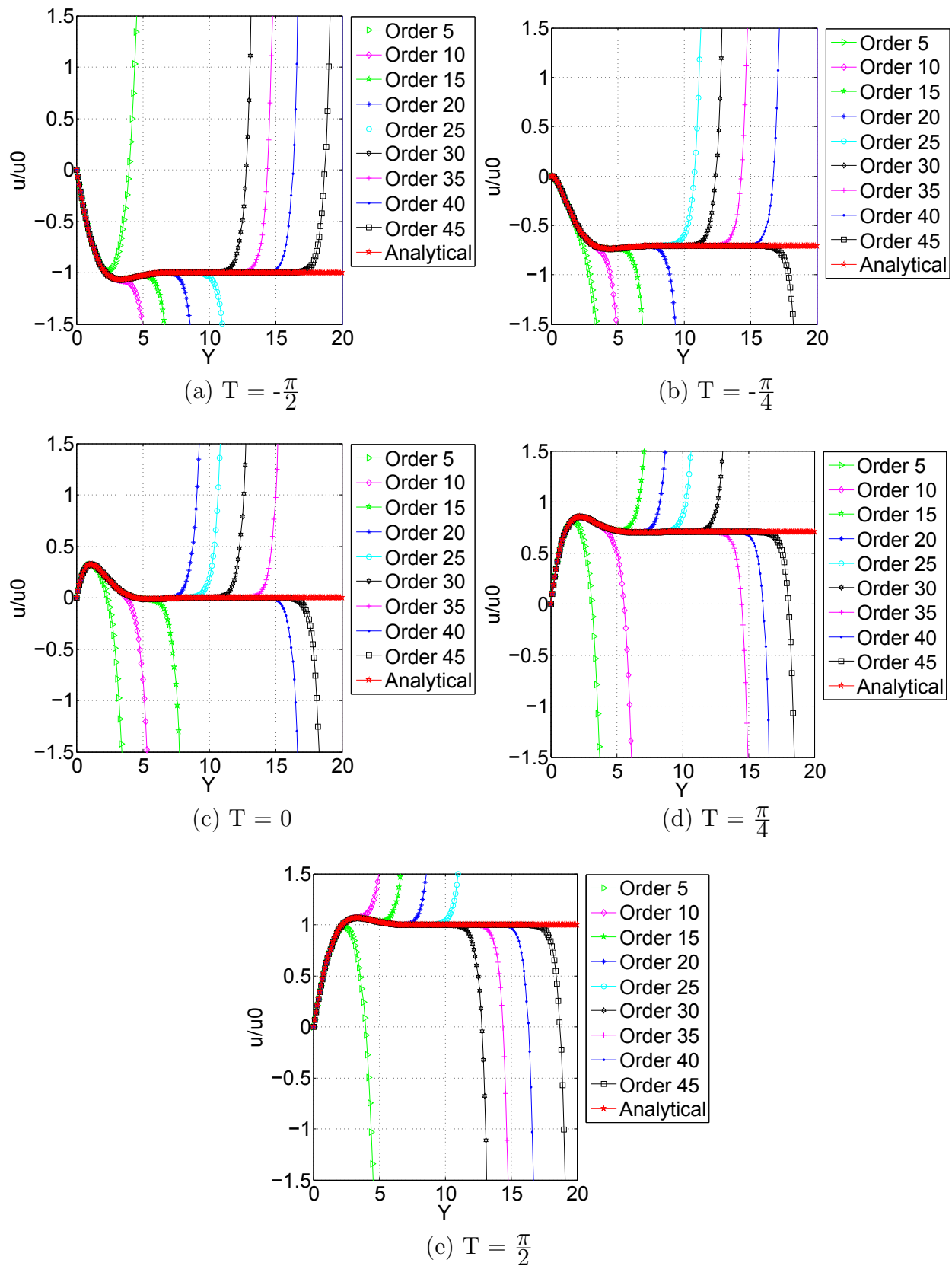


Figure 2.3: Series expansions up to the 45th order of the streamwise velocity compared to the analytical solution for Stokes oscillating stream flow. Different plots represent different phases of the oscillation cycle

3. The domain of convergence of the series expansion (for up to the order of 45) is less than the boundary layer thickness (except in the case of the unsteady Stokes flow, where the convergence seems faster).

Chapter 3

Validation of The Computational Approach

Having validated the concept to determine the flow field from knowledge of wall-stress information (without knowing the far-field boundary condition) using the Taylor-series based expansion model, it is now required to examine the feasibility of this concept to estimate a flow field that is relevant to the wake-vortex problem. As discussed in Chapter 1, the selected problem is that of a counter rotating line-vortex pair impinging on a wall. For the purpose of assessing the Taylor-series model it is necessary to have space-time information of the flow field and associated wall stresses. The latter can then be used in conjunction with the Taylor-series model to estimate the velocity field and compare the outcome with the actual field.

Numerical calculation, employing Fluent, is used to produce the required database of the vortex pair impinging on a wall. However, prior to using the database to validate the Taylor series, it is necessary to ensure the accuracy of the computation. Ideally, this would be done

by comparing against experimental data of the same flow problem. Unfortunately, no such data were available. Instead, it was possible to obtain experimental data in the closely-related problem of an axisymmetric vortex ring impinging on a wall. Thus, simulation of the axisymmetric problem was undertaken first to validate the computational approach and the choice of numerical parameters (grid resolution, domain size, time step, etc). Once confidence was established in the latter, the same numerical approach and parameters were used for computing the Cartesian counterpart problem of line vortex pair. In this chapter, details of the computation of the axisymmetric configuration and validation against experimental data are described. Information regarding the Cartesian-configuration computation and its use to assess the Taylor-series model are left to the following chapter.

3.1 Background

The experimental data used for validation were generated in a study done at Turbulent Mixing and Unsteady Aerodynamics Laboratory (TMUAL) at Michigan State University (MSU) by Gendrich *et al.* [3]. This study was done for a vortex ring approaching a solid wall (i.e. axisymmetric co-ordinate system).

This flow can be simulated using the proprietary code - ANSYS[®]-Fluent. Confidence that such a computational model will provide results that match quantitatively with the known experimental data is based on a study by Fabris *et al.* [5] who developed in-house code to simulate a vortex ring impinging on a wall and did quantitative comparisons with experiments.

The following steps are followed to generate the required numerical data set for final estimations -

1. Analyze the experiments performed by Gendrich *et al.* [3] to determine the initial conditions of the simulation that are consistent with the experiment.
2. Compare the simulation results with those from the experiments.
3. Optimize the simulation parameters, such as the time step, grid resolution, etc. by quantitative comparison with the experimental results.
4. Finalize parameters for the simulated model of the vortex ring problem.
5. Use the parameters fixed for the axisymmetric simulations and simulate the 2D planar counterpart problem of the counter-rotating vortex pair.
6. The results from step 5 are then employed to generate the numerical data used to assess the feasibility of using the Taylor series model to estimate vortex-dominated flows.

3.2 Description of The Experimental Data

3.2.1 Credits

The description in this *entire section* is based on the paper by Gendrich *et al.* [3]. Kindly refer to this paper for more detailed illustration.

3.2.2 Introduction

The flow-field due to vortex ring interaction with a solid wall was studied using 2-color Laser-Induced Fluorescence (LIF) and Molecular Tagging Velocimetry (MTV). A high Reynolds number, based on circulation, ($Re_\Gamma = 4500$) vortex ring was introduced in a flow-domain and allowed to traverse under the action of self-induced velocity to interact with the wall.

This section gives a description of the experimental set up, MTV data, wall signature study due to impingement of a vortex ring.

3.2.3 Experimental Facility

As seen in 3.1, a gravity-driven vortex ring generator was used to introduce a 0.06 m long slug of water from a vertical tube for a short duration of time (0.5 seconds) controlled by a solenoid valve. During the solenoid actuation, the head change was very small, less than 3×10^{-4} m. The wall was placed at a distance of 0.07 m normal to the vortex ring generator axis. The initial vortex ring diameter was approximated to be $D_0 = 0.0364$ m (Figure 3.1) and the ring convection speed was $U_0 = 0.051$ m/s. The resulting Reynolds number based on the initial ring diameter was 1860 and 4500 based on the initial circulation ($\Gamma_0 = 45 \times 10^{-4}$ m²/s).

The velocity field was quantified using Molecular Tagging Velocimetry (MTV). This method is a non-intrusive flow diagnostic which measures two components of the velocity simultaneously at many points in a 2D plane.

3.2.4 Observations

The vortex ring interaction with the wall exhibits different stages as it convects down from the time it was introduced. Some of the prominent observations as seen in Figure 3.3 and 3.4 are listed below. These observations are consistent with those published by Fabris *et al.* [5], Chu *et al.* [6], Orlandi *et al.* [7], Naguib *et al.* [8].

1. Vortex stretching effect is observed as the ring convects towards the wall. This is discerned from the apparent reduction in the core size of the vortex ring.

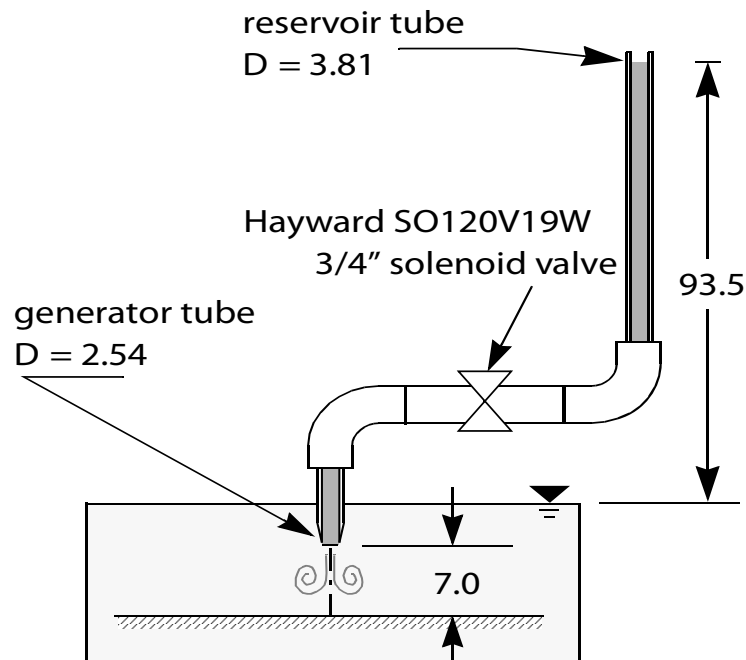


Figure 3.1: Experimental Set up (units are in cm) - Axisymmetric vortex impinging on a wall [3]

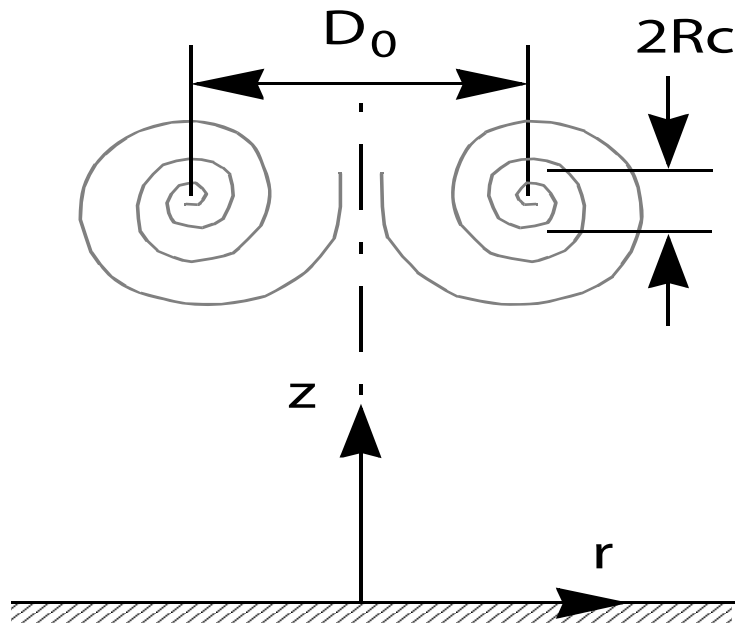


Figure 3.2: Coordinate axes, $D_0 = 0.0364$ m and the core diameter $2R_c = 1.06$ cm (used in this thesis as $R_c = 0.0053$ m[3])

2. Viscous boundary layer growth is observed on the solid wall (light-colored dye).
3. The vortex ring causes boundary layer separation ($t = 1.7$ s in Figure 3.3).
4. The separated boundary layer forms a secondary vortex having opposite vorticity to that of the primary vortex (marked with light-colored dye in Figure 3.3 at $t = 1.8$ s). The secondary vortex is seen to orbit around the primary one before traveling upwards under self-induction effects ($t = 2.0$ to 3.8 s in Figure 3.3).
5. A tertiary vortex is also seen to form from boundary layer separation (see the outer edges of the image at $t = 2.67$ s in Figure 3.3).

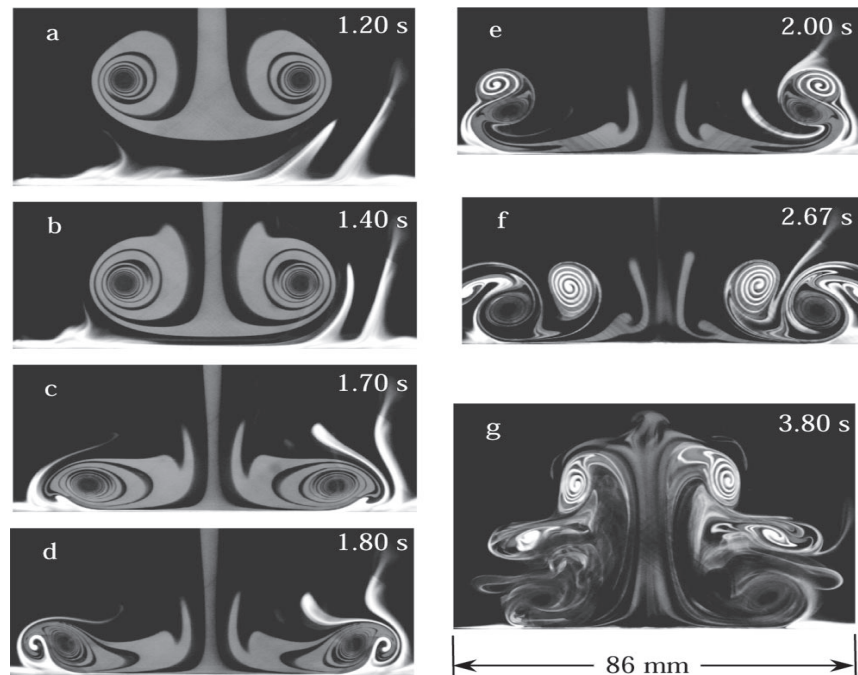


Figure 3.3: Flow visualization using LIF [3]

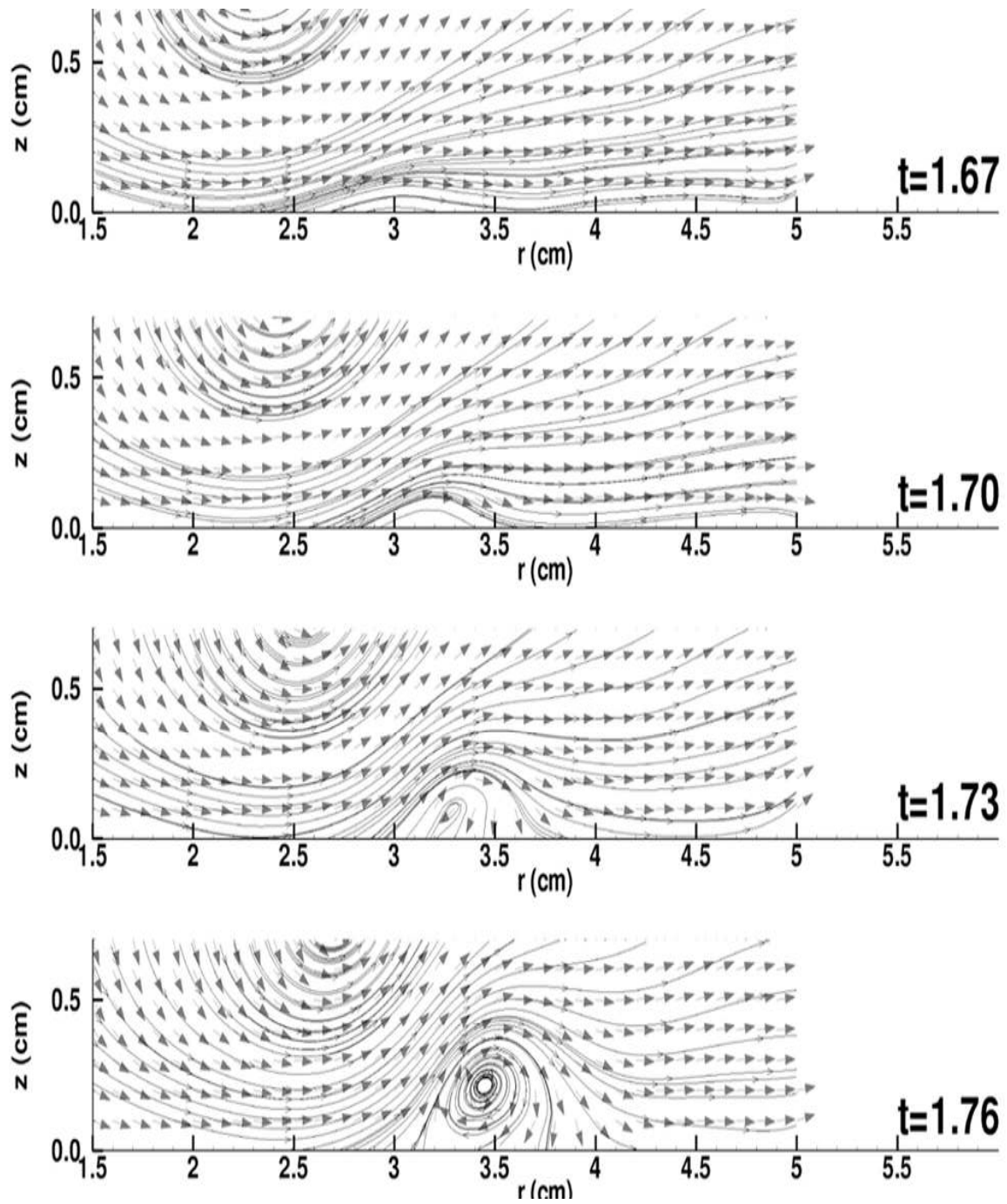


Figure 3.4: Near-wall velocity vectors, time in *seconds* [3]

3.3 Initial Conditions For The Simulation Model

In order to simulate the vortex ring interaction with the wall, an axisymmetric grid was generated in Gambit. The numerical simulation was done using ANSYS[®]-Fluent solver. The solver restricts the horizontal axis to be the symmetry axis for axisymmetric problems. Hence, the geometry of the simulated problem is as shown in Figure 3.5 with the impingement wall oriented vertically and the vortex ring's axis is horizontal. Different approaches may be used to initialize the computation. One method is to directly use experimental data at a time instant that is early during the vortex ring evolution. In such an approach, one would need to interpolate the measurements in order to map the experimental velocity data onto the much finer computational grid. In the present work, such interpolation is avoided by modeling the initial velocity field as that associated with a finite viscous core vortex having Gaussian vorticity distribution. Gendrich *et al.*[3] showed that such a model represents the actual vorticity distribution with good accuracy.

A user-defined function (UDF) was written in C and 'hooked' to the fluent solver to compute the radial and wall-normal velocity components induced by the 'Gaussian-core' vortex and initialize the calculation. The specific characteristics of the vortex model (i.e. initial circulation, core-radius, and core-center location) were determined from the experimental data as described in the following section.

3.3.1 Gaussian Vorticity Distribution

The Gaussian vorticity distribution underlying the velocity field used to initialize the computation is given by -

$$\omega_{\theta} = \omega_0 e^{-\left(\frac{(r-r_{peak})^2 + (z-z_{peak})^2}{R_c^2}\right)} \quad (3.1)$$

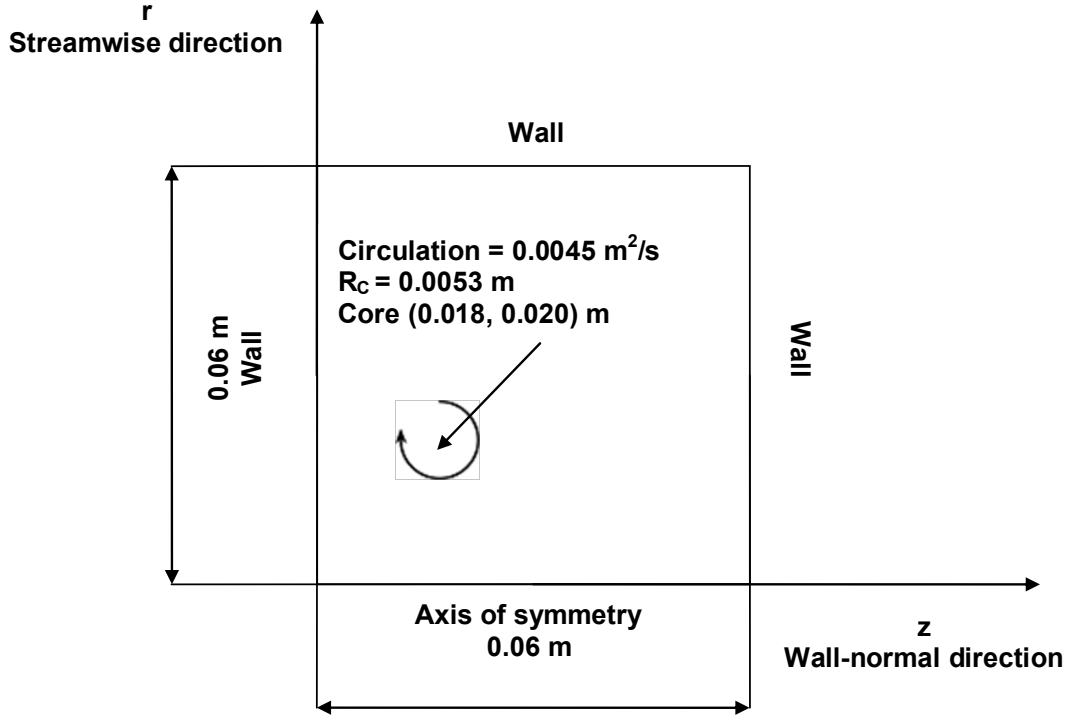


Figure 3.5: Geometry of the computational model to be used in ANSYS[®]-Fluent based on experimental geometry given in Figure 3.2 [3]

where,

ω_θ : Out-of-plane (azimuthal) vorticity at a particular location in the flow domain.

ω_0 : This is the initial peak vorticity (at the vortex core center) of the primary vortex ring when introduced in the flow-domain (at $t = 1.4$ s, in experiments).

R_c : Initial core radius of the primary vortex.

r_{peak}, z_{peak} : The initial radial and wall-normal coordinate, respectively, of the vortex core center. It is also the location of the peak vorticity.

r and z : The radial and wall-normal coordinates, respectively, of locations within the flow domain.

The parameters in Equation 3.1 ($\omega_0, r_{peak}, z_{peak}$ and R_c) are determined by fitting the

vorticity distribution given by Equation 3.1 to that extracted from the experimental velocity vector field at time $t = 1.4$ s. As seen from the LIF visualization images in Figure 3.3, the selected time corresponds to an instant where the vortex ring is approaching the wall and there is very little activity within the boundary layer flow (light-colored dye) induced by the ring. Because the Gaussian model provided good, but not perfect, representation of the experimental vorticity distribution, the characteristics of the experimental distribution exhibited some variation depending on the direction along which the distribution is extracted. This can be seen more clearly in Figure 3.6 where the experimental vorticity distribution is shown along two different lines that pass through the vortex core center (i.e. where the peak vorticity is found) at $t = 1.4$ s: one line parallel to the r and the other to the z axis. As seen from the figure, though the two vorticity distributions are qualitatively similar, they have quantitative differences that will lead to different vortex parameters when fitting Equation 3.1 to each. Thus, for the purpose of the computation, three different sets of vortex parameters are employed: one based on the vorticity distribution along r (referred to as r -profile), the other based on that along z (or z -profile) and the last based on an average of the parameters extracted from the r - and z - profiles.

In order to do the Gaussian fit, we are required to know the following information from the experimental data: $\omega(r)$ and $\omega(z)$ through the vortex core center, and location of the core center (r_{peak}, z_{peak}) . The former is known from the vorticity values at different locations in the flow-field from the MTV data set [3]. Additionally, Gendrich *et al.* [3] give the approximate location of the center of the vortex ring at $t = 1.4$ s. For fitting the r -profile (similar procedure is followed for the z -profile equation (3.1) can be rewritten as)-

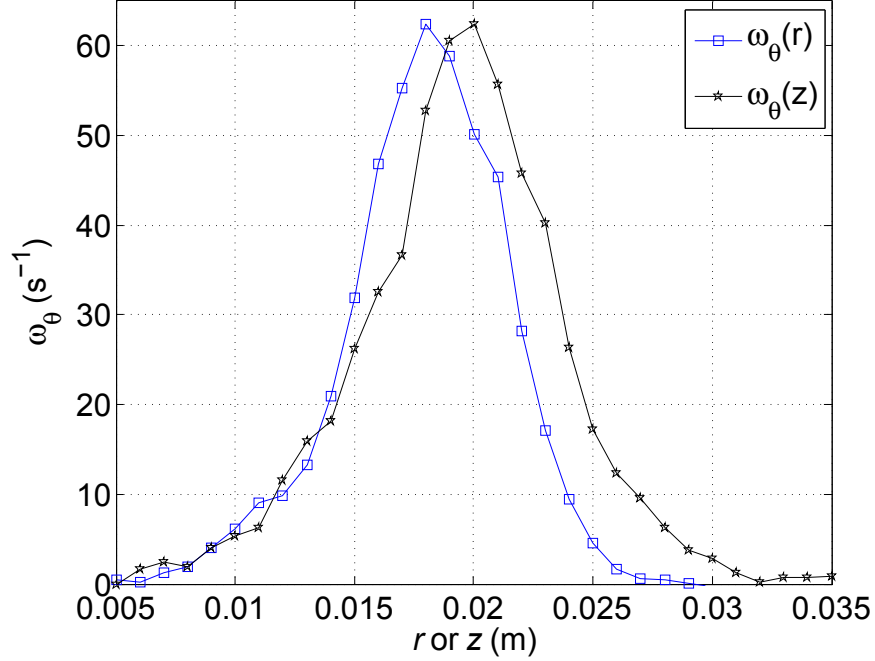


Figure 3.6: Experimental vorticity at $t = 1.4$ s along lines passing through the vortex core center while parallel to r and z axis

$$\omega_{\theta} = \omega_0 e^{-\left(\frac{r-r_{peak}}{R_c}\right)^2} \quad (3.2)$$

With r_{peak} known from the experiments, this equation is fitted to determine the values of ω_0 and R_c . A second alternative fitting approach is also used in the present study. Since the location of the center of the vortex ring is approximated to the nearest data grid point in paper [3], better accuracy may be gained by choosing to make the initial position (r_{peak} , z_{peak}) a parameter of the fit. These two different ways of doing the Gaussian fit will be referred to as: *two-parameter fit* and *three-parameter Fit*

3.3.1.1 Two-Parameter Fit

The initial core center position, $(r_{peak}, z_{peak}) = (0.018, 0.02) m$, is known from the MTV data [3][8]. A linear fit can be done after taking natural-log of both sides of Equation (3.2)-

$$\ln(\omega_\theta) = \ln(\omega_0) - \frac{1}{(R_c)^2}(r - r_{peak})^2 \quad (3.3)$$

This expression is of the form $y = mx + c$, with $x = (r - r_{peak})^2$ and $y = \ln(\omega_\theta)$. From the linear fit (refer to Figures 3.7 and 3.8), we can determine the-

The y -intercept, $c = \ln(\omega_0)$ which gives the initial vorticity (ω_0), and the slope $m = \frac{-1}{R_c^2}$ which gives the initial vortex core radius (R_c). It is seen in the Figures 3.7 and 3.8 that the experimental data points fall above and below the fit, with some scatter, in an asymmetric manner. One of the two data branches represent data at $r > R_c$ and the other at $r < R_c$. For a perfect Gaussian behavior, the two branches should yield identical vorticity values (i.e. they should collapse on one another). The discrepancy seen in Figures 3.7 and 3.8 is believed to be due to inaccurate initial core center as well as deviation from true Gaussian behavior.

3.3.1.2 Three-Parameter Fit

Here, the vortex core center location (r_{peak}, z_{peak}) is one of the fit parameters. Taking natural-log of both sides of the Equation 3.2 -

$$\ln(\omega_\theta) = \frac{-1}{R_c^2}r^2 + \left(\frac{2r_{peak}}{R_c^2}\right)r + \left(\ln(\omega_0) - \left(\frac{r_{peak}}{R_c}\right)^2\right) \quad (3.4)$$

This expression is of the form $y = ax^2 + bx + c$, and a quadratic polynomial fit (refer to Figures 3.9 and 3.10) will yield the constants-

$$a = \frac{-1}{R_C^2} \text{ which gives the initial vortex core radius } (R_C)$$

$$b = \frac{2r_{peak}}{R_C^2} \text{ that gives the initial location of the vortex center, and}$$

$$c = \ln(\omega_0) - \left(\frac{r_{peak}}{R_C}\right)^2 \text{ that gives the initial peak vorticity } (\omega_0).$$

Figure 3.11 shows comparison of the Gaussian fits compared to the data extracted along a line parallel to r and z axis using *two*-parameter and *three*-parameter fits. Table 3.1 summarizes the values of three parameters r_{peak} or z_{peak} , R_C , and ω_0 . The values of initial maximum vorticity (ω_0) and initial vortex core radius (R_C) are used to compute the initial circulation ($\Gamma_0 = \pi R_C^2 \omega_0$: a relation that can be derived given the Gaussian shape of the vorticity distribution).

Table 3.1: Initial Vortex parameters obtained from the Gaussian fit

Profile	Type of fit (n-Parameter)	Maximum Vorticity ω_0 (1/s)	Position of maximum vorticity r_{peak} or z_{peak} $\times 10^{-3}$ (m)	Initial core radius $R_C \times 10^{-3}$ (m)	Initial Circulation $\Gamma_0 = \pi R_C^2 \omega_0 \times 10^{-4}$ (m^2/s)
r	2	60.2509	18.000	4.4345	35.7345
z	2	56.7836	20.000	5.217	48.5570
r	3	62.2480	18.337	4.143	33.5664
z	3	58.4330	19.602	5.012	46.1137

3.3.2 Comparison of Numerical Results With Experiments

The initial condition of the computation is specified using the initial vortex parameters listed in Table 3.1. Although the parameters were obtained using *two*- and *three*- parameter fits, the latter is more accurate as it extracts the initial location of the primary vortex center with an accuracy better than the spacing of the measurement grid. Thus, for the purpose of the simulations, the initial vortex location is set to - $(r_{peak}, z_{peak}) = (0.018337, 0.019602)$ m.

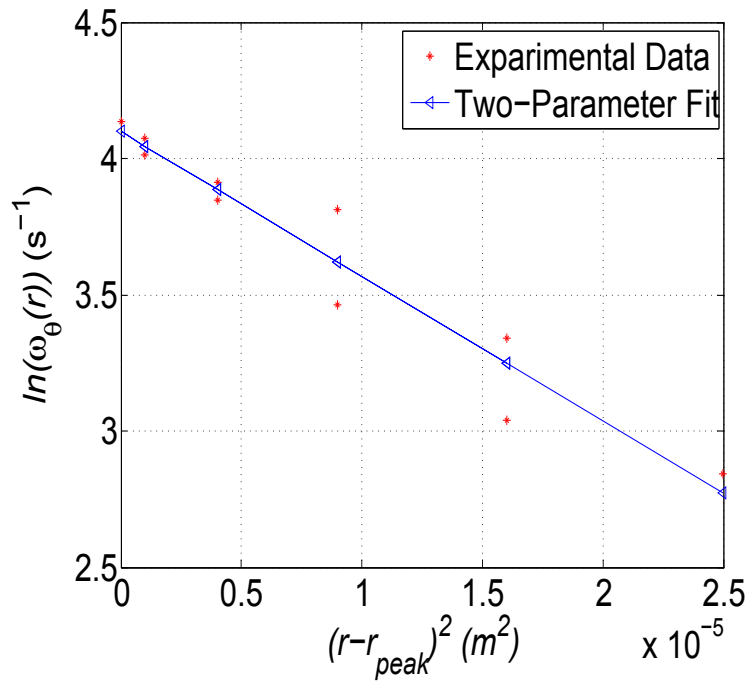


Figure 3.7: Two-parameter fit, with $r_{peak} = 0.018$ m and $z_{peak} = 0.02$ m is taken from from the experiments at $t = 1.4$ s, compared to experimental data for the r -profile

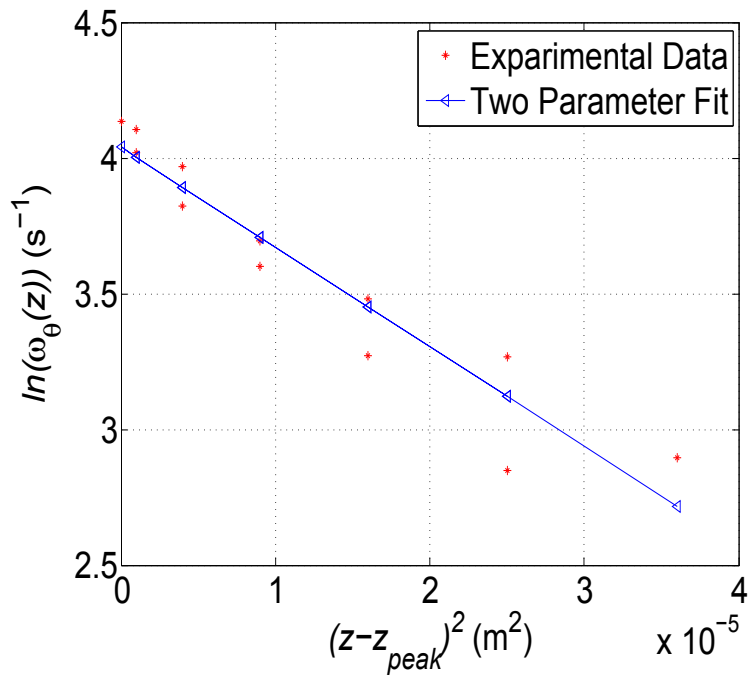


Figure 3.8: Two-parameter fit, with $r_{peak} = 0.018$ m and $z_{peak} = 0.02$ m is taken from from the experiments at $t = 1.4$ s, compared to experimental data for the z -profile

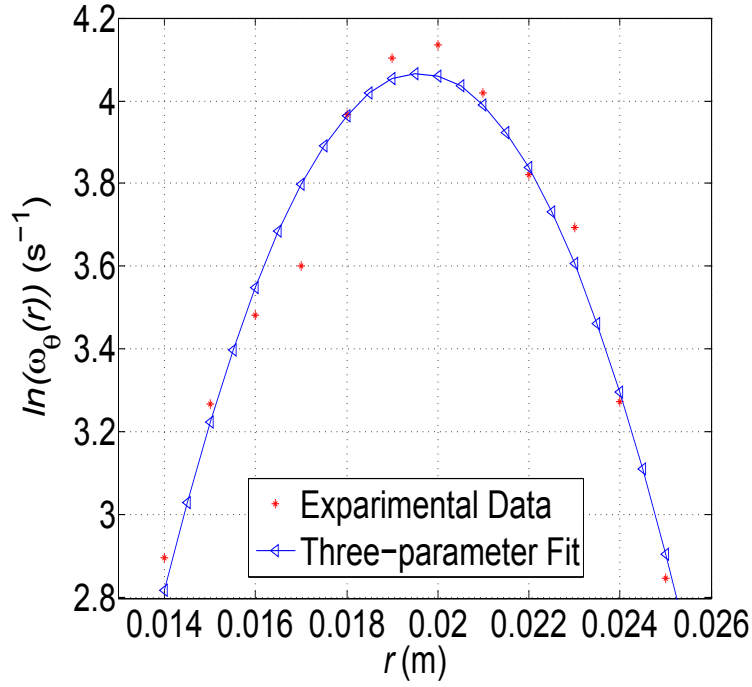


Figure 3.9: Three-parameter fit compared to experimental data for the r-profile. Initial position of the center of vortex r_{peak} and z_{peak} is obtained from the fit

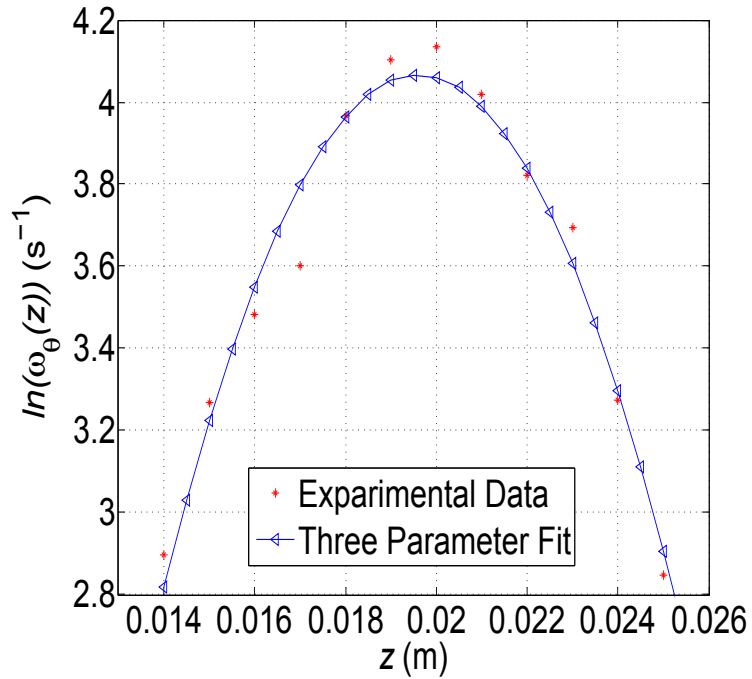


Figure 3.10: Three-parameter fit compared to experimental data for the z-profile. Initial position of the center of vortex r_{peak} and z_{peak} is obtained from the fit

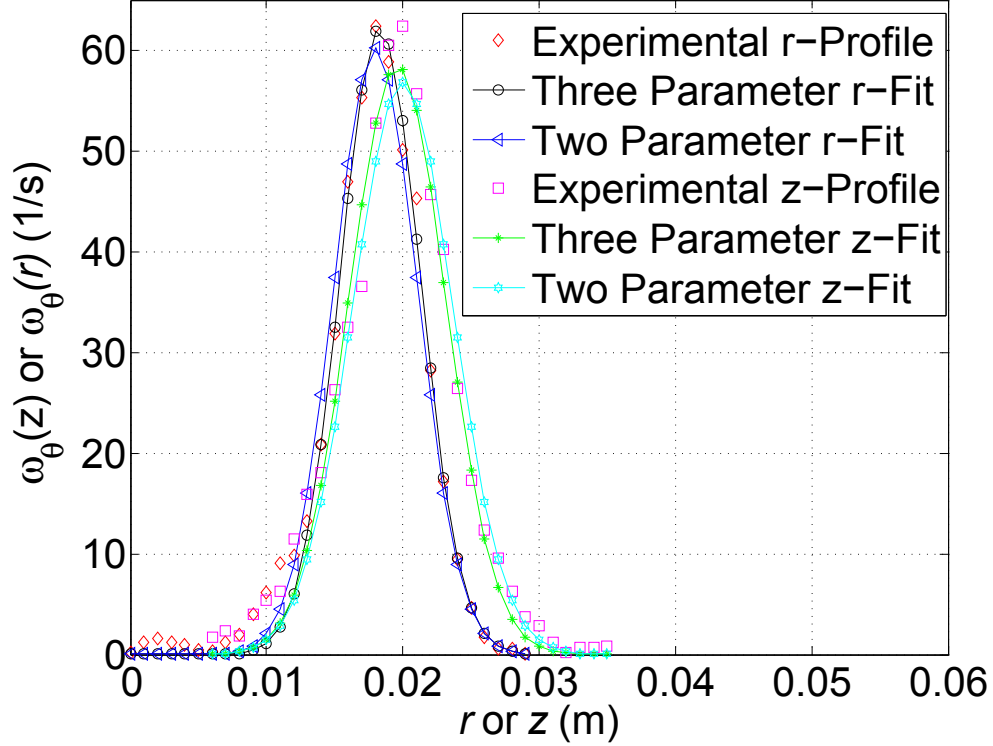


Figure 3.11: Experimental, r and z vorticity profiles compared with *two*-parameter and *three*-parameter Gaussian fits

To initialize the simulation, the velocity field induced by the Gaussian vorticity distribution must be specified. The radial and wall-normal components of the velocity field are computed from:

$$u = -\frac{\Gamma(r)}{2\pi} \frac{y}{x^2 + y^2} \quad (3.5)$$

$$v = +\frac{\Gamma(r)}{2\pi} \frac{x}{x^2 + y^2} \quad (3.6)$$

where, $\Gamma(r)$ is the circulation given by-

$$\Gamma(r) = \int_0^r \omega(r) dr \quad (3.7)$$

contained in a circle of radius, $r = \sqrt{x^2 + y^2}$

The simulation employed 0.06×0.06 m square domain having 360,000 grid points (600×600 uniform grid resolution, corresponding to a resolution of 0.1 mm in either direction: about one-fifth of the initial vortex core radius) and a time step of 0.005 s which is more than two orders of magnitude bigger than the initial vortex core radius in each direction. The fluid used was water with kinematic viscosity, $\nu = 1.004 \times 10^{-6} \text{ m}^2/\text{s}$. The choices of the spatial and the temporal resolution were confirmed to be appropriate as will be discussed in the following sections. The boundary condition was set to the no-slip condition on three of the four boundaries, and to symmetry axis on the fourth boundary. This agrees with the experiment except for the boundary opposite to the impingement wall, which is a free surface in the experiment. However in both the experiment and computation, the boundaries of the domain are made sufficiently far away such that the boundary condition at the boundaries opposite to the impingement wall and axis of symmetry should not influence the evolution of the flow during the time of interest.

Figures 3.12 through 3.19 show a comparison of the experimental and computational vorticity contour plots for different time instants during the flow evolution. It is interesting to find that the vorticity contours of the simulated model match closely with their experimental counterpart at the same time instant. This matching is particularly true for the evolution of the primary vortex. The secondary vortex development also agrees closely, but not exactly. Specifically, the development of the secondary vortex captured in the simulation seems to lag by a small amount relative to the one seen in the experiments. This is likely because the initial condition in the simulation matches the vorticity distribution associated with the primary vortex while ignoring the boundary layer on the impingement wall (i.e. no boundary layer exists at $t = 0$ in the simulation). As a result, it is probably not surprising

for the boundary layer development in the computation to lag behind the experiments. This would cause a lag in the development of the secondary vortex as well, which forms from the boundary layer. It is also worth noting that the boundary-layer vorticity level in the simulation is larger than that seen in the experiment; e.g. compare Figures 3.14 and 3.15. This is believed to be caused by the much finer resolution of the computation, yielding vorticity values much closer to the wall than in the experiment.

The above discussion demonstrates the consistency of the flow physics extracted from the computation in comparison to the experiments. To give a more quantitative measure of the accuracy of the computation, the evolution of the peak vorticity at the center of the primary vortex is obtained from the three computational cases and compared to the experimental counterpart in Figure 3.20. Note that since the initial peak vorticity for the computation is obtained from the three-parameter curve fitting rather than taken directly from the experimental data, the plot in Figure 3.20 gives the vorticity at any time instant relative to the initial vorticity. Inspection of Figure 3.20 shows that out of the three computational cases, case 2 (with the initial condition based on the three-parameter fit to the z -profile of vorticity) agrees the best with the experimental results. This may not be too surprising since Re_{Γ_0} (see Table 3.2) value computed from the vortex parameters is extracted from the z -profile curve fit which is the closest to that extracted from the experiments. Additional quantitative measures that gives confidence in the computation may be obtained by comparing the *axial*- and the *radial*- trajectory of the center of the primary vortex core from the Fluent computation and the experiments (Figure 3.21). The comparison is shown in Figure 3.21. Note that the initial coordinates of the vortex core (i.e. at zero time) do not agree exactly with their counterpart from the experiment. This is because the latter are located based

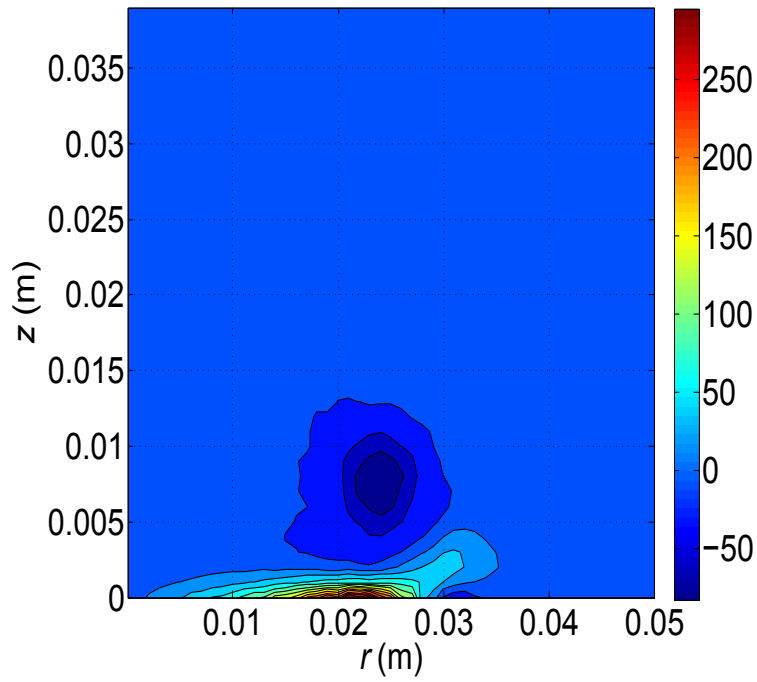


Figure 3.12: Vorticity (ω_θ) contour of the *experimental* flow-field at $t = 0.3$ s (measured relative to the time of occurrence of the velocity field used to set the initial Gaussian vortex parameters for the computation: $t = 1.4$ s relative to the solenoid opening)

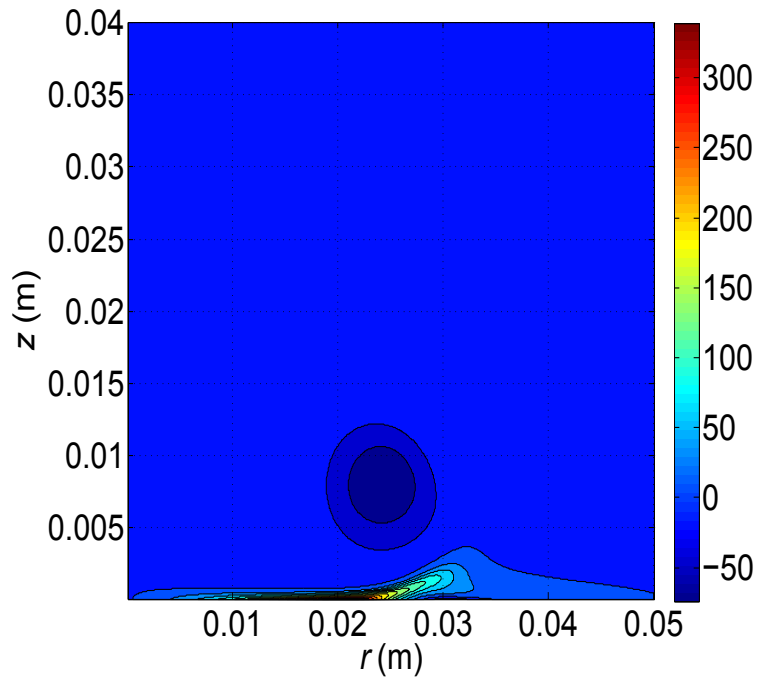


Figure 3.13: Vorticity (ω_θ) contour of the *simulated* flow-field at $t = 0.3$ s

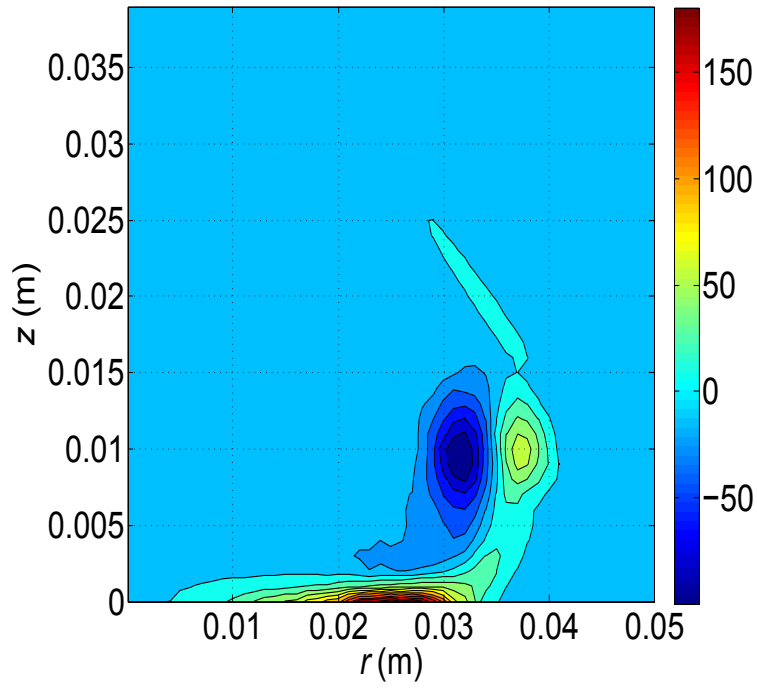


Figure 3.14: Vorticity (ω_ρ) contour of the *experimental* flow-field at $t = 0.5$ s (measured relative to the time of occurrence of the velocity field used to set the initial Gaussian vortex parameters for the computation: $t = 1.4$ s relative to the solenoid opening)

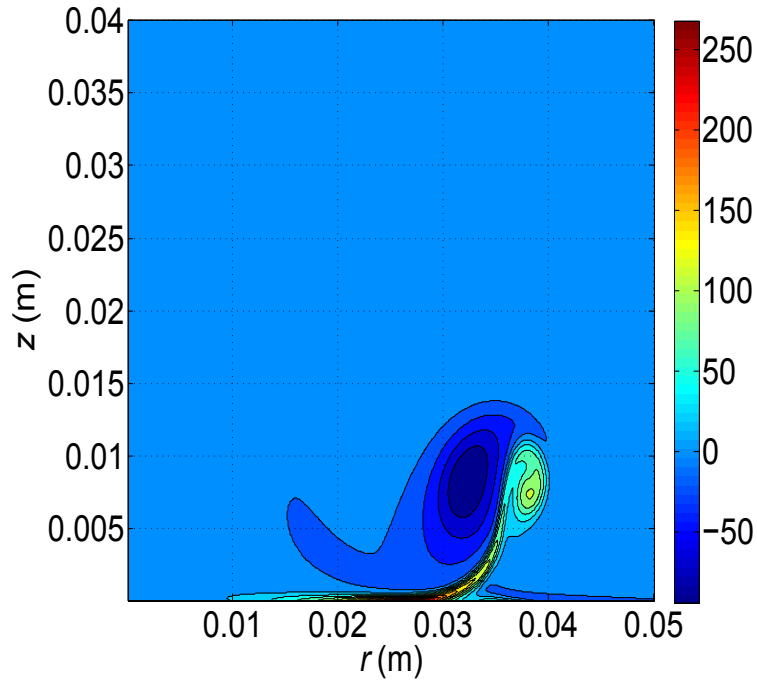


Figure 3.15: Vorticity (ω_ρ) contour of the *simulated* flow-field at $t = 0.5$ s

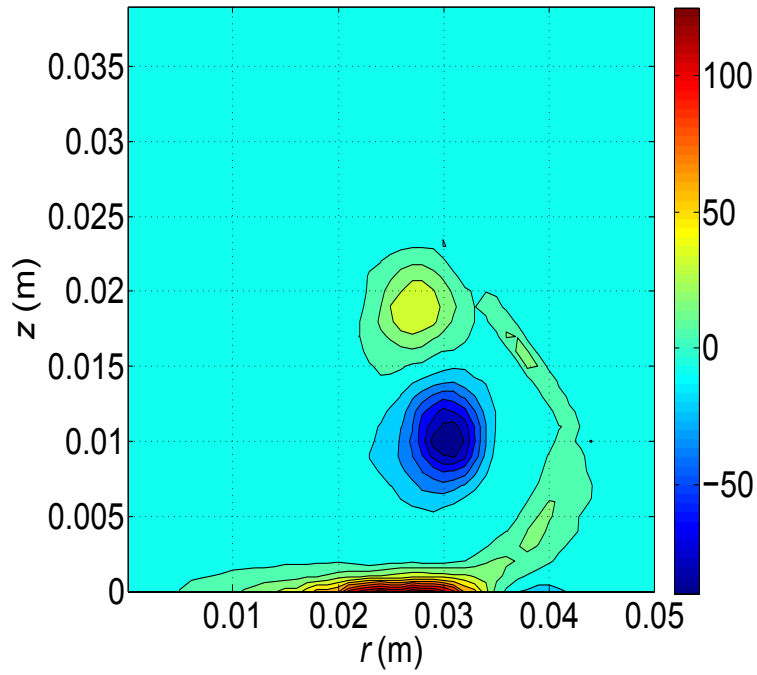


Figure 3.16: Vorticity (ω_θ) contour of the *experimental* flow-field at $t = 0.8$ s (measured relative to the time of occurrence of the velocity field used to set the initial Gaussian vortex parameters for the computation: $t = 1.4$ s relative to the solenoid opening)

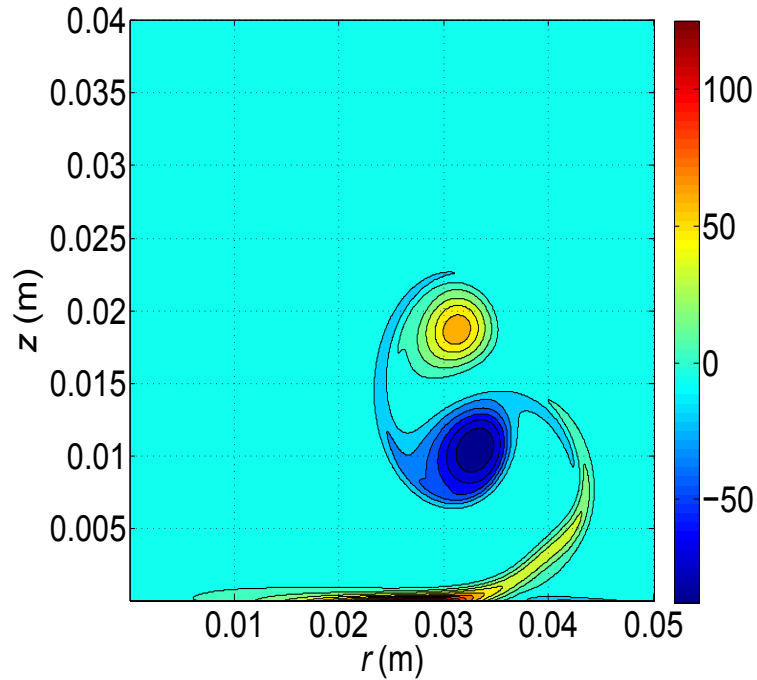


Figure 3.17: Vorticity (ω_θ) contour of the *simulated* flow-field at $t = 0.8$ s

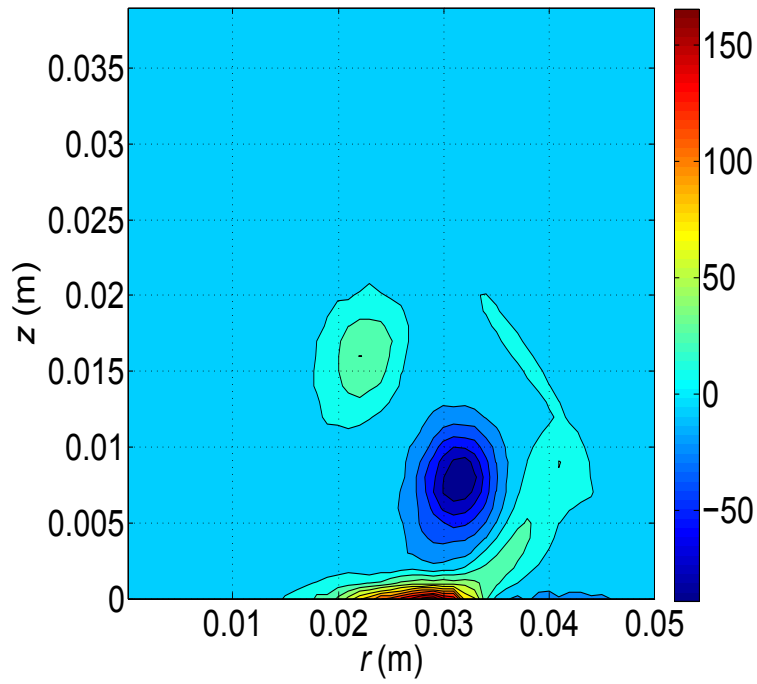


Figure 3.18: Vorticity (ω_θ) contour of the *experimental* flow-field at $t = 1$ s (measured relative to the time of occurrence of the velocity field used to set the initial Gaussian vortex parameters for the computation: $t = 1.4$ s relative to the solenoid opening)

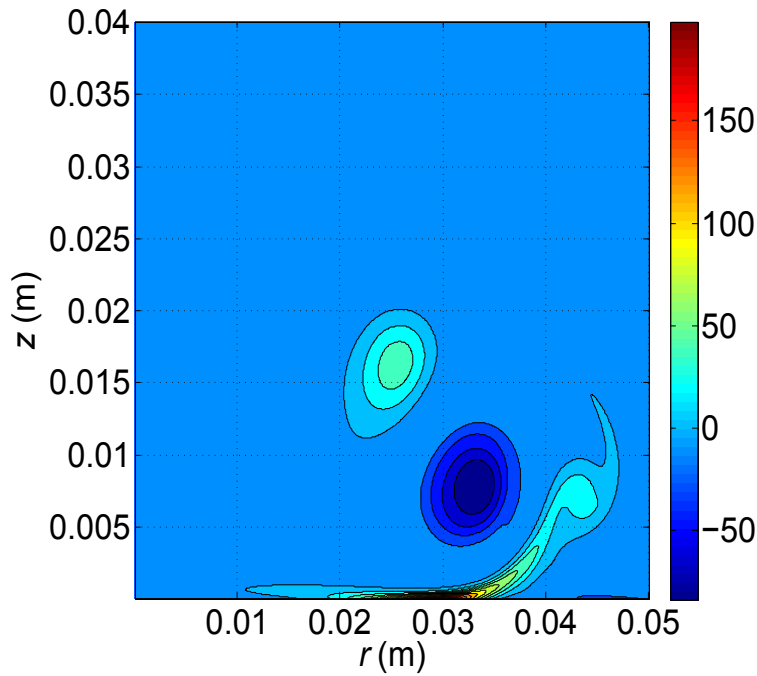


Figure 3.19: Vorticity (ω_θ) contour of the *simulated* flow-field at $t = 1$ s

on the location of peak vorticity at $t = 0$: a location that coincides with an experimental data grid point. In comparison, as described earlier, the computational results are based on curve-fitting of a Gaussian vortex model to the experimental data, which yields a center location which may fall in-between the experimental data grid points.

Table 3.2: Computational cases and associated initial vortex parameters. Listed experimental values are those given by Gendrich *et al.* [3]

Case	Profile	Initial core radius $R_c \times 10^{-3}$ (m)	Circulation $\Gamma_0 \times 10^{-4}$ (m^2/s)	Reynolds No based on initial circulation $Re_{\Gamma_0} = \frac{\Gamma_0}{\nu}$
1	r	4.143	33.566	3347
2	z	5.012	46.114	4593
3	$avg(r,z)$	4.578	39.840	3968
4	Experimental	5.300	45.000	4500

3.3.2.1 Effect of computational time step

To physically justify the choice of the time step of 0.005 s, we consider the two different time scales associated with the vortex-wall interaction: a diffusive time scale ($\tau_{Diffusive}$), associated with the diffusion of viscous effects from the wall and a convective time scale ($\tau_{Convective}$), associated with the advection of the vortex ring. If we compare the diffusive time and the convective time, we find that the convective time scale is much smaller, and therefore, it sets the more stringent constraint on the computational time step. This can be explained as follows -

$$\tau_{Convective} = \frac{D_o^2}{\Gamma_0} = \frac{4R_c^2}{\Gamma_0} \quad (3.8)$$

$$\tau_{Diffusive} = \frac{D_o^2}{\nu} = \frac{4R_c^2}{\nu} \quad (3.9)$$

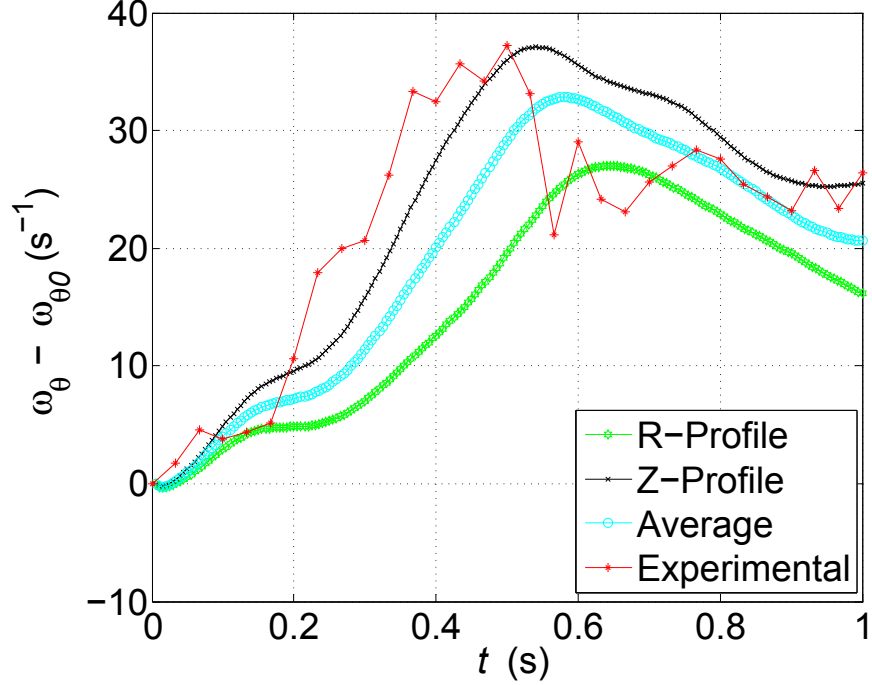


Figure 3.20: Comparison of the temporal evolution of the vorticity at the center of the primary vortex. Results from simulations based on *three*-parameter r,z and $avg(r,z)$ Gaussian profiles are compared with those from MTV experiments.

From equations 3.8 and 3.9 -

$$\frac{\tau_{Convective}}{\tau_{Diffusive}} = \frac{\nu}{\Gamma_0} = \frac{1}{Re_{\Gamma_0}} \quad (3.10)$$

Since-

$$Re_{\Gamma_0} \gg 1 \quad (3.11)$$

then-

$$\tau_{Convective} \ll \tau_{Diffusive} \quad (3.12)$$

The expression in Equation 3.12 implies that the computational time step must be sufficiently small in comparison to the convective time scale. Our choice of 0.005 s is about four

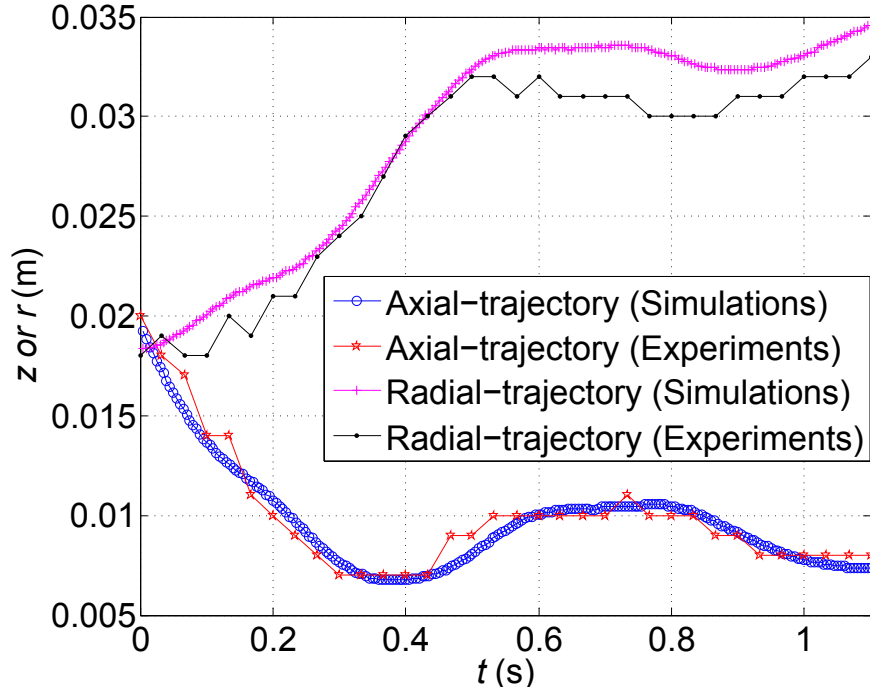
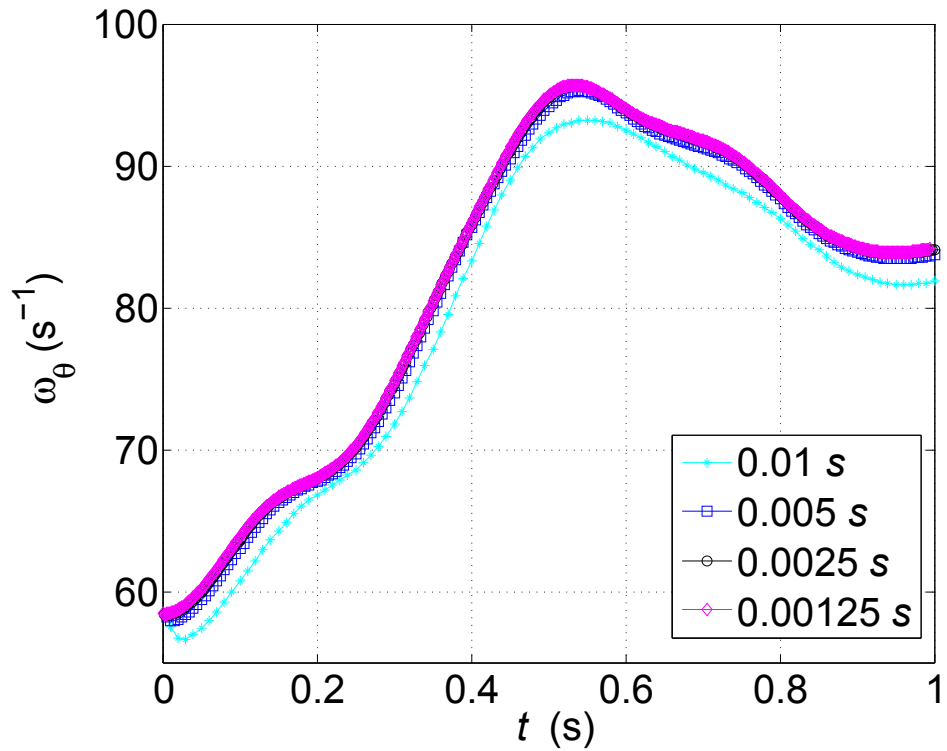


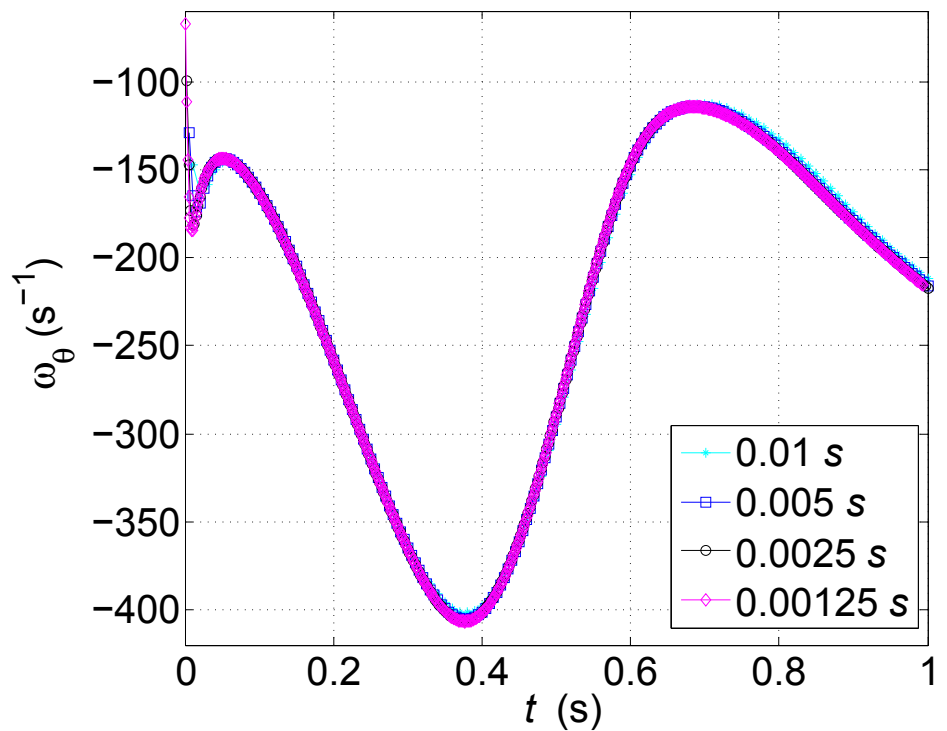
Figure 3.21: Axial- (z), and radial- (r) trajectories of the center of the primary vortex.

times smaller than the convective time scale (0.0217 s). To ascertain that this is sufficiently small, three other computations similar to that reported above except for the time step size were undertaken. The evolution of the vorticity at the primary vortex center as well as of the boundary layer for all four cases is depicted in Figure 3.22a and 3.22b respectively. Note that the boundary layer vorticity is determined by the slope of the streamwise velocity at the wall ($\omega_{BoundaryLayer} = \left. \frac{\partial u}{\partial z} \right|_{z=0}$).

From Figures 3.22a and 3.22b, we see that the vorticity profiles converge for all time steps smaller or equal to 0.005 s. It is also observed that time steps greater than 0.005 s underestimate the magnitude of the vorticity of the primary vortex and boundary layer vorticity. Based on this observation, the computation time step was set to 0.005 s.



(a) Vorticity of Primary Vortex



(b) Boundary Layer Vorticity

Figure 3.22: Effect of the computational time step on maximum vorticity of the primary-vortex (a) and boundary layer (b) vorticity. ($\Gamma_0 = 46.11 \times 10^{-4} \text{ m}^2/\text{s}$, $R_c = 0.005012 \text{ m}$, 300 iterations/time step, 600×600 grid)

3.3.2.2 Effect of number of iterations per time step

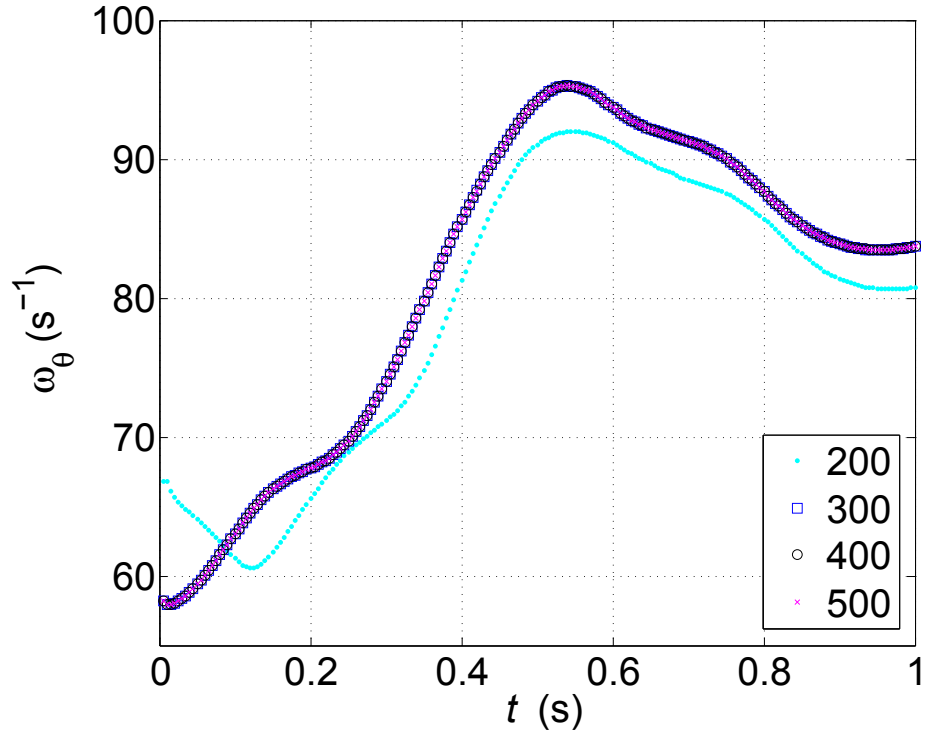
Number of iterations per time step is one of the important parameters affecting the accuracy of the computed velocities in Fluent. The utilization of an integral global-error criterion to determine convergence of the solution at each time step did not yield accurate results. We believe this stemmed from the fact that the computational domain is much larger than the vortex size, and hence the velocity at most nodes was close to zero. To remedy this problem, we systematically varied the number of iterations to see its effect on the accuracy of the computed vorticity (primary vortex and boundary layer vorticity) for the time step of 0.005 s. The number of iterations was set to 200, 300, 400 and 500 per time step to verify the convergence. The results are shown in Figures 3.23*a* and 3.23*b*.

It is evident from Figures 3.23*a* and 3.23*b* that 200 iterations underestimate vorticities but larger number of iterations, 300 through 500, produce converging profiles. Thus, 300 iterations per time step is selected in the final computation. Larger number of iterations does not give more accuracy and would increase the computational time considerably.

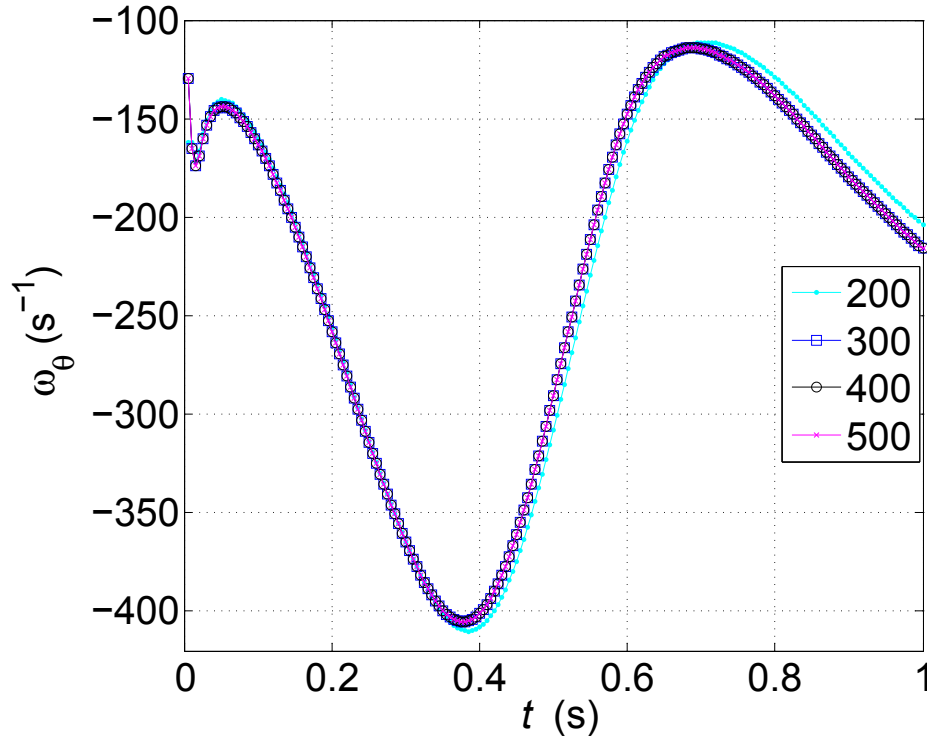
3.3.2.3 Effect of grid size

Spatial resolution is important for accurate computation. The MSU research license provided by Fluent allow a maximum of 715×715 grid points. Hence, we decided to analyze the accuracy of the computations for four grid sizes, viz. -

1. 300×300
2. 500×500
3. 600×600
4. 715×715



(a) Vorticity of Primary Vortex



(b) Boundary Layer Vorticity

Figure 3.23: Effect of no iterations per time step on maximum vorticity of the primary-vortex (a) and boundary layer (b) vorticity. ($\Gamma_0 = 46.11 \times 10^{-4} \text{ m}^2/\text{s}$, $R_c = 0.005012 \text{ m}$, Time step = 0.005s, 600×600 grid)

The resulting evolution of primary-vortex and boundary-layer vorticity for all four cases can be observed in Figures 3.24a and 3.24b respectively. The figure demonstrates that a grid size of 500×500 or bigger would resolve the primary vortex evolution properly. On the other hand, the boundary-layer vorticity does not completely converge with an approximately 5% difference seen between computation employing the largest two grid sizes. Of course, it is possible that convergence is achieved with the 715×715 grid, but this can't be ascertained without using an even larger grid. Since it is not possible to increase the number of grid points (given the Fluent license limitation), the reader is advised that computations based on the finest possible grid are uncertain to within 5%. Additionally, to gauge the influence of this error on the Taylor-series-based estimation, we will carry out flow estimations using the Taylor-series model for data obtained from the three different grid sizes.

3.4 Summary of Fluent Parameters

3.4.0.4 General Attributes:

Solver: Fluent (12.1 version), 2D- Planar, Laminar without gravity effect

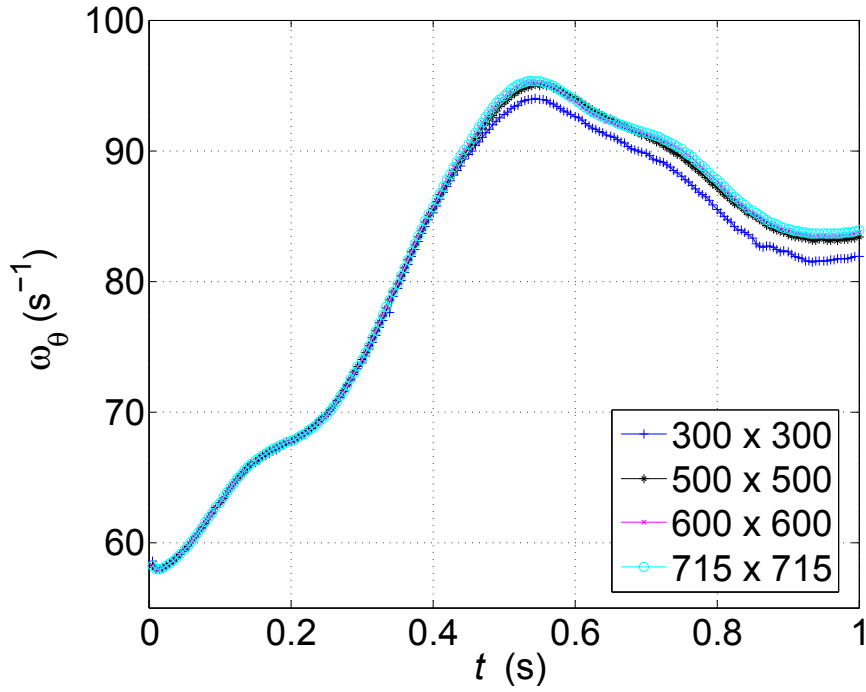
Solver Type: Pressure-Based

Velocity Formulation: Absolute

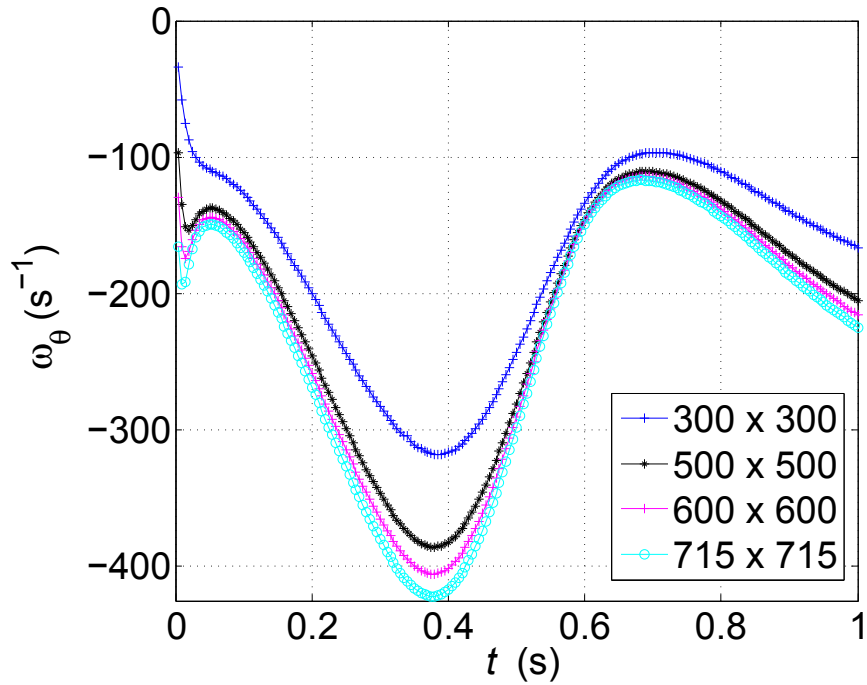
Time: Transient

Model used: Viscous - Laminar

Material: Water (Liquid) [Density (ρ): 998.2 kg/m^3 , Dynamic Viscosity (μ): $0.001003 \text{ kg/m} - \text{s}$]



(a) Vorticity of Primary Vortex



(b) Boundary Layer Vorticity

Figure 3.24: Effect of different grid resolution on maximum vorticity of the primary-vortex (a) and boundary layer (b) vorticity. ($\Gamma_0 = 46.11 \times 10^{-4} \text{ m}^2/\text{s}$, $R_c = 0.005012 \text{ m}$, 300 iterations/time step, Time step = 0.005 s)

3.4.0.5 Solution Methods:

Pressure-Velocity Coupling:

Scheme: PISO (Pressure Implicit solution by Split Operator method)

Skewness Correction: 0

Neighbor Correction: 1

Skewness-Neighbor Coupling: No

Spatial Discretization:

Gradient: Least Squares Cell Based

Pressure: Standard

Momentum: Third-Order MUSCL

Transient Formulation:

Second-Order Implicit with *no* non-iterative Time Advancement and *no* Forzen Flux formulation.

3.4.0.6 Solution Controls:

Under-Relaxation Factors:

Pressure: 0.3

Density: 1

Body Forces: 1

Momentum: 0.7

Chapter 4

Simulation of A Pair of Line Vortices Impinging On A Solid Wall And Estimation of Velocities Using The Cartesian Taylor Series Model

In Chapter 3, we discussed how an axisymmetric vortex ring impinging on a wall can be simulated accurately in ANSYS[®]-Fluent. The parameters used to simulate the vortex ring problem are now used to simulate a pair of linear vortices impinging on a wall; *i.e.* the Cartesian geometry counterpart. The numerical database will contain time-resolved velocity-field information, which will be used to calculate the wall stresses (wall-shear stress and wall-pressure gradient) that, in turn, enable us to apply the Cartesian Taylor-series model to estimate the velocity components. The estimated field is then compared to the true field to assess the viability of the model to capture the characteristics of the vortex pair

(primarily the center location and the strength of the vortex).

4.1 Geometry of the Computational Model

A pair of counter rotating vortices is introduced in a $0.06 \times 0.06 \text{ m}^2$ flow-domain (Figure 4.1). As determined in the previous chapter, based on the *three*-parameter Gaussian fit, a vortex is introduced at $(x_{peak}, y_{peak}) = (0.018337, 0.019602) \text{ m}$. The vortex has initial circulation (Γ_0) of $46.11 \times 10^{-4} \text{ m}^2/\text{s}$ with the core radius $R_c = 0.005012 \text{ m}$. Only the vortex in the first-quadrant is shown in the geometry given in Figure 4.1 since symmetry is imposed relative to the y -axis in Fluent and hence there is no need to explicitly solve for the line vortex on the other side of the y -axis. Each of the vortices in the pair induce a velocity on the other vortex causing the vortex to approach the vertical wall placed along the x -axis. Subsequently, the image (virtual) vortex in the wall (required to maintain zero wall-normal velocity at the wall) induce a velocity on the real vortex, causing it to travel in the positive x direction, hereafter, referred to as the *streamwise direction* (while the y axis will be referred to as the *wall-normal direction*). The reference point is at the top-left is where the pressure value is used as a reference in calculating the surface-pressure coefficient.

The computational grid is prepared in Gambit. Three different grids are used in order to study the effect of spatial resolution -

1. 500×500 - Called *Domain-500* - The square domain is divided into 500 equal intervals along both directions.
2. 600×600 - Called *Domain-600* - The square domain is divided into 600 equal intervals along both directions.
3. 715×715 - Called *Domain-715* - The square domain is divided into 715 equal intervals

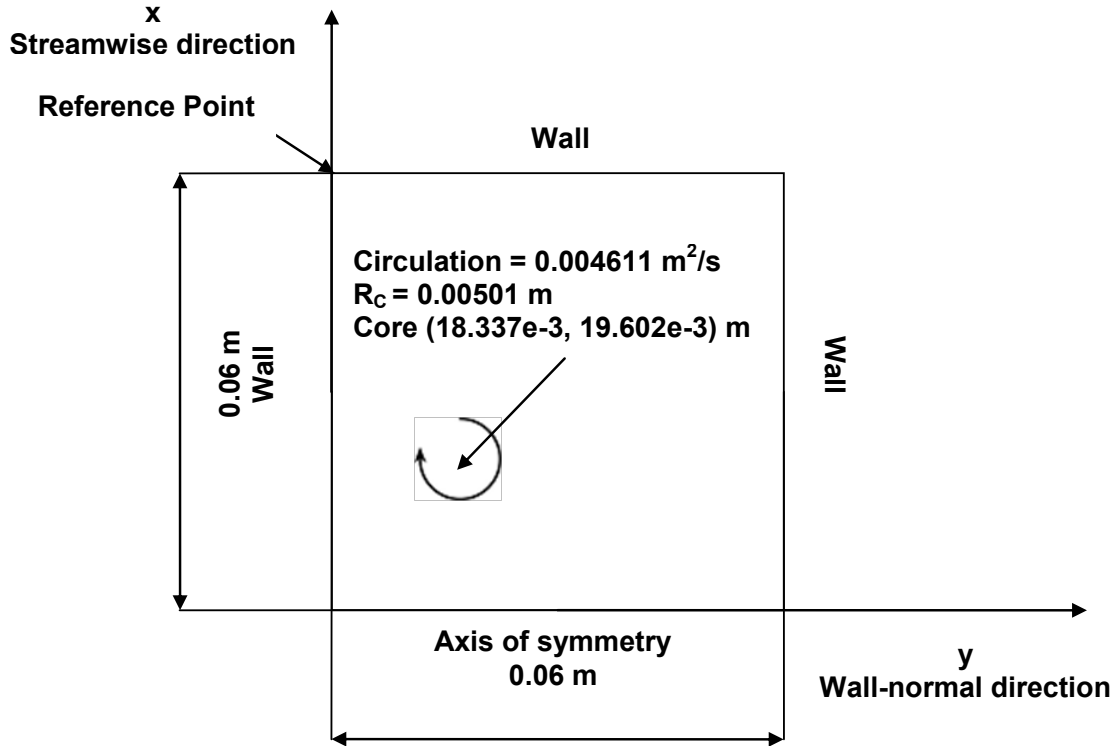


Figure 4.1: Illustration of the numerical domain and initial/boundary conditions used for simulation of a pair of counter rotating vortices having initial circulation $\Gamma_0 = 46.11 \times 10^{-4} \text{ m}^2/\text{s}$ and initial core radius $R_c = 0.005012 \text{ m}$ introduced in a $0.06 \times 0.06 \text{ m}^2$ square-domain at $(0.018337, 0.019602) \text{ m}$ at $t = 0$. Because of problem symmetry, only the upper half domain containing one of the vortices is computed.

along both directions. As noted in Chapter 3, this is the maximum allowable number of grid points under the current ANSYS[®]-Fluent license.

4.2 Simulations Using ANSYS[®]-Fluent

ANSYS[®]-Fluent solver is used to carry out the simulation described in the previous section.

The grid geometry from Gambit is imported in Fluent and the solution is initialized (with the Gaussian vortex of initial circulation, initial core radius and center of the vortex core as given in section 4.1) using a User Defined Function (UDF) in Fluent. The vortex profile

is estimated to be Gaussian and the solver is run to obtain the solution over a flow time period of 1.11 seconds. This duration is long enough for the primary vortex to approach the wall and induce the formation of a boundary layer and subsequent formation of a secondary vortex.

At each time steps (of 0.005 s) 300 iterations were carried out and the data files are saved and the computed Fluent data files are converted into text files using TecPlot-10 built-in capability of importing Fluent data files. These text files are then processed using MATLAB[®] to obtain the wall stresses. Once read in MATLAB[®] the wall-shear stress and the wall-pressure gradient and their time derivatives are computed using the central difference scheme to obtain the higher order coefficients in the Taylor-series model. The central difference formula used to compute the wall-shear stress, wall-pressure gradient, and their time derivatives is given below-

$$f'(x) = \frac{f(x+h) - f(x-h)}{2h} \quad (4.1)$$

where h is a distance between two adjacent nodes.

Before beginning to analyze the Cartesian simulations we compared time evolution of the vorticity at the core of the primary vortex against that obtained in the axisymmetric simulation. Figure 4.2 shows the comparison of the two cases. It is interesting to note how the early stages of development of the primary vortex are affected by the coordinate geometry. The primary vortex of the same initial conditions evolves in different ways in cylindrical and Cartesian system. The cylindrical - axisymmetric vortex ring - problem show initial increase in the vorticity of the primary vortex as it approaches the wall. This is caused by stretching of the vortex ring diameter, which results in proportional decrease in the core

size to conserve the ring's volume. Subsequently, conservation of angular momentum (over a time scale during which viscosity has no significant influence) results in amplification of the vorticity, as seen in Figure 4.2. This causes increase in the vorticity, hence we see the peak on a vorticity profile in Figure 4.2. This observation is consistent with results published by Fabris *et al.* [5], and Chu *et al.* [6]. In case of a Cartesian - counter rotating line pair of vortex - system, no vortex stretching is possible and the vorticity continues decrease.

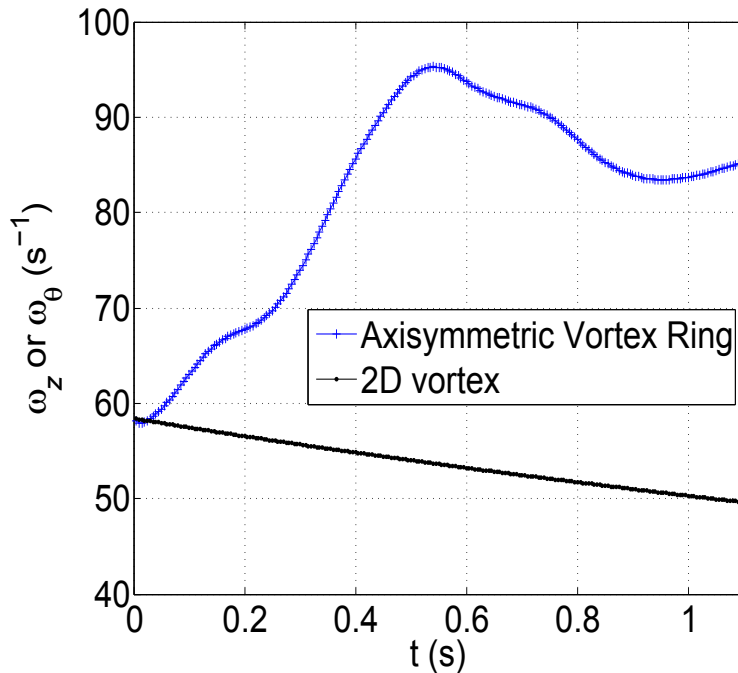


Figure 4.2: Comparison of the Vorticity at the core center of the primary vortex for an axisymmetric vortex ring (ω_θ) and 2D vortex (ω_z)

Figures 4.3, 4.4, 4.5, 4.6, 4.7, 4.8 depict how the primary vortex evolves. Figure 4.3, shows the vorticity contour at the initial time $t = 0.005$ s one time step after the primary vortex is introduced. As the computations continue beyond this time, we see the vortex moving away from the axis of symmetry and approaching the wall causing formation of the boundary layer. The boundary layer thickens and at one point separates (see Figure 4.7) and rolls up into a secondary vortex with the opposite-sign vorticity to that of the primary

vortex.

4.3 Simulation Results

The time instant $t = 0.605$ s (file number 121, see Figure 4.6) was selected for checking the viability of the Taylor series estimation model. This time instant was deemed suitable since both the primary vortex and boundary layer are prominent (a situation akin to that of the wake vortex above ground, though at a much lower Reynolds number) but without the added complexity of a well formed secondary vortex.

Figures 4.9, 4.10 and 4.11 depict the wall-shear stress, the wall-pressure and the wall-pressure gradient profiles at $t = 0.605$ s, respectively. These profiles are important as their nodal information is used to compute spatial derivatives. Figures 4.12 and 4.13 show the u - and v - velocity profiles in a plane through $x = 0.025$ m (location of the primary vortex core) and $x = 0.03$ m (outer boundary of the primary vortex). These are the velocity profiles we will be estimating using our Cartesian Taylor-series model. Readers should note that it is difficult to identify the exact vortex core location in the computational grid and it is approximated to the grid point *nearest* to the actual center of the core by finding the location of maximum vorticity within the vortex. The *almost zero* v -velocity profile in Figure 4.13 is an indication that we are near the core.

Also, in order to expand the Taylor-series model up to a high order, high-order time derivatives of the wall-shear stress and the wall-pressure gradient are required. The stencil size of the central-finite-difference scheme used to compute these derivatives increases with the increase in derivative order. Thus, more time snap shots of the flow must be available before and after the instance at which the derivatives are computed. The selected time for

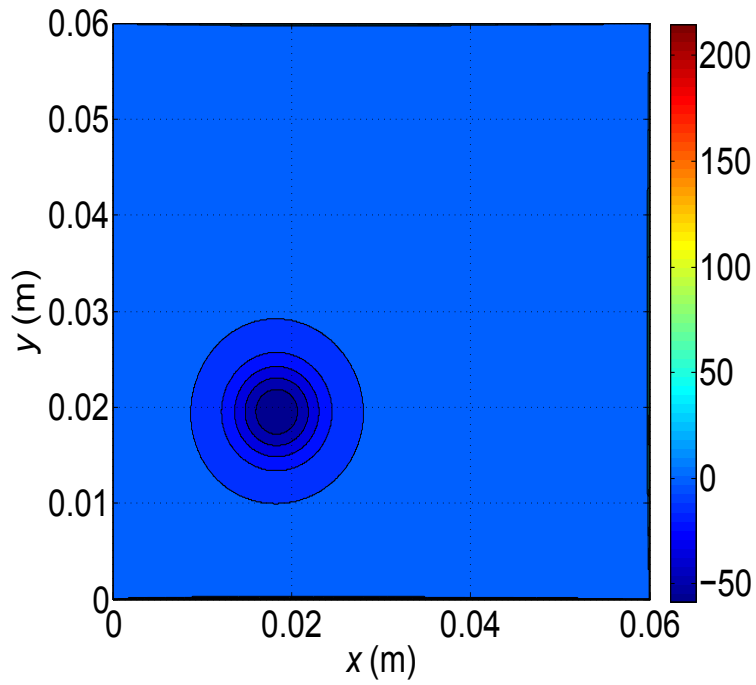


Figure 4.3: Vorticity (ω_z in s^{-1}) contour of Cartesian flow at $t = 0.005$ s showing evolution of the primary vortex.

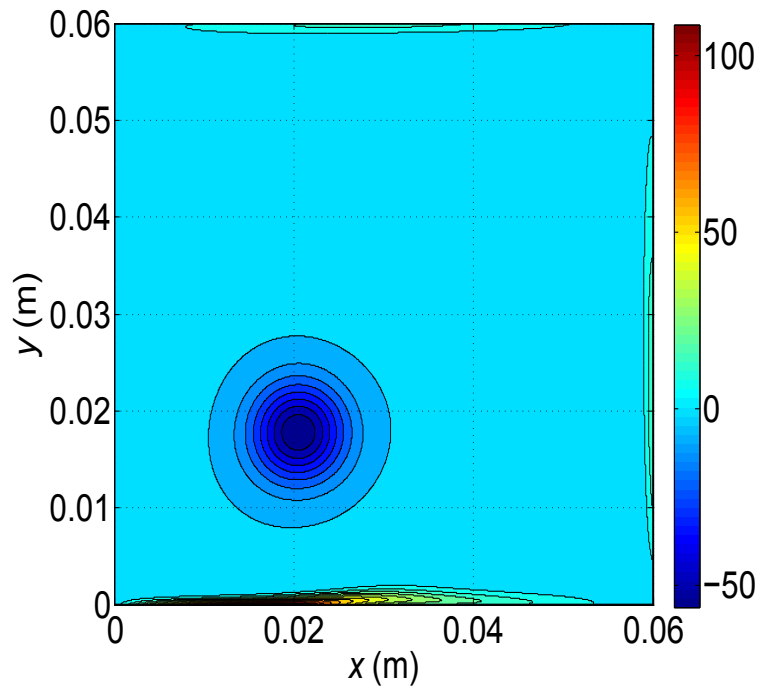


Figure 4.4: Vorticity (ω_z in s^{-1}) contour of Cartesian flow at $t = 0.25$ s showing evolution of the primary vortex.

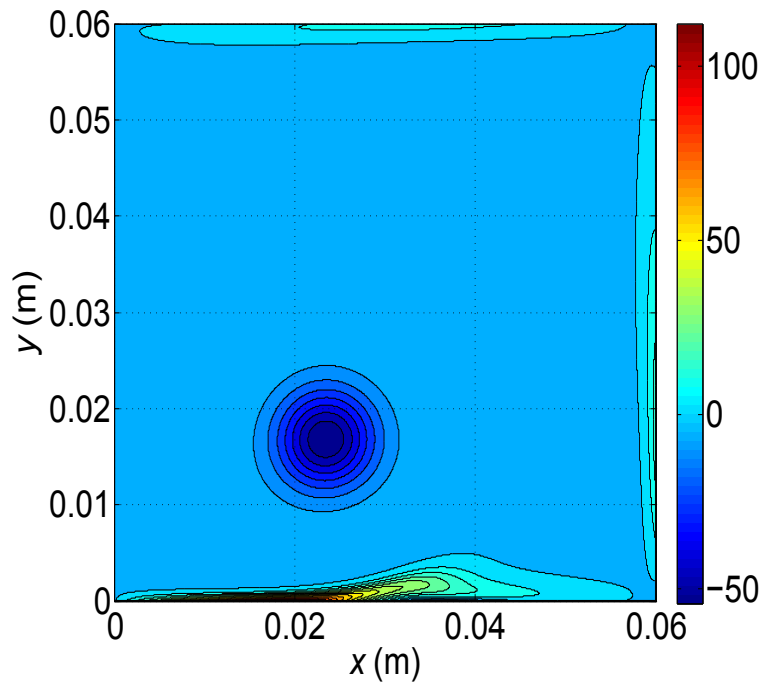


Figure 4.5: Vorticity (ω_z in s^{-1}) contour of Cartesian flow at $t = 0.50$ s showing evolution of the primary vortex.

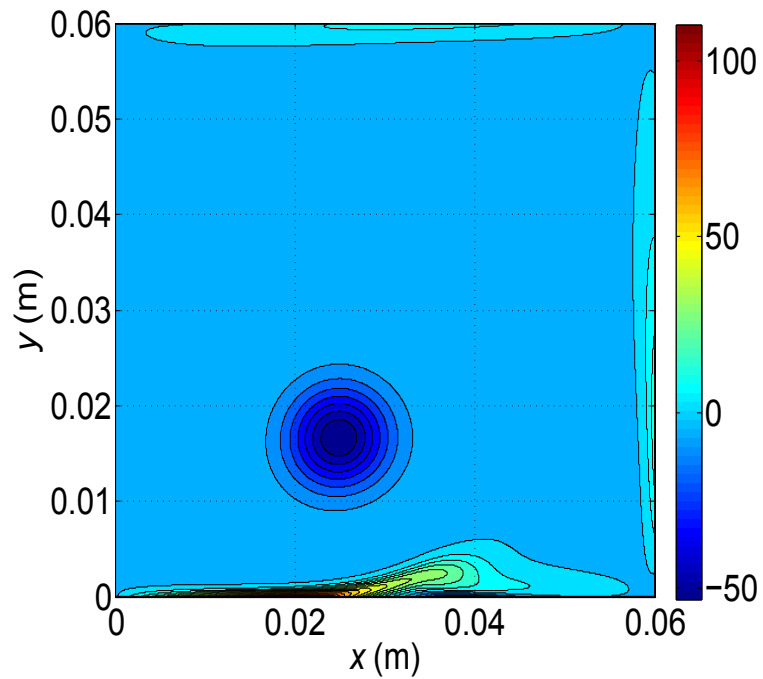


Figure 4.6: Vorticity (ω_z in s^{-1}) contour of Cartesian flow showing at $t = 0.605$ s evolution of the primary vortex.

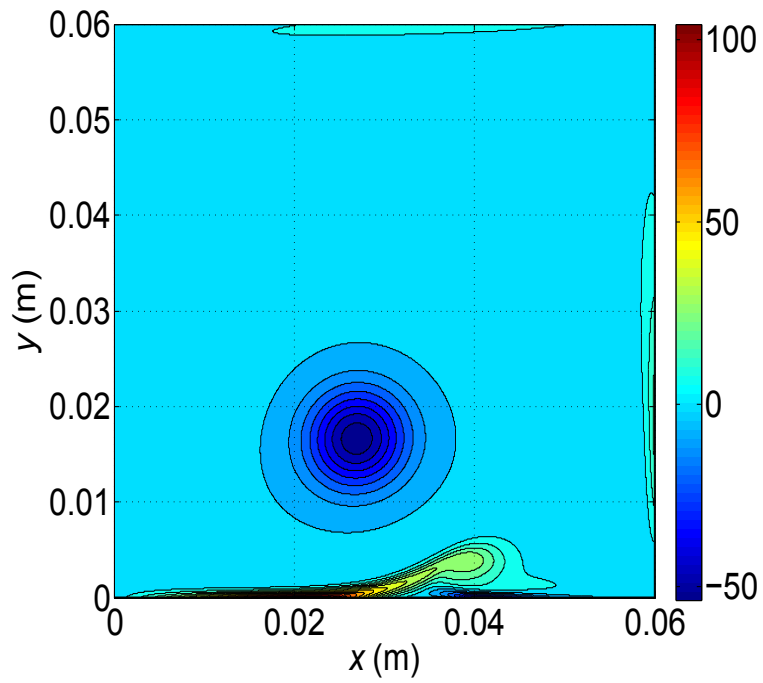


Figure 4.7: Vorticity (ω_z in s^{-1}) contour of Cartesian flow at $t = 0.75$ s showing evolution of the primary vortex.

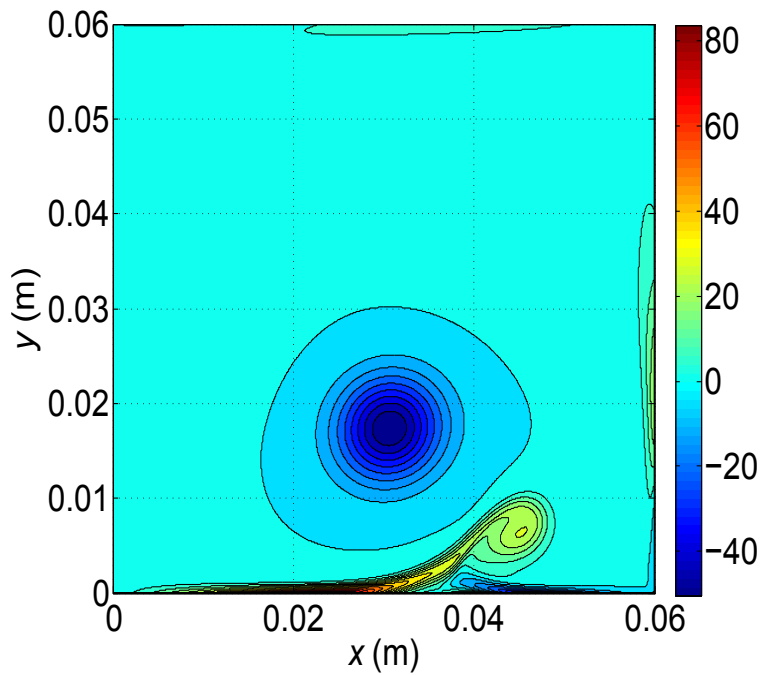


Figure 4.8: Vorticity (ω_z in s^{-1}) contour of Cartesian flow at $t = 1$ s showing evolution of the primary vortex.

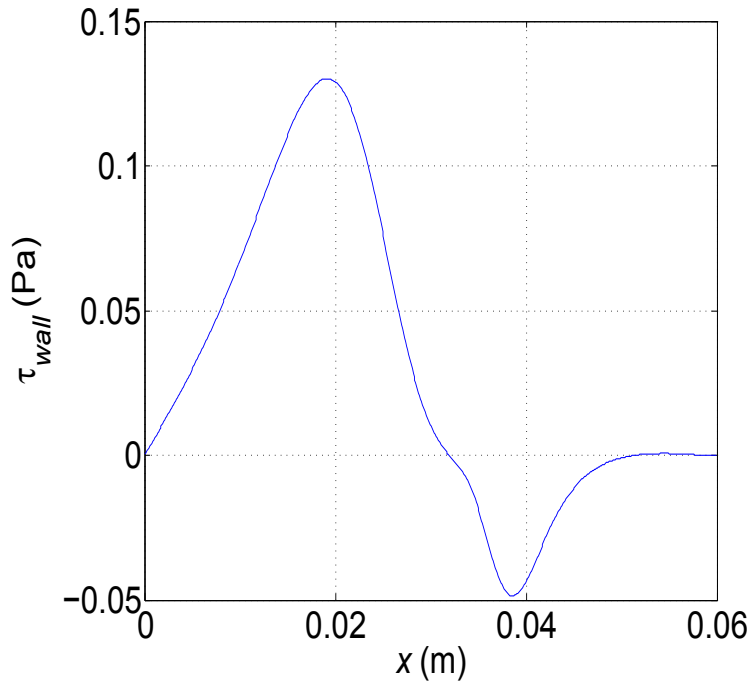


Figure 4.9: τ_{wall} profile at time $t = 0.605$ s

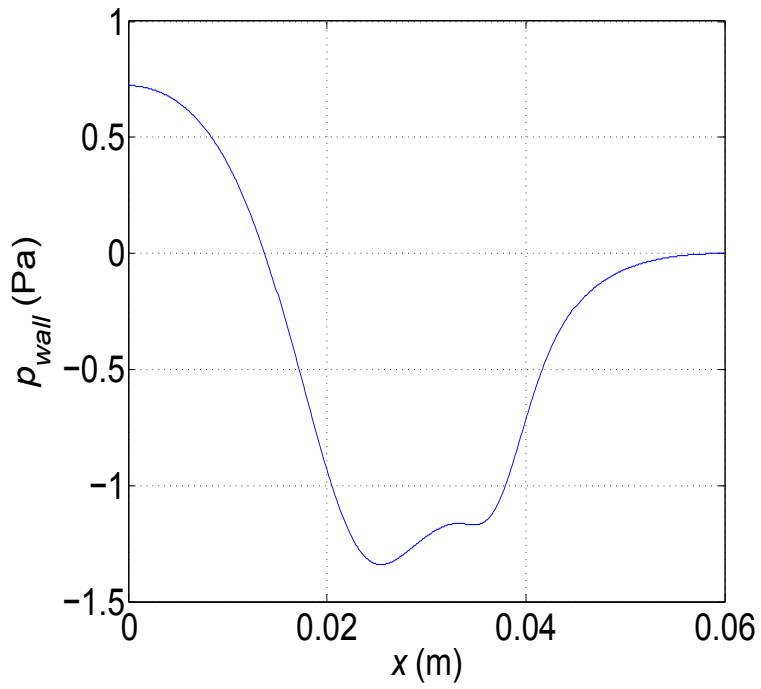


Figure 4.10: p_{wall} profile at time $t = 0.605$ s

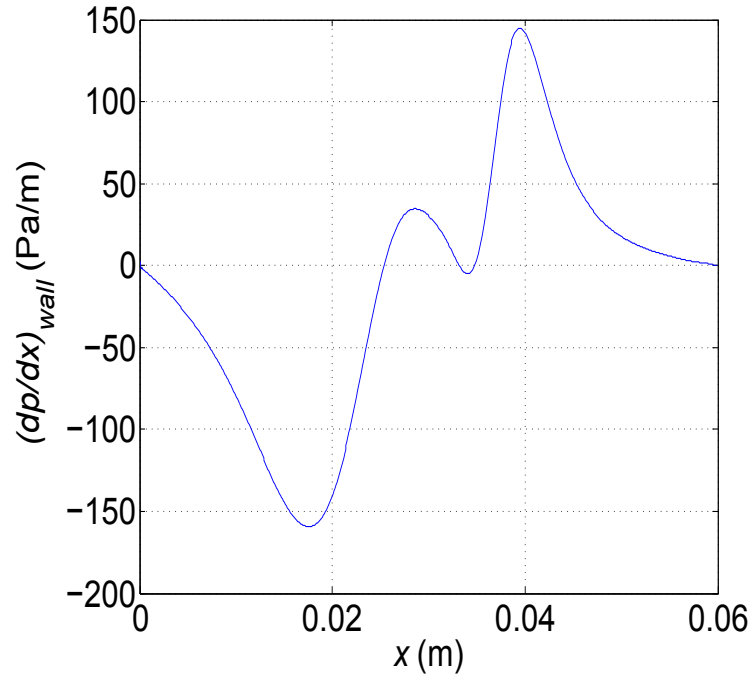


Figure 4.11: $\frac{\partial p_{wall}}{\partial x}$ profile at time $t = 0.605$ s

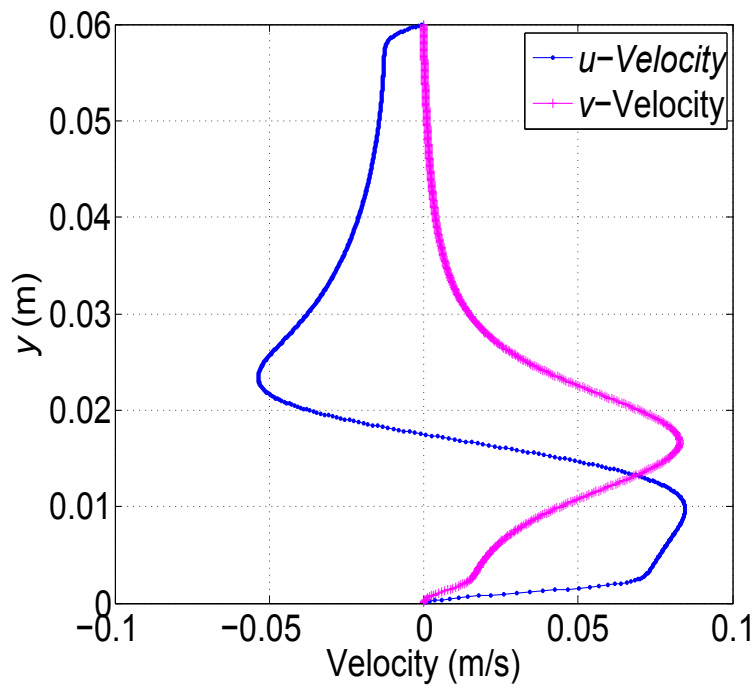


Figure 4.12: Streamwise (u -) and wall-normal (v -) profile in a plane at $x = 30$ mm (near outer edge of the primary vortex) at time $t = 0.605$ s as determined by Fluent simulations for the case of *Domain-600*

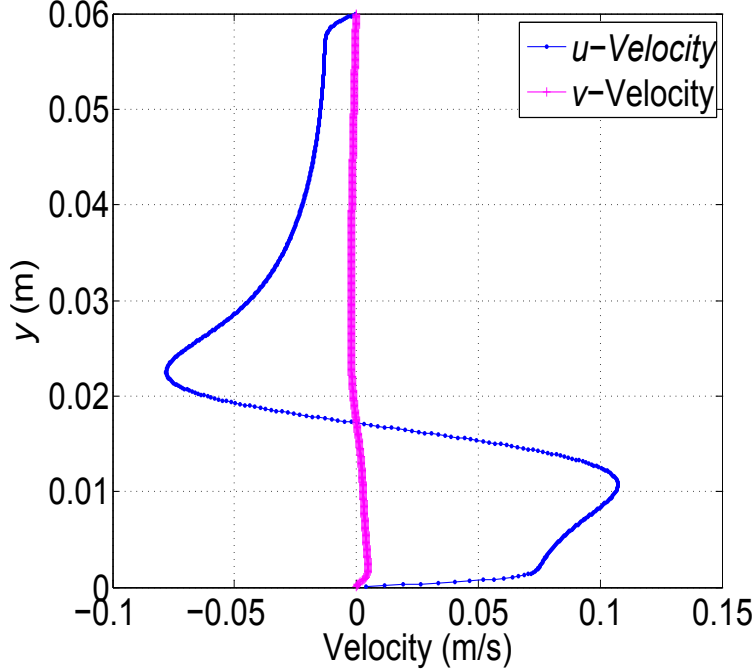


Figure 4.13: Streamwise (u -) and wall-normal (v -) profile in a plane at $x = 25$ mm (nearest pixel to the maximum vorticity, at the center of the primary vortex) at time $t = 0.605$ s as determined by Fluent simulations for the case of *Domain-600*

the estimation is roughly half-way through the computed flow duration. This makes sufficient data available before/after the time of estimation, enabling calculation of time derivatives up to 15^{th} order (and Taylor series order up to 45).

Figures 4.14 and 4.15 compare the effect of grid size on the wall-shear stress and the wall-pressure gradient. All three curves, corresponding to different grid sizes (*Domain-500*, *-600*, *-715*) converge, giving confidence that the grid size (spatial resolution) has no detectable effect on the accuracy of the computed wall-shear stress and the wall-pressure gradient. However, as we employ high order derivatives, minute differences may have significant influence on the accuracy of the derivatives at high order. Hence, we decided to estimate the velocity components for all three grid sizes and compare the convergence of Taylor-series to the actual velocity profiles (from Fluent simulations) for all three cases.

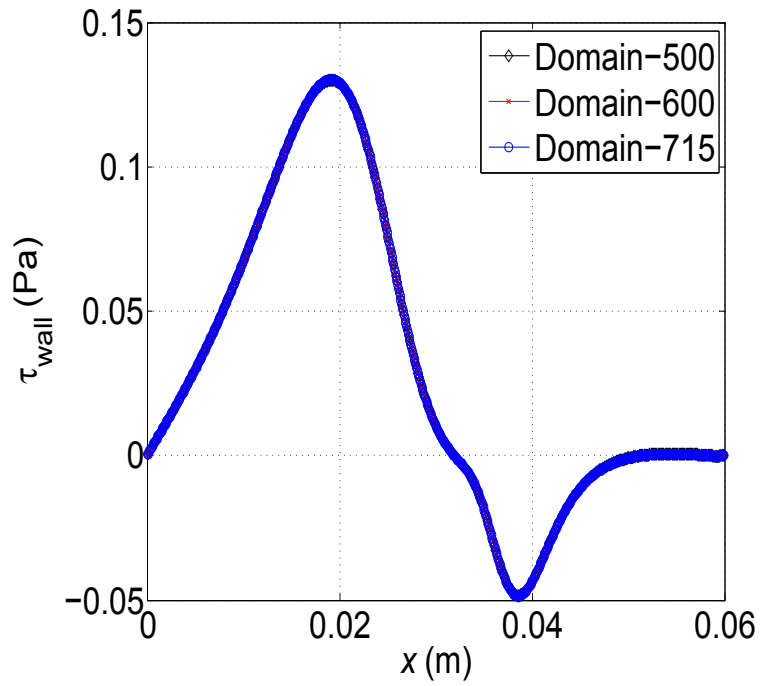


Figure 4.14: Comparison of the wall-shear stress profile along the wall, at $t = 0.605$ s for *Domain-500, -600, -715*

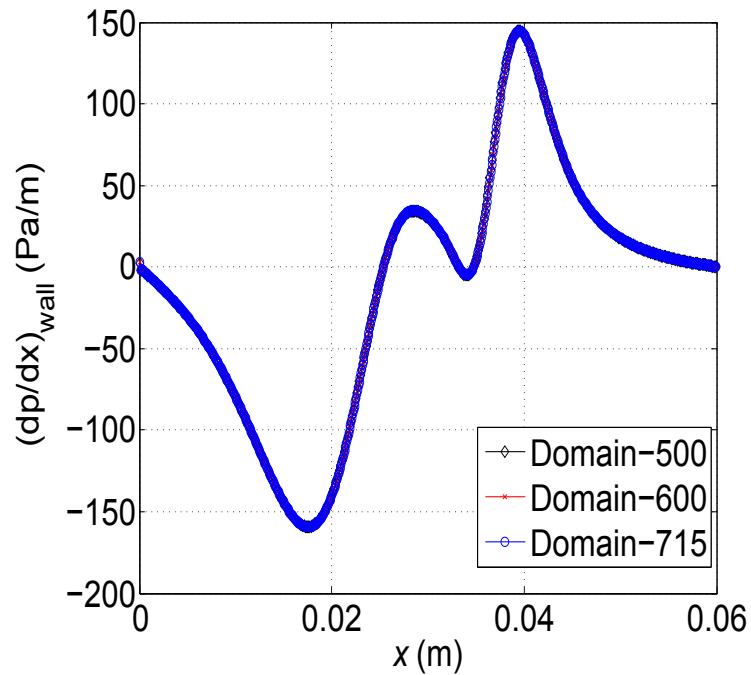


Figure 4.15: Comparison of the wall-pressure gradient along the wall, at $t = 0.605$ s for *Domain-500, -600, -715*

4.4 Estimations Using Cartesian Taylor-series Model

The data set generated by Fluent simulations for three different grid sizes (*Domain-500*, *Domain-600*, and *Domain-715*) is further processed to estimate the u - and v -velocity (streamwise and wall-normal, respectively) components. The data set provides the velocity components and the pressure within the flow. Wall-pressure is extracted from the Fluent data file and the central difference scheme is applied to compute the wall-pressure gradient along the streamwise direction. The time derivatives of the wall-pressure gradient at each node on the wall is computed by applying the central difference method on the data available at the same node from adjacent data files, from the previous ($t-0.005$ s) and the next time step ($t+0.005$ s) (see Equation 4.1).

For a given estimation, the velocity profiles are estimated at the same x location as the wall point at which the wall-shear and wall-pressure-gradient derivatives are obtained. Thus, the series expansion is only done in y , but not in x (i.e. using a one-dimensional series). That is, estimates at a different x location are accomplished by moving the point of wall-stresses observation to the new x location rather than fixing the latter and using a two-dimensional series expansion. We believe this approach provides better accuracy by avoiding the expansion in the second dimension. In the following, there are two sets of comparisons done for the final velocity estimations based on -

- I. The same x location ($x = 25$ mm; directly beneath the vortex core center) but different grid resolutions (three cases, *Domain-500*, *Domain-600*, and *Domain-715*)
- II. The same grid resolution (600×600) but two different estimation locations: $x = 25$ mm (similar to part 1 above) and $x = 30$ mm (below outer periphery of the primary vortex where the wall-stress signatures are weaker and velocity variation is less).

4.5 Results and Discussion

4.5.1 Comparison of estimations based on different grid resolutions

u - and v -Velocity estimations are done for the three cases of different grid sizes (*Domain-500*, *Domain-600*, and *Domain-715*). The idea is to study the effect of spatial resolution on the final estimations. As observed before (Figures 4.14 and 4.15), grid size doesn't have significant effect on the wall stresses at a given node on the wall, but high order expansions of the Taylor-series *may still exhibit* sensitivity to the grid resolution due to error in computing high order derivatives using the central difference scheme with different spatial step size (0.12, 0.10 and 0.084 mm for *Domain-500*, *Domain-600*, and *Domain-715* respectively).

The results are shown in Figure 4.16, 4.18 and 4.20 for u estimations and 4.17, 4.19 and 4.21 for the v estimations. In each figure, the true velocity profile, obtained from Fluent, is shown using red diamonds. Other symbols/line colors represent the estimation done using different series orders up to 15. Note that the series order is the order of y in the *stream function*. Also, the domain extent in the wall-normal direction is truncated to only encompass the y range for which accurate estimation could be obtained. This range is approximately less than one tenth the height of the vortex core center above the wall for all Taylor-series orders considered. Outside the y range shown, the series estimate deviates considerably from the true velocity value such that it is not meaningful to show results for a wider domain.

Inspection of Figures 4.16 through 4.21 reveals a pattern in which increasing the Taylor-series estimation order, starting from the first order, systematically increases the range of

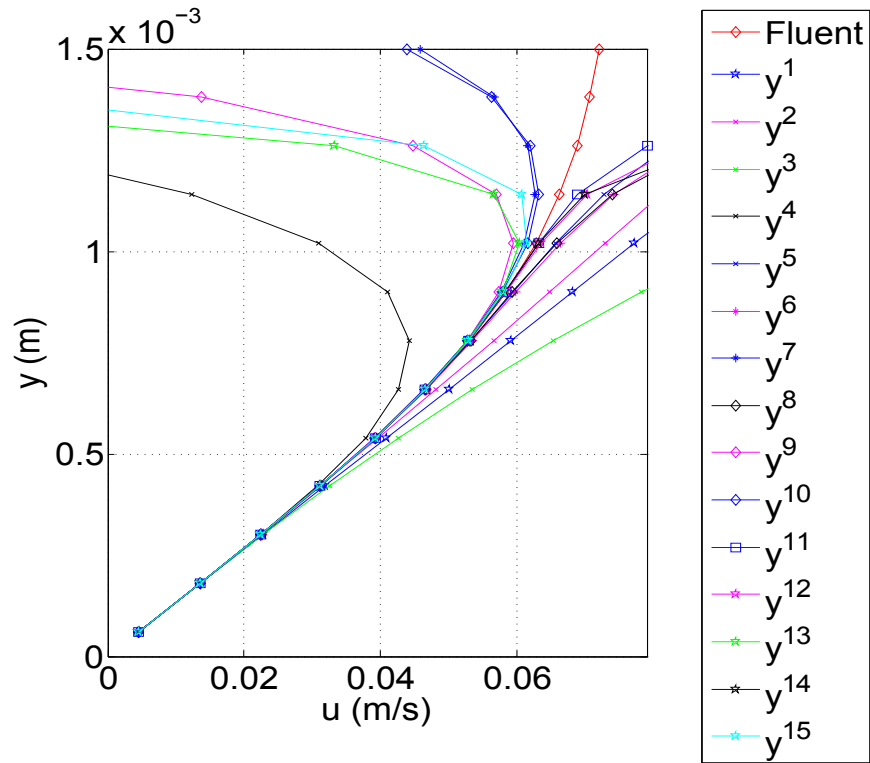


Figure 4.16: u -Velocity estimation using Taylor-series expansions up to 15th order for the case of *Domain-500* in a plane through the center of the primary vortex ($x = 25$ mm)

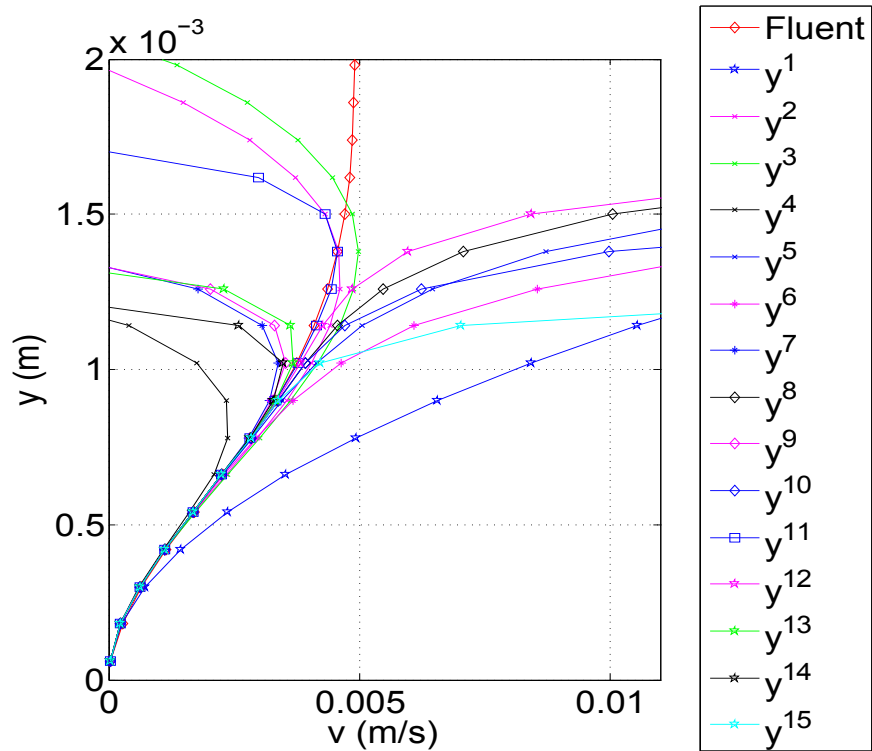


Figure 4.17: v -Velocity estimation using Taylor-series expansions up to 15th order for the case of *Domain-500* in a plane through the center of the primary vortex ($x = 25$ mm)

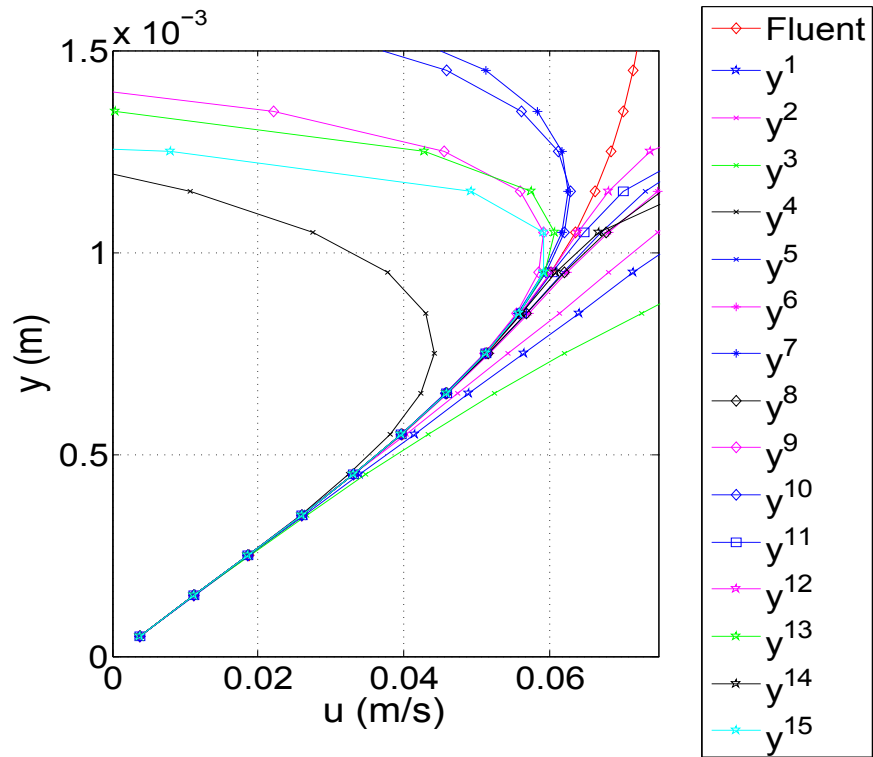


Figure 4.18: u -Velocity estimation using Taylor-series expansions up to 15th order for the case of *Domain-600* in a plane through the center of the primary vortex ($x = 25$ mm)

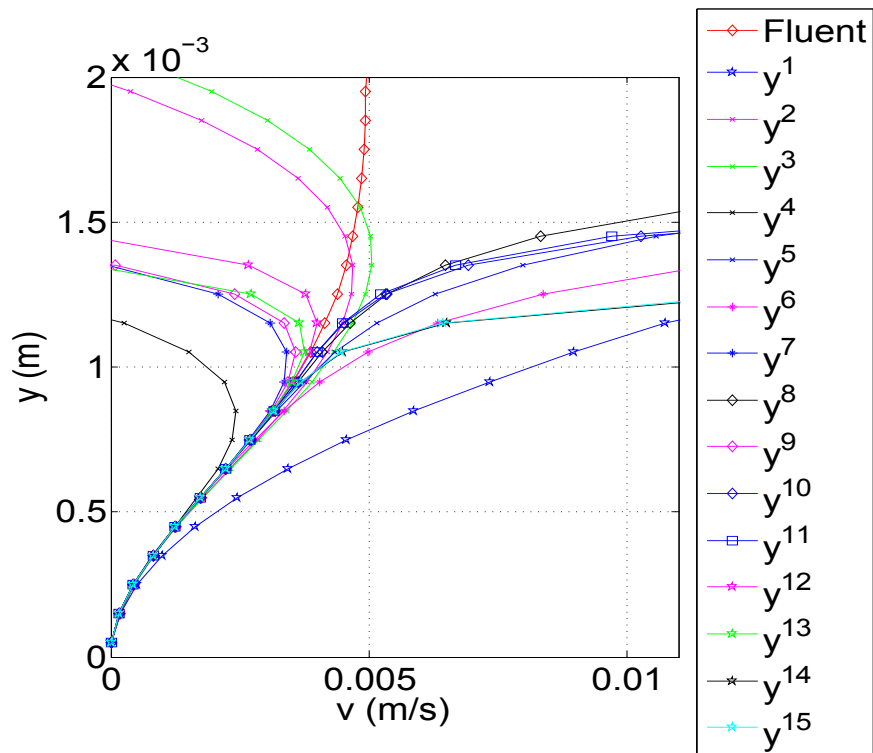


Figure 4.19: v -Velocity estimation using Taylor-series expansions up to 15th order for the case of *Domain-600* in a plane through the center of the primary vortex ($x = 25$ mm)

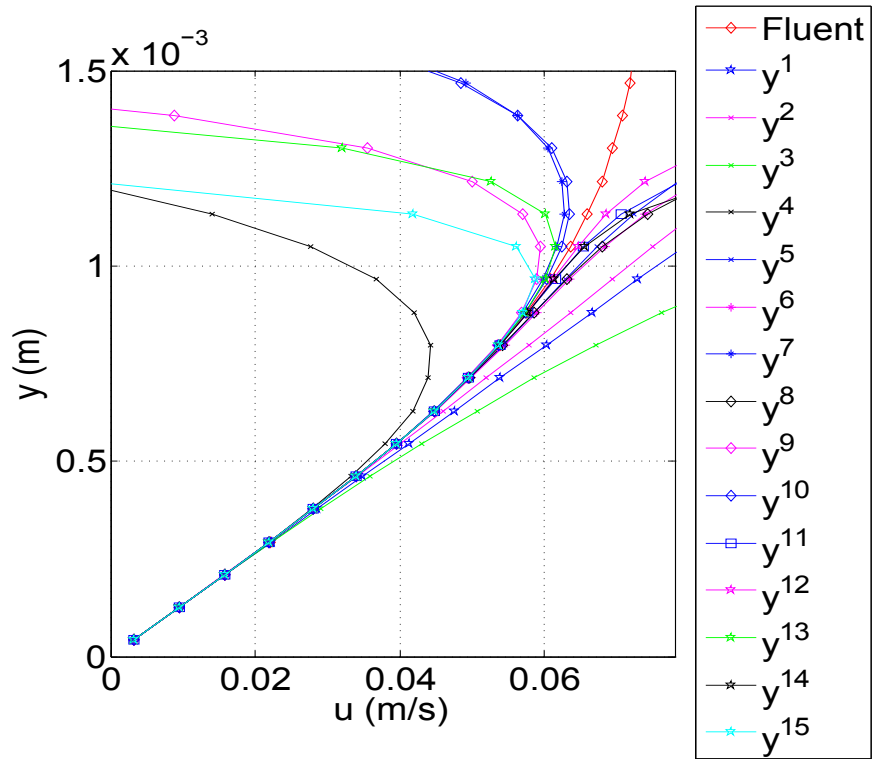


Figure 4.20: u -Velocity estimation using Taylor-series expansions up to 15th order for the case of *Domain-715* in a plane through the center of the primary vortex ($x = 25$ mm)

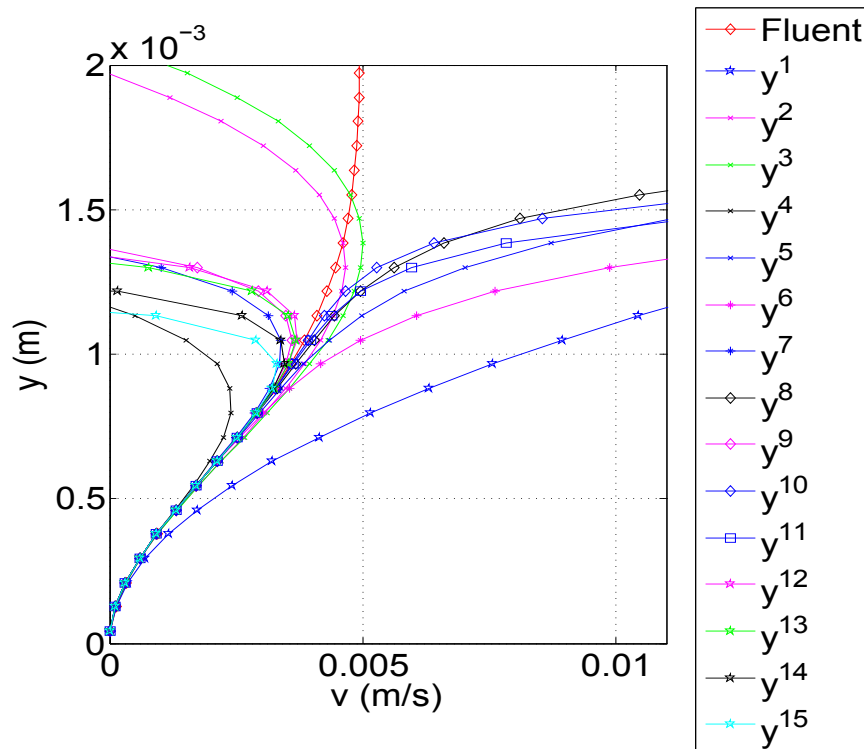


Figure 4.21: v -Velocity estimation using Taylor-series expansions up to 15th order for the case of *Domain-715* in a plane through the center of the primary vortex ($x = 25$ mm)

y over which good agreement is obtained between the series and the true velocity. This trend, however, continues only up to a certain order beyond which the range of agreement becomes smaller rather than bigger. This is unlike what one would expect from both a theoretical point of view (*i.e.* increasing the order should increase the accuracy of the series) as well as from results presented in Chapter 2 concerning the series expansion for simple flows with known analytical solution. The key difference, however, between the latter and the present case is that for the simple flows, the wall stresses are known analytically, and hence they can be differentiated up to an arbitrary order without loss of accuracy. In the present case, the stresses are known from a numerical solution and one would expect that, even with very high spatial and temporal resolution and minimum 'numerical noise', the accuracy of the derivatives will start to deteriorate beyond a certain order. Thus, the order of the series beyond which the results in Figures 4.16 through 4.21 become less accurate may be considered as a break-even point; at which further increase in the estimation accuracy by increasing the series order is more than offset by the deterioration in the accuracy of the computed derivative.

In attempt to quantify the assessment of the Taylor series effectiveness in capturing the true velocity field as well as to compare the influence of the grid resolution systematically, the series order that gives agreement between the true and estimated velocity (to within 0.1%) over the *largest* y range is identified. A list of this order for the three grid resolutions, along with the y range of agreement is given in Tables 4.1 and 4.2 for estimations of u and v respectively. One of the key observation for the table is that the y range over which the series convergence is satisfactory is very small compared to the core center of the primary vortex. This shows that the Taylor-series-based estimation would be unusable for capturing

the vortex velocity field and associated characteristics. Specifically, the convergence of the series is too slow to be a useful tool for wake vortex detection.

Finally, Tables 4.1 and 4.2 show that although some differences are seen in the most accurate series order and corresponding y range for different grid resolutions, these differences are not substantial. Essentially for all cases the most accurate estimate is obtained for a series order of 8 - 12 over a domain range of approximately 1 mm (or 5.7057% of the core vortex center).

Table 4.1: Comparison of the y extent from the wall over which the u -velocity estimation has an error less than $\pm 0.1\%$ at a location directly beneath the center of the primary vortex ($x = 25$ mm) for different grid sizes

Case	Series Order	Location above the wall (mm)	% of the core vortex center	Actual velocity (Fluent) $\times 10^{-3}$ m/s	Estimated velocity $\times 10^{-3}$ (m/s)
Domain-500	12	0.9000	5.4152	58.44	58.39
Domain-600	12	0.9500	5.7057	60.26	60.28
Domain-715	12	0.7972	4.7860	53.78	53.79

Table 4.2: Comparison of the y extent from the wall over which the v -velocity estimation has an error less than $\pm 0.1\%$ at a location directly beneath the center of the primary vortex ($x = 25$ mm) for different grid sizes

Case	Series Order	Location above the wall (mm)	% of the core vortex center	Actual velocity (Fluent) $\times 10^{-3}$ m/s	Estimated velocity $\times 10^{-3}$ (m/s)
Domain-500	8	0.780	4.6931	2.839	2.837
Domain-600	12	0.950	5.7057	3.537	3.540
Domain-715	10	0.797	4.7848	2.910	2.913

4.5.2 The same grid resolution (600×600) but two different estimation locations: $x = 25$ mm and $x = 30$ mm

Similar comparison is done for the case of *Domain-600* in which we expanded series in two different planes. The two planes selected are -

1. $x = 25$ mm : A plane passing through the center of the primary vortex.
2. $x = 30$ mm : A plane passing through the outer edge of the Primary vortex.

The Tables (4.3 and 4.4) are self-explanatory. It shows that u -velocity can be estimated with low order series in a plane through $x = 30$ mm as compared to the one passing through the center of the vortex but the domain of estimation above the wall is very small as compared to that with 12th order series for the expansions in plane $x = 25$ mm. v -velocity, on the other hand, has the lower order expansion capturing more distance above the wall in the plane $x = 30$ mm as compared to the case of plane $x = 25$ mm.

Table 4.3: Comparison of the y extent from the wall over which the u -velocity estimation has an error less than $\pm 0.1\%$ at a location directly beneath the center of the primary vortex ($x = 25$ mm) and $x = 30$ mm

Case	Series Order	Location above the wall (mm)	% of the core vortex center	Actual velocity (Fluent) $\times 10^{-3}$ m/s	Estimated velocity $\times 10^{-3}$ (m/s)
$x = 25$ mm	12	0.950	5.7057	60.26	60.28
$x = 30$ mm	6	0.350	2.1021	55.19	55.18

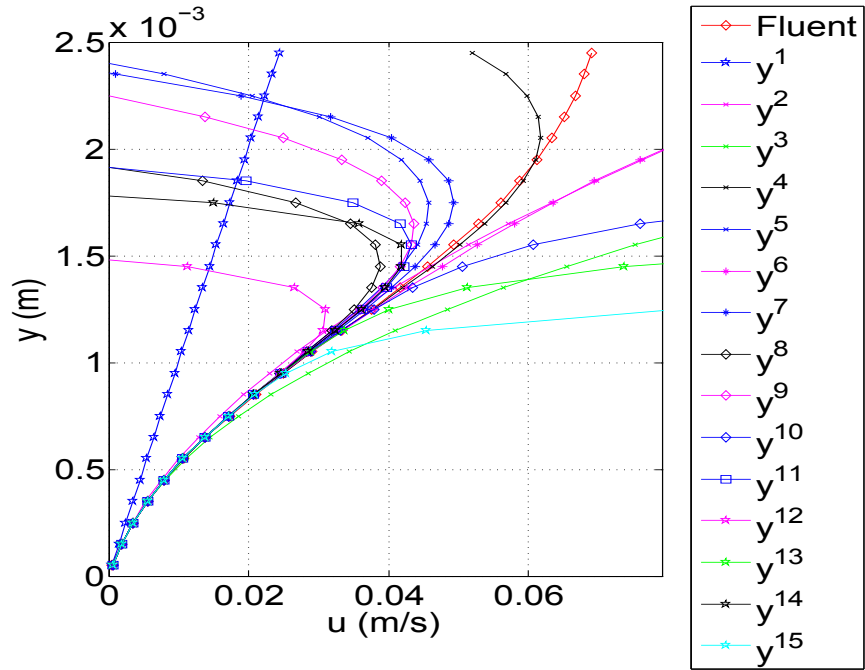


Figure 4.22: u -Velocity estimation using Taylor-series expansions up to 15th order for the case of *Domain-600* in a plane through outer edge (away from the axis) of the Primary vortex ($x = 30$ mm)

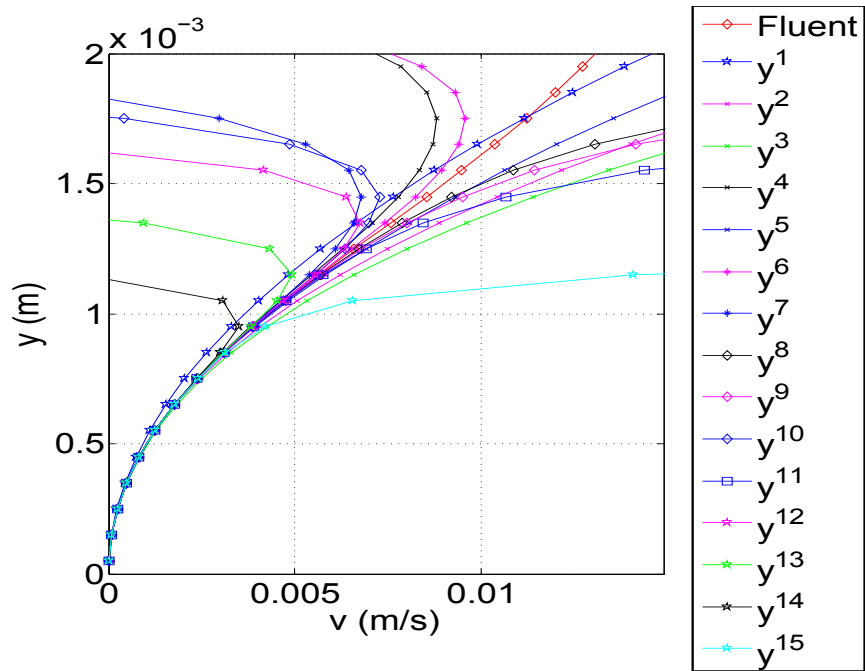


Figure 4.23: v -Velocity estimation using Taylor-series expansions up to 15th order for the case of *Domain-600* in a plane through outer edge (away from the axis) of the Primary vortex ($x = 30$ mm)

Table 4.4: Comparison of the y extent from the wall over which the u -velocity estimation has an error less than $\pm 0.1\%$ at a location directly beneath the center of the primary vortex ($x = 25$ mm) and $x = 30$ mm

Case	Series Order	Location above the wall (mm)	% of the core vortex center	Actual velocity (Fluent) $\times 10^{-3}$ m/s	Estimated velocity $\times 10^{-3}$ (m/s)
$x = 25$ mm	12	0.950	5.7057	3.537	3.540
$x = 30$ mm	8	1.050	6.3036	4.748	4.747

Chapter 5

Summary, Conclusions and Recommendations

As outlined in Chapter I, we followed a three-step approach during this research. This chapter captures key results and conclusions from each step.

5.1 Summary and Conclusions

We successfully constructed a Taylor-series model, based on the ideas discussed by Dallman *et al.* [2], that enables the estimation of the velocity field from wall-stress information in Cartesian geometry. MATLAB[®] programs were constructed to derive and compute Taylor-series coefficients up to any arbitrary order. The model and the MATLAB[®] program were validated using known analytical flows, namely Blasius boundary layer, 2D steady stagnation-point Falkner Skan ($m = 1$) flow, and Stokes oscillating stream problem. These validation tests show that the estimations do agree very closely with the analytical solution but one of the important findings was that the series converges very slowly. Steady flows such

as Blasius boundary layer and Falkner Skan ($m = 1$) show very slow convergence pattern. Specifically, though the solution over more than one-third of the boundary layer thickness is captured accurately with a 5th order series, a 45th order series was insufficient to represent the solution over the entire boundary layer extent. The solution of Stokes oscillating stream problem showed faster rate of convergence. Though the reason for this is unclear, it is notable that in this case the wall shear stress and pressure gradient are invariant in space, and hence the series coefficients are independent of spatial derivatives of the wall stresses.

To address the motivation of potentially using the Taylor-series model in sensing aircraft wake vortices, the model was used to estimate the velocity field of a counter-rotating vortex pair above a wall. The flow field was generated using numerical simulation employing ANSYS[®]-Fluent. In order to perform the simulation accurately we needed some baseline flow to validate the simulated flow. We identified the experiments - of the closely-related problem of an axisymmetric vortex ring impinging on a solid wall [2]- conducted at Michigan State University - as a good bench mark to validate the computational approach against.

The computation was initialized using Gaussian vorticity distribution, the parameters of which were set by matching the distribution to the experimental data, in the least-squares sense. Grid and time-step sensitivity tests were undertaken, showing that the employed resolutions of 0.918 (normalized based on the factor $\frac{R_c^2}{\Gamma_0}$) and 0.02 (normalized based on the initial vortex core radius (R_c)) are sufficient to accurately resolve the evolution of the primary vortex ring.

Having identified the computational parameters for accurate simulation of a vortex above a wall, the flow of a two-dimensional counter-rotating vortex pair was computed. We performed three simulations for three different grid sizes (500×500 , 600×600 , 715×715).

We observed that there is no significant effect of grid size on computation of the wall-shear stress and the wall-pressure gradient but it did influence the accuracy of estimated velocities with different orders of expansions. Most significantly, similar to the simple analytical flow, the series convergence was extremely slow, enabling the capture of the velocity field of only a portion of the boundary layer (approximately 5% of the vortex core center height). However, unlike the simple analytical flows, the accuracy of the series did not increase monotonically with increasing series order. The trend only held up to 8th to 10th order, then further increase in series order resulted in less accurate estimation. This is attributed to the loss of accuracy in computing high-order derivatives from numerical data.

Overall, as much as succeeded to validate the Taylor-series model for estimation of velocities in the flow-field, the accuracy of the estimation and its practical usage is severely limited by the spatial and temporal resolution required to accurately compute high order derivatives. The model application is also limited by several factors such as knowledge of flow stresses at large number of surface points, data captured over a large time range, and the slow convergence rate. Therefore, regarding the original research motivation, we conclude that the Taylor-series model is incapable of estimating the vortex flows behind an aircraft.

5.2 Recommendations

There is further scope for analysis of the Taylor-series model as well as to refine the computation of the vortex-ring/counter-rotating-vortex-pair impinging on a wall. Some of the associated recommendations are listed below-

1. As we determined that the high-order expansions do not provide good estimation over the complete boundary layer, we can cover the near-wall region with the Taylor-series model

and use this information as a boundary condition to estimate the remaining domain using *efficient* function bases. This approach will reduce the number of coefficients considerably and requires fewer boundary conditions. These function bases can be obtained, for instance, from Proper Orthogonal Decomposition of wake-vortex data.

2. The model needs to be tested for different temporal resolutions to examine the effect of the latter on the accuracy and quality of the estimation.

3. Some study could be done to see if the Taylor-series model can be used for Boundary layer control (since the latter application may only require very-near-wall information).

4. It will be advantageous to perform simulations with non-uniform grid in the near-wall region. This will improve the accuracy of the wall-shear stress and the wall-pressure, thereby reducing the estimation error propagating while computing high order derivatives.

5. Current approach is based on introduction of a primary vortex in flow domain at $t =$

0. This is equivalent to the experimental time $t = 1.4$ s, when the vortex was initially introduced. MTV data set provides us with the velocity vector array captured at $t = 1.4$

s. It would be interesting to simulate the flow by supplying velocities at each point in the flow domain as initial condition in Fluent, instead of introducing the primary vortex. This approach will simulate the initial boundary layer (if any) in the experiments and give us better near wall information, which will ultimately affect the accuracy of the Taylor-series model.

APPENDICES

APPENDIX A

Taylor-series Model for Axisymmetric Flow

We derived expressions for Taylor-series coefficients in Cartesian system in section 2.2. Similar exercise was done to derive coefficients for the Cylindrical Taylor-series model.

A.1 Derivation of the Taylor-series Model for Axisymmetric Flow

A.1.1 Step I. Expanding the stream function (ψ) in a two-dimensional, infinite Taylor-series form

$$\psi = \sum_{i=0}^{\infty} \sum_{j=0}^{\infty} a_{ij} r^{j+1} z^{i+2} \quad (\text{A.1})$$

Where a_{ij} are the series coefficients (which are time dependent), and r and z are stream-wise and wall-normal coordinates respectively. Note that the lowest power of z in the series

is 2. This is so because of the wall boundary conditions:

$$\psi_{z=0} = 0 \tag{A.2}$$

$$V_{r,y=0} = \frac{-1}{r} \frac{\partial \psi}{\partial z} \Big|_{z=0} = 0 \tag{A.3}$$

This also guarantees-

$$v_{z,y=0} = \frac{1}{r} \frac{\partial \psi}{\partial r} \Big|_{z=0} = 0 \tag{A.4}$$

A.1.2 Step II. Expressing the velocity components in a series form by differentiating the series for the stream function given by Equation A.1

Since the series defined for the stream function (ψ) is continuous and differentiable in space, we differentiate it to obtain the series form for the velocity components. Considering the streamwise velocity component (in r direction):

$$v_r = \frac{-1}{r} \left(\frac{\partial \psi}{\partial z} \right) \tag{A.5}$$

$$v_r = - \sum_{i=0}^{\infty} \sum_{j=0}^{\infty} a_{ij} (i+2) r^j z^{i+1} \tag{A.6}$$

Wall-normal velocity component (in z direction):

$$v_z = \frac{1}{r} \left(\frac{\partial \psi}{\partial r} \right) \quad (\text{A.7})$$

$$v_z = - \sum_{i=0}^{\infty} \sum_{j=1}^{\infty} a_{ij} (j+1) r^{j-1} z^{i+2} \quad (\text{A.8})$$

A.1.3 Step III. Obtaining series expressions for partial derivatives of the velocity components in the momentum equations A.20

Starting with Equation A.6 and differentiating with respect to r:

$$\frac{\partial v_r}{\partial r} = - \sum_{i=0}^{\infty} \sum_{j=1}^{\infty} a_{ij} (i+2)(j) r^{j-1} z^{i+1} \quad (\text{A.9})$$

Differentiating A.9 with respect to r :

$$\frac{\partial^2 v_r}{\partial r^2} = - \sum_{i=0}^{\infty} \sum_{j=2}^{\infty} a_{ij} (i+2)(j)(j-1) r^{j-2} z^{i+1} \quad (\text{A.10})$$

Differentiating equation A.5 with respect to z:

$$\frac{\partial v_r}{\partial z} = - \sum_{i=0}^{\infty} \sum_{j=0}^{\infty} a_{ij} (i+2)(i+1) r^j z^i \quad (\text{A.11})$$

Differentiating A.11 with respect to z:

$$\frac{\partial^2 v_r}{\partial z^2} = - \sum_{i=1}^{\infty} \sum_{j=0}^{\infty} a_{ij} (i+2)(i+1)(i) r^j z^{i-1} \quad (\text{A.12})$$

Similarly, differentiating equation with respect to z :

$$\frac{\partial v_z}{\partial z} = \sum_{i=0}^{\infty} \sum_{j=1}^{\infty} a_{ij} (i+2)(j+1) r^{j-1} z^{i+1} \quad (\text{A.13})$$

Differentiating Equation A.13 with respect to z :

$$\frac{\partial v_z}{\partial z^2} = \sum_{i=0}^{\infty} \sum_{j=1}^{\infty} a_{ij} (i+2)(i+1)(j+1) r^{j-1} z^i \quad (\text{A.14})$$

Differentiating Equation A.7 with respect to r :

$$\frac{\partial v_z}{\partial r} = \sum_{i=0}^{\infty} \sum_{j=2}^{\infty} a_{ij} (j-1)(j+1) r^{j-2} z^{i+2} \quad (\text{A.15})$$

Differentiating Equation A.15 with respect to r :

$$\frac{\partial^2 v_z}{\partial r^2} = \sum_{i=0}^{\infty} \sum_{j=3}^{\infty} a_{ij} (j+1)(j-1)(j-2) r^{j-3} z^{i+2} \quad (\text{A.16})$$

A.1.4 Step IV. Obtaining expression relating the lowest-order Taylor series coefficients a_{0j} to the wall shear stress using constitutive equation for Newtonian fluids

Starting with the constitutive equation for Newtonian fluids:

$$\tau_{wall} = \mu \left. \frac{\partial v_r}{\partial z} \right|_{z=0} \quad (\text{A.17})$$

Substituting series expression for $\frac{\partial v_r}{\partial z}$ (Equation A.11), and evaluating the expression

at wall i.e. $z = 0$:

$$\tau_{wall} = -\mu \sum_{i=0}^{\infty} \sum_{j=0}^{\infty} a_{ij} (i+2)(i+1)r^j z^i \Big|_{z=0} \quad (\text{A.18})$$

We observe that, only terms with z^0 will survive (i.e. $i = 0$) and the expression reduces to the form below-

$$\frac{\tau_{wall}}{-2\mu} = \sum_{j=0}^{\infty} a_{0j} r^j \quad (\text{A.19})$$

A.1.5 Step V. Obtaining expression relating the next-order Taylor series coefficients a_{1j} to the wall pressure gradient using the momentum equation in the streamwise direction

We use momentum equation in streamwise direction (r) and replace all differential terms by their corresponding series forms derived in step 4 above.

$$\rho \left(\frac{\partial v_r}{\partial t} + v_r \frac{\partial v_r}{\partial r} + v_z \frac{\partial v_r}{\partial z} \right) = -\frac{\partial p}{\partial r} + \mu \left[\frac{\partial}{\partial r} \left(\frac{1}{r} \frac{\partial}{\partial r} (r v_r) \right) + \frac{\partial^2 v_r}{\partial z^2} \right] \quad (\text{A.20})$$

Rearranging terms in Equation A.20 to obtain series expression for pressure gradient in streamwise (r) direction. We get-

$$\begin{aligned}
& -\frac{1}{\rho} \left(\frac{\partial p}{\partial r} \right) \tag{A.21} \\
& = - \sum_{i=0}^{\infty} \sum_{j=0}^{\infty} \dot{a}_{ij} (i+2) r^j z^{i+1} \\
& + \sum_{i=0}^{\infty} \sum_{j=0}^{\infty} \sum_{p=0}^{\infty} \sum_{q=1}^{\infty} a_{ij} a_{pq} (i+2)(p+2)(q) r^{j+q-1} z^{i+p+2} \\
& - \sum_{i=0}^{\infty} \sum_{j=1}^{\infty} \sum_{p=0}^{\infty} \sum_{q=0}^{\infty} a_{ij} a_{pq} (j+1)(p+1)(p+2) r^{j+q-1} z^{i+p+2} \\
& + v \left[\sum_{i=0}^{\infty} \sum_{j=2}^{\infty} a_{ij} (i+2)(j+1)(j-1) r^{j-2} z^{i+1} + \sum_{i=1}^{\infty} \sum_{j=0}^{\infty} a_{ij} (i+1)(i+2)(i) r^j z^{i-1} \right]
\end{aligned}$$

where, \dot{a} indicates differentiation with respect to time. If we evaluate the Equation A.21 at the wall,

$$\begin{aligned}
& -\frac{1}{\rho} \left(\frac{\partial p}{\partial r} \right)_{Wall} \tag{A.22} \\
& = - \sum_{i=0}^{\infty} \sum_{j=0}^{\infty} \dot{a}_{ij} (i+2) r^j z^{i+1} \\
& + \sum_{i=0}^{\infty} \sum_{j=0}^{\infty} \sum_{p=0}^{\infty} \sum_{q=1}^{\infty} a_{ij} a_{pq} (i+2)(p+2)(q) r^{j+q-1} z^{i+p+2} \\
& - \sum_{i=0}^{\infty} \sum_{j=1}^{\infty} \sum_{p=0}^{\infty} \sum_{q=0}^{\infty} a_{ij} a_{pq} (j+1)(p+1)(p+2) r^{j+q-1} z^{i+p+2} \\
& + v \left[\sum_{i=0}^{\infty} \sum_{j=2}^{\infty} a_{ij} (i+2)(j+1)(j-1) r^{j-2} z^{i+1} + \sum_{i=1}^{\infty} \sum_{j=0}^{\infty} a_{ij} (i+1)(i+2)(i) r^j z^{i-1} \right] \Big|_{y=0}
\end{aligned}$$

In equation A.22, only terms where the power of z is 0 will survive. Considering each of the terms on the right hand side, the lowest power of z is 1 in the first term, 2 in the second term, 2 in the third term, 1 in the fourth term and 0 in the last term. Thus, only the last term contributes and has components that do not vanish at the wall, giving an expression for the wall-pressure gradient in the streamwise direction in terms of a_{2j} :

$$\frac{1}{6\mu} \left(\frac{\partial p}{\partial r} \right)_{wall} = - \sum_{j=0}^{\infty} a_{1j} r^j \quad (\text{A.23})$$

A.1.6 Step VI. Obtaining expressions for higher-order Taylor series coefficients in terms of a_{0j} and a_{1j} and their time derivatives by successive differentiation (in the wall-normal direction) of the 2D momentum equations and evaluating the result at the wall

The series expression of the streamwise momentum equation is given by Equation A.21 above. The momentum equation in the wall-normal (z) direction is given by-

$$\rho \left(\frac{\partial v_z}{\partial t} + v_r \frac{\partial v_z}{\partial r} + v_z \frac{\partial v_z}{\partial z} \right) = - \frac{\partial p}{\partial z} + \mu \left[\frac{1}{r} \frac{\partial}{\partial r} \left(r \frac{\partial v_z}{\partial r} \right) + \frac{\partial^2 v_z}{\partial z^2} \right] \quad (\text{A.24})$$

$$\begin{aligned}
& -\frac{1}{\rho} \left(\frac{\partial p}{\partial z} \right) \tag{A.25} \\
& = \sum_{i=0}^{\infty} \sum_{j=1}^{\infty} a_{ij} (j+1) r^{j-1} z^{i+2} \\
& - \sum_{i=0}^{\infty} \sum_{j=0}^{\infty} \sum_{p=0}^{\infty} \sum_{q=2}^{\infty} a_{ij} a_{pq} (i+2)(q+1)(q-1) r^{j+q-2} z^{i+p+3} \\
& + \sum_{i=0}^{\infty} \sum_{j=1}^{\infty} \sum_{p=0}^{\infty} \sum_{q=1}^{\infty} a_{ij} a_{pq} (j+1)(q+1)(p+2) r^{j+q-2} z^{i+p+3} \\
& - v \left[\sum_{i=0}^{\infty} \sum_{j=3}^{\infty} a_{ij} (i+2)(j+1)(j-1)(j-1) r^{j-3} z^{i+2} \right] \\
& - v \left[\sum_{i=0}^{\infty} \sum_{j=1}^{\infty} a_{ij} (j+1)(i+2)(i+1) r^{j-1} z^i \right]
\end{aligned}$$

We combine expressions for both the momentum equations (A.21 and A.25 and rearrange the terms in such a way that highest order expansion coefficients (indicated by index i) will

be on the left hand side and other lower order terms appear on the right hand side. We get-

$$\begin{aligned}
& v \sum_{i=2}^{\infty} \sum_{j=0}^{\infty} a_{ij}(i+2)(i+1)(i)(i-1)r^j z^{i-2} \tag{A.26} \\
&= \sum_{i=0}^{\infty} \sum_{j=0}^{\infty} \dot{a}_{ij}(i+2)(i+1)r^j z^i + \sum_{i=0}^{\infty} \sum_{j=2}^{\infty} \dot{a}_{ij}(j+1)(j-1)r^{j-2} z^{i+2} \\
&- \sum_{i=0}^{\infty} \sum_{j=0}^{\infty} \sum_{p=0}^{\infty} \sum_{q=1}^{\infty} \dot{a}_{ij} \dot{a}_{pq}(i+2)(p+2)(q)(i+p+2)r^{j+q-1} z^{i+p+1} \\
&+ \sum_{i=0}^{\infty} \sum_{j=1}^{\infty} \sum_{p=0}^{\infty} \sum_{q=0}^{\infty} \dot{a}_{ij} \dot{a}_{pq}(j+1)(p+2)(p+1)(i+p+2)r^{j+q-1} z^{i+p+1} \\
&- \sum_{i=0}^{\infty} \sum_{j=0}^{\infty} \sum_{p=0}^{\infty} \sum_{q=2}^{\infty} \dot{a}_{ij} \dot{a}_{pq}(i+2)(q+1)(q-1)(j+q-2)r^{j+q-3} z^{i+p+3} \\
&- \sum_{i=0}^{\infty} \sum_{j=1}^{\infty} \sum_{p=0}^{\infty} \sum_{q=1}^{\infty} \dot{a}_{ij} \dot{a}_{pq}(p+2)(q+1)(j+1)(j+q-2)r^{j+q-3} z^{i+p+3} \\
&- v[2 \sum_{i=0}^{\infty} \sum_{j=2}^{\infty} \dot{a}_{ij}(i+2)(i+1)(j+1)(j-1)r^{j-2} z^i] \\
&- v[\sum_{i=0}^{\infty} \sum_{j=4}^{\infty} \dot{a}_{ij}(j+1)(j-1)^2(j-3)r^{j-4} z^{i+2}]
\end{aligned}$$

A.2 Demonstration In Axisymmetric Laminar Flows With Known Analytical Solution

In this section we will analyzing the axisymmetric flow (see Table A.1) to validate the coefficients derived by using MATLAB[®] code.

Table A.1: Analytical flows employed in validation of MATLAB[®] code used to derive Taylor series coefficients

Case No.	Flow	Nature of flow
1.	Axisymmetric Flow	<ol style="list-style-type: none"> 1. Steady flow. 2. Axisymmetric stagnation point flow. 3. The radial wall-shear stress and the wall pressure gradient are linear.

A.2.1 Axisymmetric Flow

The following derivation may be found in most standard textbooks on fluid mechanics (e.g. White [10], Section 3.8).

White [10] defines the streamwise velocity component in terms of similarity variable (η) as:

$$v_r = \frac{Br}{n-1} f'(\eta) \quad (\text{A.27})$$

And the wall normal velocity component in terms of similarity variables as:

$$v_z = -\sqrt{B\nu} f(\eta) \quad (\text{A.28})$$

And, the similarity variable is defines as:

$$\eta = -z\sqrt{\frac{B}{\nu}} \quad (\text{A.29})$$

Where z is wall-normal coordinate, r is streamwise coordinate, B is a constant, and ν is kinematic viscosity.

Differentiating A.27 with respect to z :

$$\frac{\partial v_r}{\partial z} = \frac{Br}{n-1} \sqrt{\frac{B}{\nu}} f''(\eta) \quad (\text{A.30})$$

Differentiating A.30 with respect to z :

$$\frac{\partial^2 v_r}{\partial z^2} = \frac{B^2 r}{(n-1)\nu} f'''(\eta) \quad (\text{A.31})$$

Shear stress at the wall can be obtained by multiplying Equation A.30, and evaluating it at the wall:

$$\tau_{wall} = \mu \frac{Br}{n-1} \sqrt{\frac{B}{\nu}} f''(0) \quad (\text{A.32})$$

For axisymmetric flow ($n = 3$), τ_{wall} is given by:

$$\tau_{wall} = \mu \frac{B}{2} \sqrt{\frac{B}{\nu}} f''(0) r \quad (\text{A.33})$$

Comparing Equations A.33 and A.34 to get the series for τ_{wall} :

$$\sum_{j=0}^{\infty} a_{0j} r^j = \frac{B}{4} \sqrt{\frac{B}{\nu}} f''(0) r; \quad (\text{A.34})$$

Equation A.34 implies that the wall-shear stress is linear in 'r' and gives a_{0j} coefficients.

$$a_{00} = 0 \quad (\text{A.35})$$

$$a_{01} = \frac{B}{4} \sqrt{\frac{B}{\nu}} f''(0) \quad (\text{A.36})$$

$$a_{02}, a_{03}, a_{04}, \dots a_{0\infty} = 0 \quad (\text{A.37})$$

Now, Equation A.20 when evaluated at the wall ($z = 0$) gives:

$$\frac{\partial p_{wall}}{\partial r} = \mu \frac{\partial^2 v_r}{\partial z^2} \quad (\text{A.38})$$

Combining Equations A.31 and A.38 (for $n = 3$, and at wall - $y = 0$):

$$\frac{\partial p_{wall}}{\partial r} = \frac{\mu B^2}{(2)\nu} f'''(0)r \quad (\text{A.39})$$

Combining Equations A.39 and A.23

$$\sum_{j=0}^{\infty} a_{1j} r^j = -\frac{B^2}{12\nu} f'''(0)r \quad (\text{A.40})$$

Equation A.40 implies that the wall-pressure gradient is linear in 'r' and gives a_{1j} coefficients, as below-

$$a_{10} = 0 \quad (\text{A.41})$$

$$a_{11} = -\frac{B^2}{12\nu} f'''(0) \quad (\text{A.42})$$

$$a_{12}, a_{13}, a_{14}, \dots a_{1\infty} = 0 \quad (\text{A.43})$$

Having computed the coefficients using MATLAB[®], we now estimate series for v_r and v_z . Figure A.1 and A.2 depict the series expansions up to 40th order of the stream function. It is evident from the figure that the convergence is very slow. It implies that we need to a polynomial series higher than 40th order to estimate the complete analytical profile.

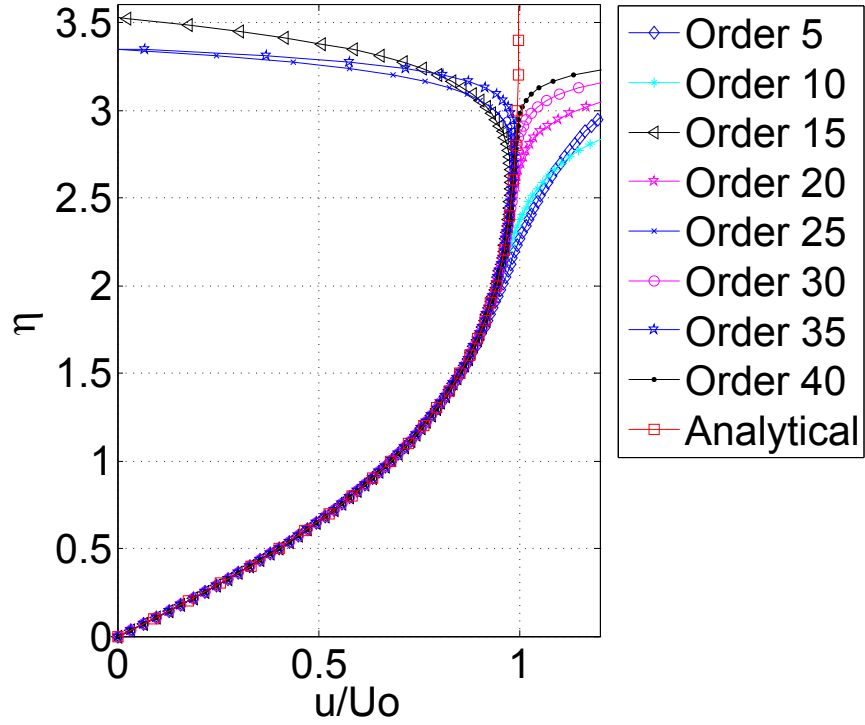


Figure A.1: Series expansions up to the 40th order of the radial velocity compared to the analytical solution for axisymmetric stagnation flow

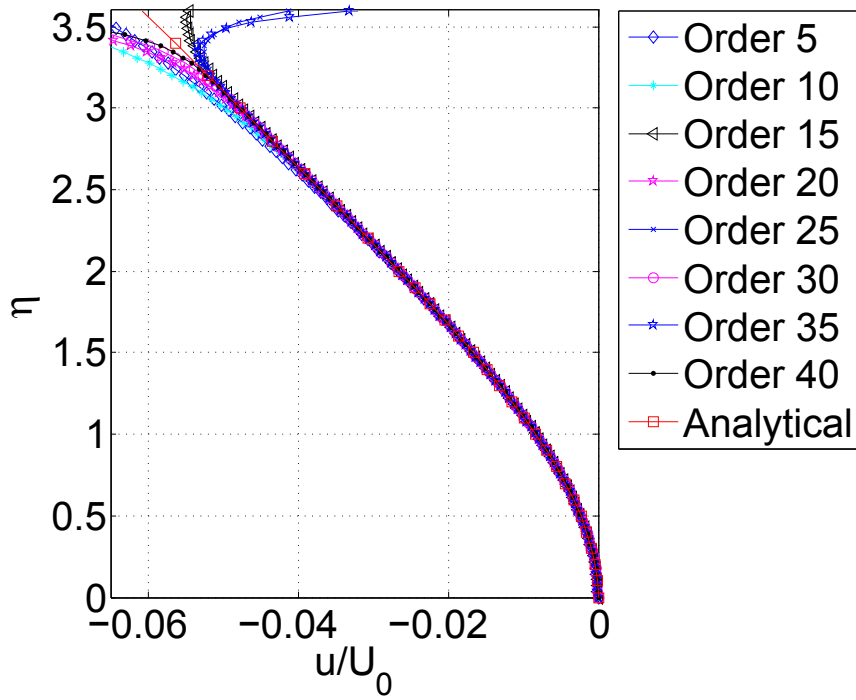


Figure A.2: Series expansions up to the 40th order of the wall-normal velocity compared to the analytical solution for axisymmetric stagnation flow

BIBLIOGRAPHY

BIBLIOGRAPHY

- [1] Speijker, N., Vidal A., Barbaresco F., Gerz, T., Barny, H., Winckelmans, G. (2005) ATC-Wake: Integrated Wake Vortex Safety and Capacity System (ATC Wake D6.2), IST2001-34729.
- [2] Dallmann, U. and Gebing, H. (1994) Flow attachment at flow separation lines: on uniqueness problems between wall-flows and off-wall fields, *Acta Mechanica* [Suppl] 4, 47.
- [3] Gendrich, C. P., Bohl, D., and Koochesfahani, M. M. [1997] Whole field measurements of unsteady separation in a vortex ring/wall interaction, AIAA Paper No. AIAA-97-1780.
- [4] Wu, J.Z., Wu, J.M. and Wu, C.J. (1987) A general three-dimensional viscous compressible theory on the interaction of solid body and vorticity-dilatation field, University of Tennessee Space Institute Report 87/031.
- [5] D. Fabris, D. Liepmann, and D. Marcus, Quantitative experimental and numerical investigation of a vortex ring impinging on a wall, *Phys. Fluids* 8, 2640 1996.
- [6] Chu, C.-C., Wang, C.-T. and Chang, C.-C. [1995] A vortex ring impinging on a solid plane surface vortex structure and surface force, *Phys. Fluids*, 7(6), 1391
- [7] Orlandi, P. and Verzicco, R. [1993], Vortex rings impinging on walls: axisymmetric and threedimensional simulations, *J. Fluid Mech.*, 256, 615
- [8] Naguib, A. and Koochesfahani, M. M. (2004) On wall-pressure sources associated with the unsteady separation in a vortex-ring/wall interaction, *Phys. Fluids*, Vol. 16, No. 7, 2613-2622.
- [9] Panton, R. L. (2005) *Incompressible Flow Third Edition*. New Delhi, India: Wiley India (P) Ltd.

- [10] White F.M. (1991), *Viscous Fluid Flow*, McGraw Hill International.
- [11] Lele SK (1990) Compact finite difference schemes with spectral-like resolution, CTR Manuscript 107, NASA Technical Reports.
- [12] Etebari A, Vlachos PP (2005) Improvements on the accuracy of derivative estimation from DPIV velocity measurements. *Exp Fluids* 39: 1040-1050.
- [13] <http://www.aerospaceweb.org/question/nature/q0237.shtml>